INSTITUTO FEDERAL DE EDUCAÇÃO, CIÊNCIA E TECNOLOGIA
GOIANO – *CAMPUS* RIO VERDE
PRÓ-REITORIA DE PESQUISA, PÓS-GRADUAÇÃO E INOVAÇÃO
PROGRAMA DE PÓS-GRADUAÇÃO EM AGROQUÍMICA

Gabriel Cabral da Fonseca

Boosting light-driven photoelectrocatalytic water oxidation by using green source-based carbon quantum dots

RIO VERDE - GOIÁS

DECEMBER – 2024

INSTITUTO FEDERAL DE EDUCAÇÃO, CIÊNCIA E TECNOLOGIA
GOIANO – *CAMPUS* RIO VERDE
PRÓ-REITORIA DE PESQUISA, PÓS-GRADUAÇÃO E INOVAÇÃO
PROGRAMA DE PÓS-GRADUAÇÃO EM AGROQUÍMICA

Boosting light-driven photoelectrocatalytic water oxidation by using green source-based carbon quantum dots

Thesis presented to the Postgraduate Program in Agrochemistry of Goiano Federal Institute Campus Rio Verde, in partial fulfillment of the requirements for the degree of Master in Agrochemistry.

RIO VERDE - GOIÁS
DECEMBER – 2024

da Fonseca, Gabriel Cabral

Cutter Boosting light-driven photoelectrocatalytic water oxidation by using green source-based carbon quantum dots / Gabriel Cabral da Fonseca. Rio Verde. – 2024.
87f. : il.

Dissertação (Mestrado) – Instituto Federal Goiano – Câmpus Rio Verde, 2024.
Orientador: Doutor. João Carlos Perbone de Souza.

Bibliografia

1. Carbon quantum dots. 2. Water oxidation reaction. 3. Photoelectrocatalysis. I. Título II. Instituto Federal Goiano – Câmpus Rio Verde.

CDD

INSTITUTO FEDERAL
Goiano

Repositório Institucional do IF Goiano - RIIF Goiano
Sistema Integrado de Bibliotecas

TERMO DE CIÊNCIA E DE AUTORIZAÇÃO
PARA DISPONIBILIZAR PRODUÇÕES TÉCNICO-CIENTÍFICAS NO REPOSITÓRIO INSTITUCIONAL DO IF GOIANO

Com base no disposto na Lei Federal nº 9.610, de 19 de fevereiro de 1998, AUTORIZO o Instituto Federal de Educação, Ciência e Tecnologia Goiano a disponibilizar gratuitamente o documento em formato digital no Repositório Institucional do IF Goiano (RIIF Goiano), sem ressarcimento de direitos autorais, conforme permissão assinada abaixo, para fins de leitura, download e impressão, a título de divulgação da produção técnico-científica no IF Goiano.

IDENTIFICAÇÃO DA PRODUÇÃO TÉCNICO-CIENTÍFICA

☐ Tese (doutorado)
☑ Dissertação (mestrado)
☐ Monografia (especialização)
☐ TCC (graduação)
☐ Artigo científico
☐ Capítulo de livro
☐ Livro
☐ Trabalho apresentado em evento

☐ Produto técnico e educacional - Tipo:

Nome completo do autor: GABRIEL CABRAL DA FONSECA
Matrícula: 2023102310340002
Título do trabalho: Boosting light-driven photoelectrocatalytic water oxidation by using green source-based carbon quantum dots

RESTRIÇÕES DE ACESSO AO DOCUMENTO

Documento confidencial: ☑ Não ☐ Sim, justifique:

Informe a data que poderá ser disponibilizado no RIIF Goiano: ☐/☐/☐
O documento está sujeito a registro de patente? ☐ Sim ☑ Não
O documento pode vir a ser publicado como livro? ☐ Sim ☑ Não

DECLARAÇÃO DE DISTRIBUIÇÃO NÃO-EXCLUSIVA

O(a) referido(a) autor(a) declara:

- Que o documento é seu trabalho original, detém os direitos autorais da produção técnico-científica e não infringe os direitos de qualquer outra pessoa ou entidade;
- Que obteve autorização de quaisquer materiais inclusos no documento do qual não detém os direitos de autoria, para conceder ao Instituto Federal de Educação, Ciência e Tecnologia Goiano os direitos requeridos e que este material cujos direitos autorais são de terceiros, estão claramente identificados e reconhecidos no texto ou conteúdo do documento entregue;
- Que cumpriu quaisquer obrigações exigidas por contrato ou acordo, caso o documento entregue seja baseado em trabalho financiado ou apoiado por outra instituição que não o Instituto Federal de Educação, Ciência e Tecnologia Goiano.

RIO VERDE 16 /12 /2024
Local Data

Gabriel Cabral da Fonseca
Assinatura do autor e/ou detentor dos direitos autorais

Ciente e de acordo:
João C. Perbone de Souza
Assinatura do (a) orientador(a)

SERVIÇO PÚBLICO FEDERAL
MINISTÉRIO DA EDUCAÇÃO
SECRETARIA DE EDUCAÇÃO PROFISSIONAL E TECNOLÓGICA
INSTITUTO FEDERAL DE EDUCAÇÃO, CIÊNCIA E TECNOLOGIA GOIANO

BOOSTING LIGHT-DRIVEN PHOTOELECTROCATALYTIC WATER OXIDATION BY USING GREEN SOURCE-BASED CARBON QUANTUM DOTS

Autor: Gabriel Cabral da Fonseca
Orientador: João Carlos Perbone de Souza

TITULAÇÃO: Mestre em Agroquímica – Área de Concentração Agroquímica

APROVADA em 16 de dezembro de 2024.

Assinado eletronicamente
Prof. Dr. Rodrigo Michelin Iost
Avaliador externo
Instituto de Química - Universidade de São Paulo

Assinado eletronicamente
Prof. Dr. Rafael Nery Prystaj Colombo
Avaliador externo
Instituto de Química de São Carlos – Universidade de São Paulo

Assinado eletronicamente
Prof. Dr. João Carlos Perbone de Souza
Presidente da banca
IF Goiano - Campus Rio Verde

Documento assinado eletronicamente por:

- **Joao Carlos Perbone de Souza, Joao Carlos Perbone de Souza - Professor Avaliador de Banca - Universidade de São Paulo (63025530000104)**, em 16/12/2024 17:21:36.
- **Rodrigo Michelin Iost, Rodrigo Michelin Iost - Professor Avaliador de Banca - Universidade de São Paulo (63025530000104)**, em 16/12/2024 17:22:54.
- **Rafael Neri Prystaj Colombo, Rafael Neri Prystaj Colombo - Professor Avaliador de Banca - Universidade de São Paulo (63025530000104)**, em 16/12/2024 17:23:43.

Este documento foi emitido pelo SUAP em 10/12/2024. Para comprovar sua autenticidade, faça a leitura do QRCode ao lado ou acesse https://suap.ifgoiano.edu.br/autenticar-documento/ e forneça os dados abaixo:

Código Verificador: 660802
Código de Autenticação: b5d623fc2c

INSTITUTO FEDERAL GOIANO
Campus Rio Verde
Rodovia Sul Goiana, Km 01, Zona Rural, 01, Zona Rural, RIO VERDE / GO, CEP 75901-970
(64) 3624-1000

AUTHOR BIOGRAPHY

Gabriel Cabral da Fonseca was born in February 2000 in Castelândia, Goiás, Brazil, a small country town. Your father is Francisco Caninde Cabral de Araújo, and his mother is Monica Cezar da Fonseca. He was raised with his amazing grandmother Elizabete Cezar da Fonseca. His academic journey began in 2016 when he enrolled in a chemistry technician course at the Goiano Federal Institute while completing high school. After finishing high school and his technician course, he pursued an undergraduate degree in chemistry.

During his undergraduate studies, Gabriel became involved in research under the mentorship of Professor Dr. João Carlos Perbone de Souza. Over four years, he contributed to various projects that focused on sustainable materials, including the utilization of lignocellulosic biomass to produce adsorbents, the extraction of cellulose for hydrogel synthesis, and the development of 3D-printed electrochemical cells and electrodes for batch injection analysis.

Currently pursuing a master's degree in Agrochemistry at the Goiano Federal Institute, collaborating with the São Carlos Institute of Chemistry at the University of São Paulo. His research focuses on synthesizing carbon quantum dots from lignocellulosic waste and exploring their potential applications in photoelectrocatalysis, aiming to develop sustainable and efficient technologies using green sources.

Gabriel is now on the way to enrolling in a PhD program, viewing the Basque Center on Materials, Applications and Nanostructures (BCMaterials) as a promising opportunity for furthering his research and academic growth. He hopes to engage with experts in the field and utilize advanced facilities to deepen his understanding and contribute to collaborative projects that address real-world challenges in materials science.

To my grandmother, Elizabete,
who never went to school.

ACKNOWLEDGMENTS

- To my grandmother, Elizabete, for teaching me how to be a good person and always supporting and praying for me.
- To my parents, Francisco and Monica, for their teaching and support.
- To my sister, Danielle, for being my example of a strong person.
- To my advisor, Dr. João Perbone, for all the teachings, the confidence in my work, the encouragement, and the friendship.
- To Professor Dr. Frank Crespilho, for welcoming me into your lab and for the confidence in my work.
- To Rafael Colombo for assistance in developing the light irradiation system.
- To Ednelson de Almeida, from the mechanical workshop, for the patience and assistance on the photoelectrochemical cell manufacture.
- To my friends Caio Lenon and Fhysmélia Albuquerque for the company in overnight lab experiments, and scientific discussions.
- To all my friends and lab colleagues, Esther Lopes, Ian Lima, João Vitor, Victor Hugo, Steffane Quaresma, Caio Lenon, Rodrigo Iost, Rafael Colombo, Luana Faria, for friendship, collaboration, and pleasant moments. Especially, Fhysmélia Albuquerque and Mayra Tamires (*coquetes*); thank you for often making my days better in São Carlos.
- To Goiano Federal Institute and São Carlos Institute of Chemistry, USP, for the facilities and infrastructure needed to perform this work.
- To FAPESP, for financial support to acquire reactants.
- To CAPES, for financial support (scholarship process number 88887.892512/2023-00).

“Study hard what interests you the most in the most undisciplined, irreverent, and original manner possible.”

Richard P. Feynman

“What an astonishing thing a book is. It's a flat object made from a tree with flexible parts on which are imprinted lots of funny dark squiggles. But one glance at it and you're inside the mind of another person, maybe somebody dead for thousands of years. Across the millennia, an author is speaking clearly and silently inside your head, directly to you. Writing is perhaps the greatest of human inventions, binding together people who never knew each other, citizens of distant epochs. Books break the shackles of time. A book is proof that humans are capable of working magic."

Carl Sagan

RESUMO

A síntese de pontos quânticos de carbono (PQCs) a partir de resíduos lignocelulósicos é uma alternativa sustentável, ambientalmente favorável e de baixo custo para produzir nanopartículas de carbono para diversas aplicações. Neste trabalho, estudamos a influência da conjugação de ftalocianina tetrassulfonada de níquel (NiTSPc) e PQCs de fonte sustentável para aplicação em processo de separação fotoeletrocatalítica da água. Os PQCs sintetizados foram caracterizados por espetroscopia Raman, infravermelho, ultravioleta-visível e fluorescência, e microscopia eletrônica de transmissão. Para os estudos de fotoeletrocatálise os eletrodos de trabalho foram produzidos sobre um vidro recoberto com óxido de índio dopado com estanho (ITO) utilizando a técnica *layer-by-layer*. A voltametria cíclica e a cronoamperometria foram utilizadas para avaliar o desempenho fotoeletrocatalítico no escuro e sob irradiação de luz azul e ultravioleta (UV). Sob luz azul, a densidade de corrente de NiTSPc/PCQ aumentou de 0,79 ± 0,03 µA cm^{-2} para 1,48 ± 0,11 µA cm^{-2} e sob luz UV de 0,77 ± 0,10 µA cm^{-2} para 3,83 ± 0,23 µA cm^{-2}, o que é 1,9 e 6,5 vezes a densidade de fotocorrente de CQD_{15} e ITO, respetivamente. O aumento da densidade de fotocorrente no eletrodo NiTSPc/PQC poder estar associado aos *holes* fotogerados na banda de valência do PQC que oxidam a água em oxigênio. Ao mesmo tempo, os elétrons fotogerados são transferidos dos PQCs para o NiTSPc e então para o contra eletrodo, resultando numa maior densidade de fotocorrente. Assim, os resíduos lignocelulósicos, como a biomassa da cana-de-açúcar, são uma excelente fonte de carbono para a fácil síntese de PQCs, oferecendo um destino para este resíduo e apresentando um nanomaterial ambientalmente sustentável para aumentar a oxidação fotoeletrocatalítica da água sob irradiação.

Palavras-chave: pontos quânticos de carbono, reação de oxidação da água, fotoeletrocatálise.

ABSTRACT

The synthesis of carbon quantum dots (CQDs) from lignocellulosic waste is a sustainable, environmentally friendly, and low-cost alternative to produce very versatile carbon nanoparticles. Herein, we study the influence of conjugation of nickel tetrasulfonated phthalocyanine (NiTSPc) and green source-based CQDs in photoelectrocatalytic water splitting. The synthesized CQDs were characterized by Raman, infrared, ultraviolet-visible, and fluorescence spectroscopy, and transmission electron microscopy. For photoelectrocatalysis studies, working electrodes were produced over a glass covered with tin-doped indium oxide (ITO) using the layer-by-layer technique. Cyclic voltammetry and chronoamperometry were used to evaluate the photoelectrocatalytic performance at dark and under blue and UV light irradiation. Under blue light, the current density of NiTSPc/CQD increased from 0.79 ± 0.03 µA cm^{-2} to 1.48 ± 0.11 µA cm^{-2} and under UV from 0.77 ± 0.10 µA cm^{-2} to 3.83 ± 0.23 µA cm^{-2} when turning on the UV light, which is 1.9 and 6.5 times the photocurrent of CQD15 and bare ITO, respectively. The increase in photocurrent density in the NiTSPc/CQD electrode may be associated with photogenerated holes in the valence band of PQC that oxidize water to oxygen. At the same time, the photogenerated electrons are transferred from CQDs to NiTSPc and then to the counter electrode. Thereupon, lignocellulosic residues, such as sugarcane biomass, are an excellent carbon source for facile synthesis of CQDs, offering a destination for this residue and presenting an environment-friendly nanomaterial for boosting light-driven photoelectrocatalytic water oxidation.

Keywords: carbon quantum dots, water oxidation reaction, photoelectrocatalysis.

TABLE OF CONTENTS

LIST OF FIGURES

LIST OF TABLES

LIST OF SYMBOLS, ABBREVIATIONS, AND ACRONYMS

CB – conduction band

CV – cyclic voltammetry

DLS - Dynamic light scattering

DOS - density of states

E_g – bandgap

E_{max} - maximum emission

E_{opt} - optical gap

E_U - Urbach parameter

FTIR - Fourier-transformed infrared spectroscopy

FTO – fluorine-doped tin oxide

GQD - graphene quantum dots

HOMO - highest occupied molecular orbital

ITO – indium tin oxide

LbL - layer-by-layer

LUMO - lowest unoccupied molecular orbital

NTs - nanotubes

SEM – scanning electron microscopy

SQD - semiconductor quantum dots

TEM – transmission electron microscopy

UV – ultraviolet

UV-Vis – ultraviolet-visible

VB – valence band

WAT - weak absorption tail

WL_{EX} – excitation wavelength

XPS – X-ray photoelectron spectroscopy

λ_{exc} – excitation wavelength

λ_{max} - maximum wavelength

1. INTRODUCTION

Fluorescent nanomaterials derived from green and low-cost sources pave the way for wide application on systems driven through photoelectrocatalysis. Nowadays, several photovoltaic systems are engineered aiming the utilization of sunlight to improve power-conversion efficiency (Gazzetto et al., 2020), (Sahai et al., 2023), (Roy et al., 2024). The utilization of photocatalysts is extensive, such for water splitting (J. Feng et al., 2024), production of high-value-added chemicals (Sayama, 2018), (Zhang et al., 2023) degradation of pollutants (X. Chen et al., 2024), (Ahlawat et al., 2023). However, the total or partial system uses inorganic semiconductors that not only can have high cost but also can cause various environmental problems due to instability in external environments by oxidation (Ali et al., 2020). Hence, greener and low-cost sources for the assembly of photocatalysts represent a step forward in environmental precautions.

Environment-friendly carbon-based nanomaterials constitute a new strategy for the construction of sustainable photoelectrocatalytic systems (Tong et al., 2024). Carbon quantum dots (CQDs), first obtained by Xu et al. (2004), are prominent nanomaterials with several features that thrive in potential applications in the field. CQDs are generally nanoparticles below 10 nm exhibit a broad solar absorption spectrum, fluorescence, high electrical conductivity (J. Zhang et al., 2021), and, depending on the source and route of synthesis, low-cost, compared to the metal ones; moreover, the ability to photogenerate charge transfer, together with biocompatibility property, chemical inertness, and low toxicity are remarkable characteristics concerning the potential applications (Rasal et al., 2021), (Pourmadadi et al., 2023), (Zhao et al., 2023).

The fluorescent properties of CQDs can be explained by two proposed mechanisms. The first associates fluorescence with the bandgap transitions of conjugated π-domains. The other relates fluorescence with defects in the CQD structure. Both mechanisms could be associated with the chemical surface, such as functional groups. Furthermore, the interaction between the carbon core and the surface functional groups plays an important role in electron transfer, including in reactions photocatalyzed by CQDs (R. Wang et al., 2017). Generally, the structural defects and functional group moieties are directly dependent on the route of synthesis.

Diverse sources are used to synthesize CQDs, such as small organic molecules (W. Li et al., 2024), carbon fiber materials (T. Wang et al., 2023), lignocellulosic sources (Raju et al., 2023), (Fang et al., 2024); and by various methods (bottom-up or top-down), such as microwave method (Gholipour et al., 2024), electrochemical method (Yu et al., 2024), hydrothermal method (Setianto et al., 2024), combustion and pyrolytic carbonization methods (Ahlawat et al., 2023), (Y. Zhang et al., 2024). The use of biomass-based sources for CQD synthesis boosts the recycling of waste resources, as well as reduces the cost of the raw material; with this, environmental protection is improved. The CQDs prepared from waste sources normally have good biocompatibility and excellent fluorescence emissions characteristics (L. Wang et al., 2023). In this regard, the synthesis through pyrolysis followed by acid treatment is efficient since converts biomass (top-down approach, for example) into the graphitic structure and the next step creates the nanoparticles with a high number of defects and functional groups, which is fundamental to the fluorescence emission and photocurrent activity (Zuo et al., 2016).

Sugarcane biomass represents a large source of carbon-based residue for the synthesis of CQDs. Several recent research shows the obtention of CQDs from sugarcane biomass (Qiu et al., 2022), (Kasinathan et al., 2022), (Deepanraj, 2024). All studies highlight the remarkable fluorescent features of the obtained nanomaterials. The role behind this feature could lead to a valuable application in photoelectrochemistry; from the benefits of the quantum size effect, these nanoparticles present noticeable properties for that use compared to other carbon materials (Z. Chen et al., 2022). Several studies have been conducted using CQDs for photocatalytic systems. J. Zhang et al. (2021) have used TiO_2 nanotubes (NTs) electrodes and CQD from biomass for photocatalytic reduction of CO_2. J. Xu et al. (2023) built heterojunction photoanodes with TiO_2 and CQDs for photoelectrocatalytic wastewater treatment. H. Y. Wang et al. (2021) synthesized CQDs from sodium ethylenediaminetetraacetic acid through the hydrothermal method for application in water splitting. N. Wang et al. (2023) have synthesized via hydrothermal method from three different precursors for H_2O_2 production. For photoelectrochemical water splitting, Kumar's group developed a Chlorophyll(a)/CQD Bio-Nanocomposite (Chl/CQDs_SiNW) photocathode onto a silicon nanowire (Roy et al., 2020).

The combination of CQDs with other materials remains an alternative way to enhance photocatalytic activity. Porphyrin byproducts such as phthalocyanines in combination with other semiconductors have been presenting improved results. Indeed, the cost-effectiveness, and sensitivity to longer wavelengths of light introduce metallophthalocyanines as emergent and attractive light-absorbing nanomaterial (Kolay et al., 2020). Considering these properties, metallophthalocyanines have been widely studied for their application as photocatalysts improver (Farooq et al., 2015), (Bian et al., 2020), (J. Sun et al., 2020), including in the integration with CQDs (Kolay et al., 2020), (S. Xu et al., 2021).

Herein, we present an eco-friendly, low-cost carbon-based source for the facile synthesis of CQDs. Furthermore, we investigate the potential applications of CQDs in photoelectrocatalysis and for that, we develop a photoelectrochemical system. Several analytical techniques were used to characterize the nanomaterials, as well as the CQD-assembled working electrode. Two hypotheses were tested here. First, we verified if the assembly of nickel phthalocyanine tetrasulfonic acid tetrasodium salt (NiTSPc) with CQDs would have a positive influence on the photoelectrocatalytic activity, such as the increase in photocurrent. The second concerned the quantity of CQDs assembled onto an indium tin oxide-covered glass (ITO) substrate, we presumed that more CQDs would improve the photocurrent response. The results confirmed that CQDs from lignocellulosic biomass have direct photoelectrochemical response under UV and blue light irradiation; moreover, NiTSPc also has increased the photocurrent improving the performance under acidic conditions. Also, a smaller amount of CQDs on the working electrode would better improve its performance. Furthermore, we proposed a mechanism for the photoelectrocatalytic behavior and to explain the role of light irradiation in the process.

2. BIBLIOGRAPHIC REVISION

2.1. Carbon quantum dots

2.1.1. The clarification of terms

The great scientific growth of research on carbon nanomaterials has outstanding positive aspects regarding the study of their properties and applications. However, efforts have been made to clarify some inconsistencies in definitions, nomenclature, and abbreviations, that could lead to misunderstandings among researcher groups (Cayuela et al., 2016). Although carbon-based nanoparticles appear to have similar optical properties, such as fluorescence, the mechanism of this phenomenon seems to be different. Therefore, we initiate by clarifying some important concepts.

At present, there is extensive use of the terms: semiconductor quantum dots (SQD), carbon quantum dots (CQDs), and graphene quantum dots (GQD). “Quantum dots” (QD) refers to semiconductor nanoparticles of sizes less than the Bohr radius i.e., the electron-hole pair of these particles is confined with quantized energy states. Therefore, “quantum dots” could refer to any type of nanoparticle or nanodot with a quantum confinement regimen, including carbon-based ones. Additionally, the difference between CQD and GQD relies upon their shape and precursors for the synthesis; CQDs are spherical and can be synthesized from other carbon-based nanomaterials, such as carbon nanotubes, or by pyrolysis of biomass; GQDs are π-conjugated single sheets and can be obtained from graphene-based materials (Cayuela et al., 2016).

2.1.2. Solid-state physics considerations

Solids are categorized as insulators, semiconductors, and conductors according to their ability to conduct electrical current. The band structure of these materials is different and has some fundamental characteristics. In insulators, there is a bandgap between the valence and conduction band, which is the cause for not conducting electricity (Figure 1). In semiconductors the bandgap is smaller; generally, a semiconductor material is considered a bandgap of up to 3.0 electron volts (eV) (Rogers et al., 2012).

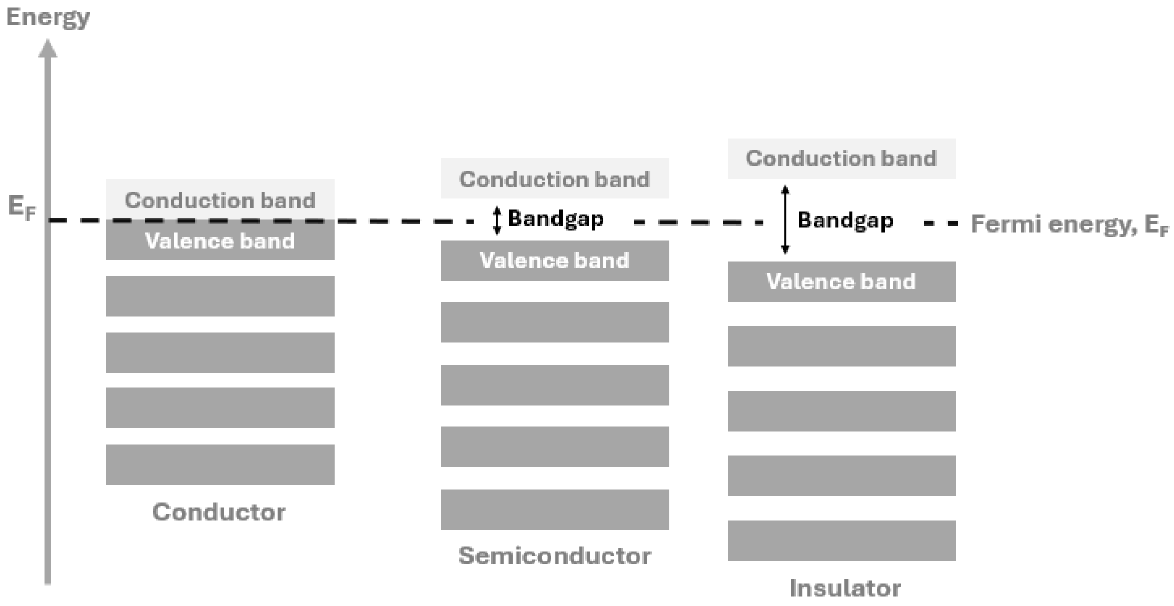

Figure 1. Band diagram for conductor, semiconductor, and insulator materials.

Source: Adapted from Rogers et al. (2012).

Conductor materials have valence and conduction bands with no gap between them, as a continuum of energy. The Fermi energy occurs in the middle of the higher band occupied, different from semiconductors and insulators, where they are in the bandgap. Electrons with energy right below the Fermi level can be easily excited under an electric field to levels right up the Femi level, justifying good conductivity (Fox, 2010). In the ground state, all allowed energy levels below the Fermi level are occupied and all that are above are empty (Rogers et al., 2012). The distribution of energy levels for bulk materials in comparison to atoms is much bigger; atoms have discrete energy levels. Therefore, if the idea is to work with a material whose electronic properties are like atoms, the alternatives are nanomaterials. The density of states (DOS) as a function of energy indicates that CQDs are between discrete atoms and bulk materials (Molaei, 2020b).

The size effect of CQDs under its electronic structure, theoretically investigated by Mandal et al. (2012), shows that, due to the quantum confinement, the highest occupied molecular orbital (HOMO) and the lowest unoccupied molecular orbital (LUMO) of the nanostructure can be dislocated to energy states more distant, increasing the bandgap. Also, functional groups can change HOMO and LUMO energy levels without significant changes in the bandgap.

Considering the electronic structure of semiconductors to elucidate the phenomenon of charge separation in CQDs, at room temperature, some electrons can have sufficient energy to jump from the valence band to the conduction band; in this case, the energy necessary for that could be thermal, from an applied electrical potential, or from the absorption of photons. In any case, when an electron is excited to the conduction band a “hole” (h^+) is formed in the valence band. The hole, because it is a physical vacancy, can assume a certain positive charge; thereby, an electron-hole pair is formed, also denominated as a quasiparticle, that is, exciton (Figure 2) (Rogers et al., 2012).

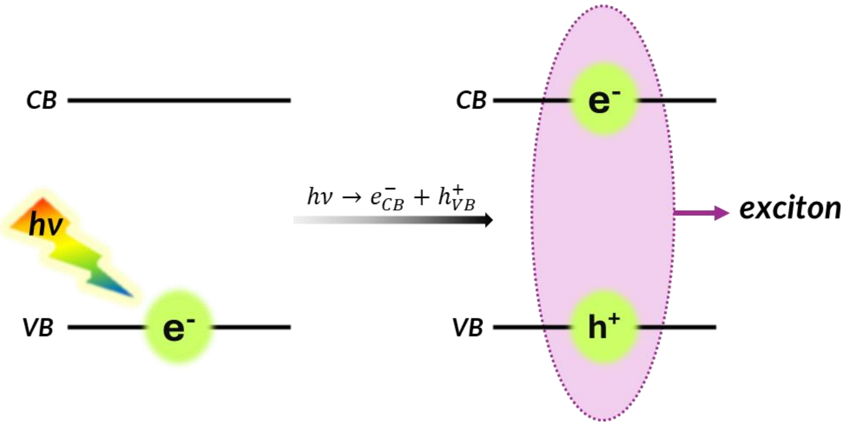

Figure 2. Schematic representation of the electron-hole pair (exciton) formation after the excitation with light (*hv*) of an electron from the valence band (VB) to the conduction band (CB).

Source: own author.

The motion of electron-hole pairs in quantum dots is restricted in three directions, the reason of sometimes is referred to as a zero-dimensional structure. In terms of size, the quantum confinement effects are observed in typical semiconductors with dimensions ≤ 5 nm (Fox, 2010). Quantum confinement in CQDs provides electrical and optical properties that are dependent on the size, which is directly related to their bandgap (Figure 3). Therefore, CQDs can be synthesized with different sizes covering a wide energy range from ultraviolet to infrared (García de Arquer et al., 2021).

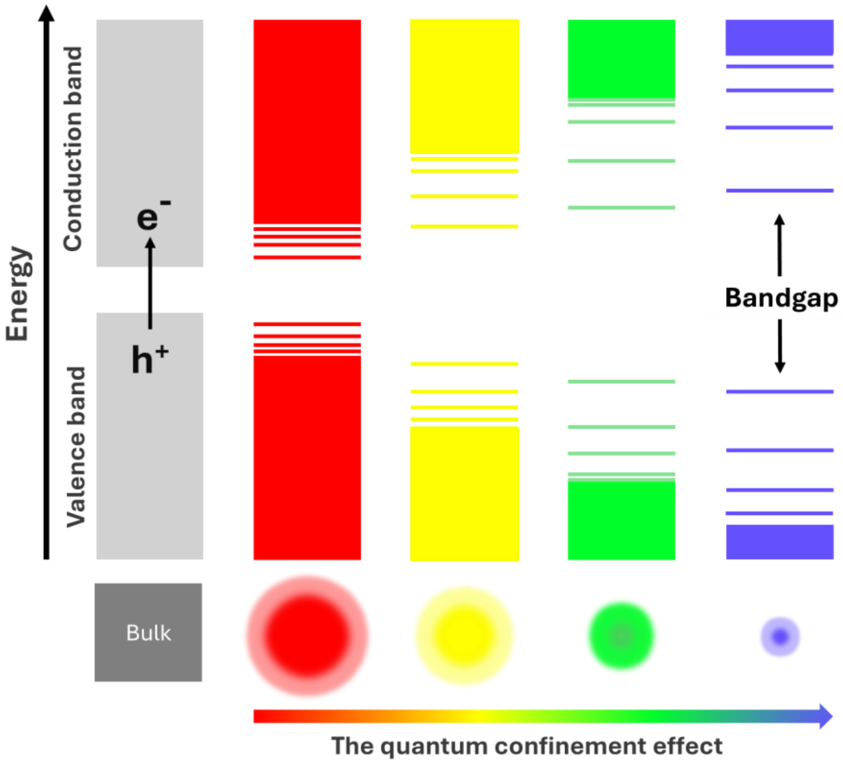

Figure 3. Quantum confinement effect, leading to size-dependent optical and electrical properties that are different from the bulk material, even if the compositions are the same. Decreasing the size of the nanoparticle, the energy levels are more discreet.
Source: Adapted from García de Arquer et al. (2021).

The size-dependent effect of CQDs can be observed when decreasing the size of the particle the bandgap increases, thus causing an increase in the energy. According to the relationship between bandgap and emission wavelength in Equation 1:

$$E = \frac{hc}{\lambda} \qquad \text{Equation 1}$$

where E is energy, h is Planck's constant, c is the velocity of light and λ is the light wavelength. A larger bandgap corresponds to higher energy transitions, meaning shorter wavelengths of light. The equation also explains the shift related to the emission of light after the excitation, that is, the Stokes shift. Since the wavelength of light is inversely proportional to emission energy, the loss of energy shifts the emission to longer wavelengths than the excitation wavelength. This phenomenon can be better understood with the Jablonski diagram (Figure 4).

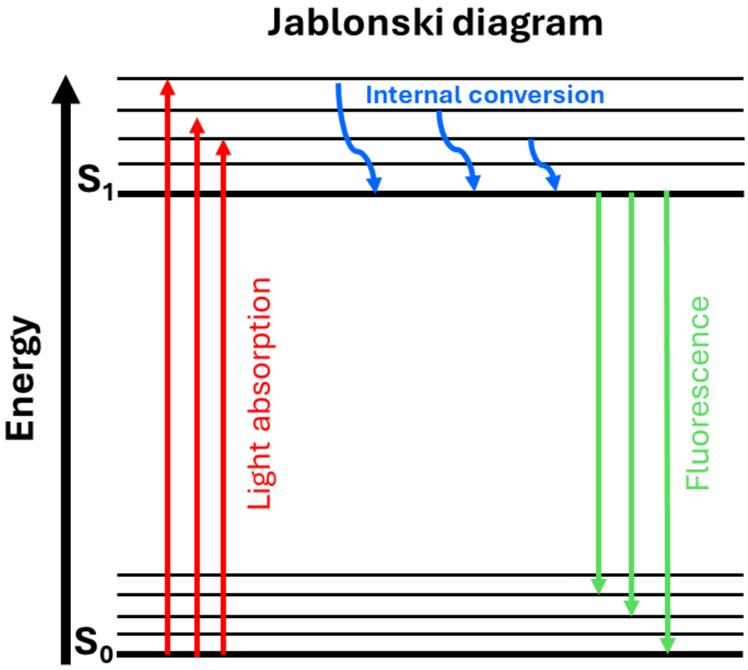

Figure 4. Jablonski diagram. After light absorption, non-radiative transitions (internal transitions) occur before the electron returns to the ground state; those transitions cause a loss of energy, and the emission of photons occurs with lower energy and longer wavelengths.
Source: Adapted from Lakowicz (2006).

The absorption of photons can excite electrons from the valence band to the conduction band. This process involves photoconductivity, which can occur on three basic mechanisms: i) formation of electron-hole pairs; ii) excitation of electrons from impurities in the nanomaterial; and iii) free-carrier absorption, where the number of carriers is the same, with increasing in conductivity due to a change in mobility (Singleton, 2001).

2.1.3. Optical features

As predicted by the quantum theory of radiation, when an atom absorbs or emits light there are two quantum states to be considered. When light is absorbed, the atom goes to an excited state and then spontaneously drops to a lower level, this process is called spontaneous emission. Fluorescence is a spontaneous emission process, an allowed transition that obeys the electric-dipole selection rules (Fox, 2010). These processes are the basis for understanding the optical features of CQDs.

2.1.3.1. Absorption properties

The π-conjugated electrons of the sp^2 atomic framework of CQD cause a large absorption capacity by photon-harvesting effect in short wavelengths. Also, the π-states can be related to aromatic sp^2-hybridized carbon present in their core; and the n-states are related to electron lone pair functional groups, such as carbonyls. Therefore, n-π* transitions can happen if the functional groups are bonded to the aromatic carbons (R. Wang et al., 2017). The absorption spectra of CQDs have typical peaks in the UV region (230-320 nm) and an absorption tail that can extend to the visible region (Y. P. Sun et al., 2006), (Thambiraja & Shankaran, 2016). The common peaks around 230 nm and shoulder at 300 nm are ascribed to the π-π* transition of aromatic C=C bonds, and n-π* of C=O bonds or other functional groups, respectively (Molaei, 2020b). The absorption characteristics can be different with size, composition, or altered by the surface passivation.

2.1.3.2. Fluorescence emissions: conjugated π-domains and surface defects

There are two proposed mechanisms for fluorescence in CQDs. The first associates fluorescence with the bandgap transitions of conjugated π-domains. This process occurs in the sp^2-hybridized framework rich in π-electrons and is referred to as the carbon core state emission; additionally, these transitions, are very determined by the nanoparticle size (Alafeef et al., 2024). When the π-domains decrease, the carbon core becomes smaller, then fluorescence emissions shift to the blue region. Likewise, when the carbon core and π-domains are increased, it happens the red shift of fluorescence (L. Wang et al., 2023).

The other proposed mechanism relates fluorescence with defects in the CQD structure. Surface defects are normally associated with a spherical model which is in boundary with the core carbon. This model is denominated as a spherical shell and predicts that around the carbon core surface functional groups, including oxygen-containing functional groups, preserve the linked structure (Figure 5).

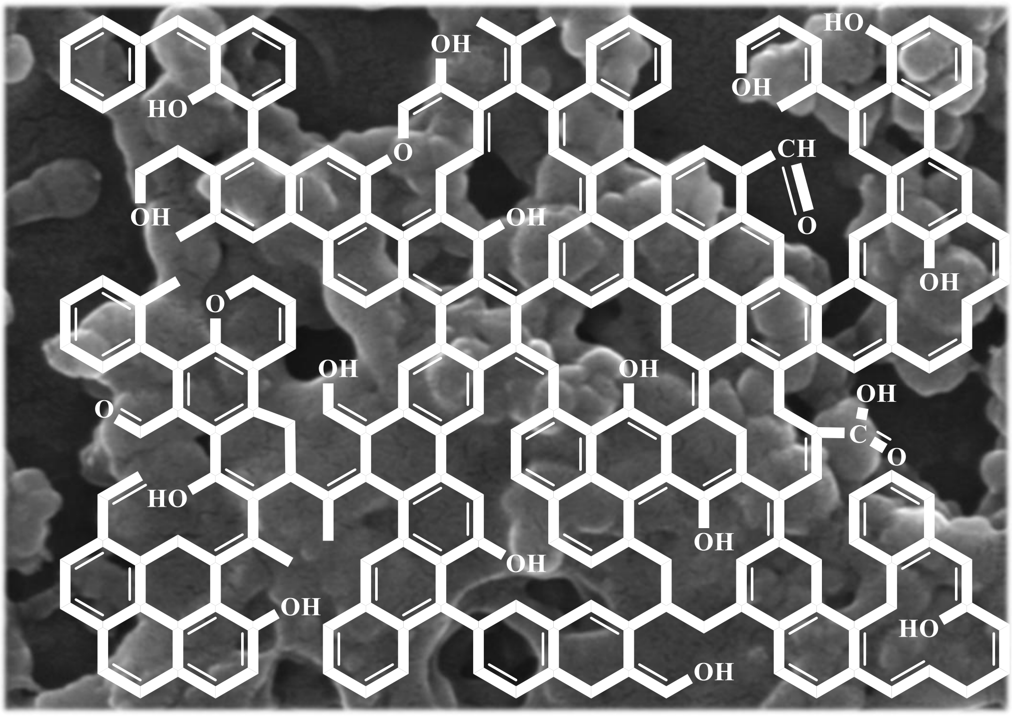

Figure 5. Schematic representation of functional groups, mostly oxygen-containing functional groups and structural defects.
Source: own author.

The surface defects are generally produced by the CQDs surface oxidation; the degree of oxidation can control the fluorescence acting as a center for the capture of excitons, or even as energy traps (Molaei, 2020a). Thus, the more defects the greater the number of emission sites and, consequently, the greater the fluorescence intensity (Alafeef et al., 2024). Ding and colleagues reported a hydrothermally synthesized CQD in one pot and separated *via* silica column chromatography that exhibited high optical uniformity. The fluorescence emission, in that case, was attributed only to the surface and surface states of the CQD; furthermore, they observed a decrease in bandgap with the increase in oxygen, that is, a redshift fluorescence arises as a result of the surface oxidation (Ding et al., 2016).

2.1.4. General aspects, sources, and applications

The CQDs were first obtained by Xu et al. (2004) during the purification of single-walled carbon nanotubes with electrophoresis. Years later, Sun et al. (2006) produced CQDs via laser ablation of a carbon target (mixture of graphite powder and cement hot-pressed) with tunable wavelengths. Thenceforth, umpteen studies were started to explore the properties and possible applications of these nanoparticles (H. Li et al., 2012), (S. Y. Lim et al., 2015), (R.

Wang et al., 2017), (L. Wang et al., 2023). CQDs are 0D nanoparticles with a size below 10 nm, with attractive optical characteristics like high photoluminescence emission, broadband absorption spectra, broad excitation wavelengths, and other features such as good conductivity, chemical stability, low toxicity, and biocompatibility (Wareing et al., 2021), (L. Wang et al., 2023).

Since the discovery, CQDs are synthesized from diverse sources, such as small organic molecules (W. Li et al., 2024), carbon fiber materials (T. Wang et al., 2023), lignocellulosic sources (Raju et al., 2023), (Fang et al., 2024); and by various methods (bottom-up or top-down), such as microwave method (Gholipour et al., 2024), electrochemical method (Yu et al., 2024), hydrothermal method (Setianto et al., 2024), combustion and pyrolytic carbonization methods (Ahlawat et al., 2023), (Y. Zhang et al., 2024). The use of biomass-based sources for CQD synthesis boosts the recycling of waste resources, as well as reduces the cost of the raw material; with this, environmental protection is improved. The CQDs prepared from waste sources normally have good biocompatibility and excellent fluorescence emissions characteristics (L. Wang et al., 2023).

Liu et al. (2014) successfully synthesized fluorescent CQDs from bamboo leaves with high performance for the detection of Cu^{2+}. The average size obtained was 3.6 nm in diameter with a narrow size distribution. The emission of blue color under UV irradiation (365 nm) followed by red-shift in emission after the excitation at higher wavelengths shows the excitation-dependent emissions property yet not fully understood, although several possibilities, including the quantum effect, that is, the optical selection of nanoparticles with different size. In the same idea for using CQDs for sensing, Yuan et al. (2015) evaluated the wide and potential applications in sensing/detection, biomedical labeling, and imaging. The CQDs were synthesized from wheat straw through the hydrothermal method; the nanoparticles showed great water-solubility and fluorescence properties. Using atomic force microscopy, the height was approximately 1.40 nm, in contrast with dynamic light scattering results, which showed an average hydrodynamic size of 1.7 nm. A shift to the red region was also observed in the study; when the excitation wavelength is increased from 304 to 364 nm the emission intensity decreases from 418 to 464 nm. The authors consider that the fluorescence is due to the intrinsic state emission, this conclusion was sustained by the absorption bonds and excitation-dependent emissions. In addition, the labeling and imaging tests demonstrated satisfactory results for applications in biomedical fields. Also, thirteen metal ions were used to study sensitivity, with Fe^{3+} showing the highest result, explained by the possible coordination between Fe^{3+} ions and surface negatively charged functional groups. Following a similar attempt for the sensing of metal ions, a group of researchers synthesized CQDs from several biomass sources, such as wheat, rice, Pennisetum glaucum, and sorghum (Chaudhary et al., 2016).

Zhu et al., (2020) used palm powder to synthesize CQDs, co-doped with sulfur and chlorine, through a one-step hydrothermal method. The product was found to be a hopeful candidate for photocatalyst methylene blue and rhodamine B degradation. As a possible mechanism for the degradation process, the authors consider the retarded recombination of electron-hole pairs which leads to the increase of free electrons that could react with adsorbed oxidants generating active oxygen radicals, in the case of oxygen; combined with the possibility for the holes to oxidize surface hydroxyl groups and water to produce hydroxyl radicals. As a result, there is a reaction with the dye molecules leading to its decomposition.

Rice straw waste was used to synthesize CQDs for sensing application by Kumari et al., (2024) through a sequence of thermal treatment. In the fluorescence emission study, the excitation wavelength from 280 to 340 nm showed the highest emission at 550 nm with excitation at 320 nm. The sensing of ellagic acid was performed and found a limit of detection of 0.2 nM; in this way, rice straw residue represents a cheap and eco-friendly source for CQDs synthesis.

Sugarcane biomass, a residue from the sugar alcohol industry and one of the most productive crop wastes in the world has the advantage production of value-added materials, like CQDs, due to its enormous source density, low cost, and stable and uniform properties (Chai et al., 2019). After the production process of sugar and alcohol, other residues like sugarcane molasses also can be used for the production of novel materials, such as CQDs (Huang et al., 2017). Several recent research shows the obtention of CQDs from sugarcane biomass (Qiu et al., 2022), (Kasinathan et al., 2022), (Deepanraj, 2024). Pandiyan et al., (2020) used sugarcane biomass to synthesize CQDs, following the hydrothermal approach, resulting in nanoparticles with spherical shape and average size of 1.7 nm. The nanomaterials were employed for antibacterial activities; the biocompatibility suggests that is suitable for photonic devices, bioimaging, and biomedical applications.

A multicolor fluorescence CQD from sugarcane waste was also synthesized over the hydrothermal method for mercury (II) ion sensing, and bioimaging; the suspension presented predominantly monodispersed spherical nanoparticles with size varying between 2 and 8 nm (Kasinathan et al., 2022). In another study, sugarcane biomass was used to synthesize CQDs to enhance the detection of organic molecules (Luo et al., 2024). Following the hydrothermal method, the obtained suspension was uniform without any noticeable aggregation; the particle size ranged from 1.5 to 5.5 nm with an average of 3.2 nm. The CQDs were used for the fabrication of a photodetector adopting a technique based on the ZnO seed layer by hydrothermal synthesis. A series of procedures was performed to obtain three photodetectors; comprehensive analysis highlights the advantages of the field of optoelectronics.

The major constituents of lignocellulosic biomass, like sugarcane biomass, are cellulose, hemicellulose, and lignin. These structures should play an important role in understanding the resulting CQDs, independently of the route of synthesis. Cellulose is a long-chain polymer composed of D-glucose with 1,4 glycosidic bonds; hemicellulose is composed of varied monosaccharide monomers; and lignin has several polyaromatic units composing a complex polymer (Shen et al., 2020). In the hydrothermal conversion of lignocellulosic structure, there is a successive break of hydrogen and glycosidic bonds to finally obtain the CQDs. Typically, the final product has a core of condensed polyaromatic structure with side chains rich in oxygen-containing functional groups (Shen et al., 2020), (Y. Liu et al., 2020).

Pyrolysis conversion of biomass in pyrolytic carbon followed by the acid treatment of the product results in CQDs like the hydrothermal products. Indeed, acid treatment shows a satisfactory process for the obtention of fluorescent carbon nanoparticles of different sizes just varying the reaction temperature (Peng et al., 2012). Also, the synthesis of CQDs from lignocellulosic biomass through the pyrolysis method results in excellent stability and strong fluorescence emission around 440 nm under excitation at 320 nm (Xue et al., 2016). However, considering that increasing the defects could also increase the fluorescence emission properties by the creation of excitons traps (Ding et al., 2020); acid treatment of pyrolytic product represents a favorable approach for obtaining CQDs with high fluorescence emissions. One may argue that another justification for chemical oxidation is the surface passivation with different functional groups, leading to an improvement in the dispersion of nanoparticle clusters, which can consequently increase fluorescence (H. Liu et al., 2007), (John et al., 2021).

Fluorescence emission is the most interesting phenomenon extensively investigated due to the viability of the substitution of inorganic fluorescent semiconductors already used at the time. The role behind this feature could lead to a valuable application in photoelectrochemistry; from the benefiting of the quantum size effect, these nanoparticles present noticeable properties for that use compared to other carbon materials (Z. Chen et al., 2022).

2.2. Photoelectrochemistry: basics and perspectives

The absorption of incoming light by an electrode excites the electrons from the valence band to the conduction band, then an electrochemical current is produced in the system; this is the phenomenon that photoelectrochemistry deals with. One may say that photoelectrochemistry is the link between solid-state physics and electrochemistry.

When the surface of a semiconductor is irradiated with light, the basic condition to produce a photocurrent is followed by the Equation 2:

$$h\nu > E_g \qquad \text{Equation 2}$$

Where E_g is the energy gap (bandgap) of the semiconductor and $h\nu$ is Planck's constant multiplied by the frequency of the striking light (Bockris & Reddy, 2004). For an electron jump to the conduction band, the energy of incident photons should be superior to the energy gap between valence and conduction bands.

In recent decades, several electrochemical systems have been studied with semiconductor electrodes; the reason is very clear, we can take advantage of solar light to facilitate the occurrence of reactions. The major interests are concerning the synthesis of value-added products (Sendeku et al., 2024) and photoelectrochemical water splitting and CO_2 conversion (T. W. Chen et al., 2024). Different types of materials are used for this purpose, such as carbon (Yan et al., 2020), (Aragaw, 2020), (Blaskievicz et al., 2024); perovskites (Bienkowski et al., 2024), (Z. Wang et al., 2021); and metal oxides (Xia et al., 2021), (C. Li et al., 2020). However, a lot of concerns about stability, decomposition, and costs have been a reason to search for new materials with improved properties.

More recently, due to their advantageous properties, carbon nanomaterials have been extensively used to improve photoelectrochemical reactions (Z. Zhang et al., 2015), (Prakash et al., 2019), (Alenad et al., 2023), (Ahmed et al., 2024). The structure of synthesized CQDs is excellent in terms of improving photoelectrochemical processes including rich optical properties, abundant catalytic active sites, electrical conductivity, charge coupling effect, surface charge localization, rich optical properties, and others (Z. Chen et al., 2022). Considering these several advantages, CQDs can be used as photosensitizers, photocatalysts, and supporting materials, or coupled with other semiconductors to prepare junction electrodes.

2.3. Applications of carbon quantum dots in photoelectrocatalysis

As a result of the considerable optical and electronic characteristics of CQDs, several researchers focus on their utilization in photocatalytic or photoelectrochemical systems. It is worth highlighting the difference between these processes; photocatalyst systems involve the use of a semiconductor powder, suspended in an aqueous solution; in the photoelectrochemical system, the semiconductor powder should be immobilized in the electrode or have been synthesized directly onto the electrode surface (H. Wu et al., 2020). As a simple example, a single-particulate photocatalyst system can work as follows: an electron is excited via photons incidence, where the photocatalytic reduction occurs by the photogenerated electrons and a photocatalytic oxidation happens with the photogenerated holes (Figure 6) (Yoshino et al., 2022).

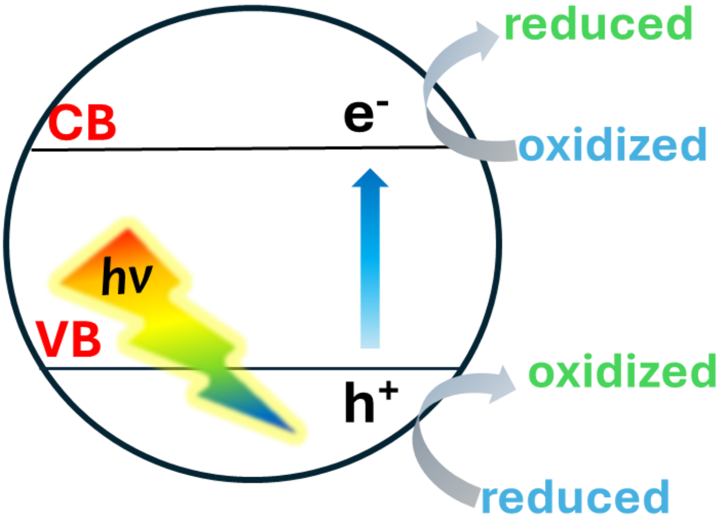

Figure 6. Single-particulate photocatalyst absorbing photons (hν) and exciting electrons from the valence band (VB) to the conduction band (CB), then generating electron-hole pairs. The photogenerated holes and electrons can oxidize and reduce reactants, respectively.
Source: own author.

Considering that a photoelectrocatalytic process requires the formation of light-induced electron-hole pairs, CQDs end up becoming potential candidates for such an application. Due to their fluorescence characteristics and photoinduced electrons, CQDs are used to construct high-performance photoelectrocatalysts. (Ali et al., 2022). In addition to acting as a mediator in the charge transfer process, it can also serve as a photosensitizer or even as the only photoelectrocatalyst in a photoelectrocatalytic process (R. Wang et al., 2017). Moreover, the photocatalytic behavior of CQDs can be explained by the possibility of some functional groups, like carboxylic acid and carbonyl, inducing the upward band bending, consequently reducing the electron-hole pairs recombination (Z. Wang et al., 2017).

Several studies have been conducted using CQDs for photocatalytic systems. H. Y. Wang et al., (2021) synthesized CQDs from sodium ethylenediaminetetraacetic acid through the hydrothermal method for application in water splitting. N. Wang et al., (2023) have synthesized via hydrothermal method from three different precursors: 3-aminopropanoic acid, 4-aminobutanoic acid, and 6-aminocaproicacid for water oxidation. Finally, Y. S. Zhang et al., (2023) prepared CQDs by hydrothermal process of 1- butyl-3-methylimidazolium chloride for H_2O_2 production. These three related studies conducted the photocatalytic process under irradiation of UV and visible light and reported that in the absence of any other traditional electrolyte show a new facile strategy and adapt the photoactivity in a robust and durable pathway (H. Y. Wang et al., 2021). From another perspective, J. Xu et al. (2023) built heterojunction photoanodes with TiO_2 and CQDs for photoelectrocatalytic wastewater treatment. The CQDs synthesized from glucose were deposited onto fluorine-doped tin oxide (FTO) conductive glass using Nafion®117 solution as ligand. Industrial wastewater was used as a sample with a total organic carbon content (TOCC) of 100,000 mg L^{-1}; after 8 hours, the optimal CQD/ TiO_2 photoanode achieved 93 % TOOC removal.

For photoelectrochemical water splitting, Kumar's group developed a Chl/CQDs_SiNW photocathode onto a silicon nanowire (K. Roy et al., 2020). Compared to the pristine device (1.46 mA/cm^2), Chl/CQDs_SiNW presented an increase of photocurrent density up to 26.36 mA cm^2 at an external bias of 1.07 V versus a reversible hydrogen electrode. In their system, CQD acts as an electron donor, while Chl acts as an acceptor. In another study, for photocatalytic reduction of CO_2, J. Zhang et al. (2021) used TiO_2 nanotubes (NTs) electrodes and CQD from biomass. The system with CQDs exhibited the highest CO_2 photoreduction with the CO and CH_4 yields of 13.55 and 3.54 μmol g^{-1} (2.4 and 2.5 times that of TiO_2 NTs, respectively). With nearly 100 % conversion of carbon dioxide to methanol by pure water, Y. Wang et al. (2020) used CQDs synthesized by microwave method and carbon nitride as catalysts. The photoconversion achieved a selectivity of 99.6 ± 0.2 %; this work paves the way for sustainable production of methanol, which is a valuable hydrogen source for energy generation.

In the case of the photoelectrocatalytic process, numerous researchers have been reporting outstanding results in the application of CQDs for several purposes. In this way, this could represent a more effective approach considering the reutilization of the used electrode. On the other hand, the use of suspension-containing CQDs can lead to more residue generation, depending on the system's long-term stability. However, the fabrication of working electrodes containing CQDs remains a hard approach because of two main technical features: the use of transparent material as support for CQDs immobilization; and the immobilization itself.

3. AIMS AND OBJECTIVES

3.1. Research aim

The general objective of this work was to synthesize CQDs from sugarcane biomass for application in photoelectrocatalysis.

3.2. Research objectives

To obtain fluorescent CQDs from sugarcane biomass through pyrolysis followed by acid treatment.

Investigate structural and chemical properties of the synthesized CQDs by dynamic light scattering, zeta potential, and Raman, infrared, UV-Vis, and fluorescence spectroscopy.

Calculate the bandgap of the CQD and understand the absorption and fluorescence properties for application in photoelectrochemical reactions.

Develop a working electrode with CQDs, as well as build a photoelectrochemical system to perform the measurements.

Investigate the influence of NiTSPc conjugation with CQDs on the photoelectrocatalytic performance of the working electrodes.

Elucidate the mechanism of photoelectrocatalysis for electrodes with the best performance.

4. EXPERIMENTAL PROCEDURE

4.1. Reactants and equipment

The reactants and equipment used in this research are presented in Tables 1 and 2. The experiments and characterizations were done at the Bioelectrochemistry and Interfaces Group of the São Carlos Institute of Chemistry, University of São Paulo, and Central de Análises Químicas Instrumentais at the same institute.

Table 1. List of equipment used for the synthesis of carbon quantum dots, production of working electrodes, and photoelectrochemical studies.

Reactants/materials	Source
Sulfuric acid 98 %	Sigma-Aldrich
Nitric acid 65 %	Sigma-Aldrich
Hydrochloric acid 37 %	Fluka
Argon	Linde
Nitrogen	Linde
Ethanol > 99,5 %	Sigma-Aldrich
Potassium hydroxide	Sigma-Aldrich
Indium tin oxide coated glass slide (15-25 Ω/sq)	Sigma-Aldrich
Ammonium hydroxide	Êxodo científica
Hydrogen peroxide	Êxodo científica
Poly (allylamine hydrochloride)	Sigma-Aldrich
Nickel (II) phthalocyanine-tetrasulfonic acid	Sigma-Aldrich

Source: own author.

Table 2. List of equipment used for the synthesis of carbon quantum dots, production of working electrodes, and photoelectrochemical studies.

Equipment	Manufacturer
Tube Oven	-
Magnetic stirrer K40-3020	Kasvi
UV chamber	Jasco
UV-Visible spectrophotometer V760	Jasco
Spectrofluorometer F-4500	Hitachi
Multiline Raman Spectrometer	Horiba
Potentiostat/Galvanostat PGSTAT204	Autolab
Field Emission Scanning Electron Microscope JSM 7200F	JEOL
Fourier-transform infrared spectrometer	Bruker

Source: own author.

4.2. Synthesis of carbon quantum dots

Sugarcane biomass was collected from a local market in São Carlos, São Paulo, Brazil. The biomass was cut into small pieces (1 cm x 1 cm x 1 cm) and dried at 120 °C for 2 hours to remove humidity. Then, the material was turned into a graphitic-like structure through pyrolysis at 1000 °C under an argon atmosphere for 30 minutes (heating rate of 5 °C min $^{-1}$).

For the obtention of CQDs, the pyrolytic material was treated with H_2SO_4 and HNO_3 (3:1 V/V) for 24 hours at 75 °C ± 5 °C, under constant stirring. After that, a suspension of CQDs is obtained. The suspension was diluted with deionized water, adjusted to pH = 7.0 with

KOH, and filtered with a 0.22 µm membrane filter (Figure 7). This suspension was used to perform all characterizations and experiments.

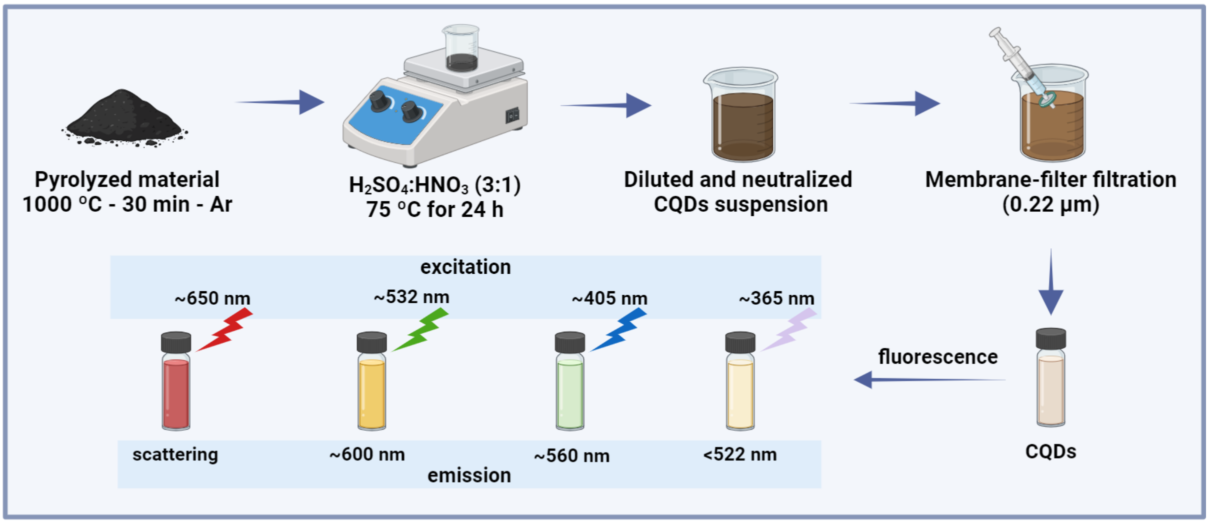

Figure 7. Schematic representation of CQDs synthesis route. Pyrolyzed material was obtained following acid treatment, dilution, and filtration. After this process, the CQDs were ready for characterization and applications.

Source: own author.

To obtain the CQDs concentration, some quantity of the suspension was dialyzed over three days. After that, three aliquots (1.0 mL) were cooled down with liquid nitrogen and freeze-dried overnight; then, the average mass of the resulting powder was 1.43 mg, consequently, the concentration was 1.43 mg mL^{-1}.

4.3. Spectroscopic and structural characterization

4.3.1. Fluorescence studies

Measurements of fluorescence spectroscopy were performed on a spectrofluorometer F-4500. Emission spectra were obtained at different excitation wavelengths (λ_{exc}) (410 – 541 nm). Slit opening of 10 nm. Fluorescence induced by UV lamp (365 nm) and lasers (405, 532, and 650 nm) were done to understand features related to the emission wavelength different from that of excitation i. e. Stokes shift.

4.3.2. Ultraviolet-Visible spectroscopy

Absorption spectroscopy analyses were carried out on a Jasco-V 760 spectrophotometer, using quartz cuvettes with an optical path length of 10 mm. The wavelengths varied in the range of 200 to 800 nm.

4.3.2.1. Tauc plot and Urbach tail

Using the UV-Vis data, we perform the Tauc plot to determine the bandgap value of the nanomaterial and analyze the Urbach tail. With the Tauc method, the bandgap value can be also denominated optical gap (E_{opt}) or Tauc gap (E_g). The following expression, Equation 3, describes the dependence of the absorption coefficient ($\alpha(E)$) to the photon energy ($h\nu$) near the band edge.

$$\alpha(E)h\nu \propto \left(h\nu - E_{\mathrm{opt}}\right)^2 \qquad \text{Equation 3}$$

This expression was used to determine the bandgap value by plotting: $(\alpha h\nu)^2$ *versus* $h\nu$. The E_{opt} was found by extrapolating the linear part of the plot until reaching the x-axis ($\alpha(E) = 0$). Extrapolation is due to two reasons: the exponential decay of $\alpha(E)$ in the bandgap (Urbach tail), a behavior always present in amorphous semiconductors; and due to the presence of a weak absorption tail, which overlaps interband absorption at lower energies (< 4 eV) (Klein et al., 2023).

4.3.3. Raman spectroscopy

Raman spectra were obtained on the Horiba Multiline Raman Spectrometer, LabRam Evolution. The analysis was carried out both for pyrolyzed material and CQD. For CQD, a certain amount of the suspension was cooled down with liquid nitrogen and freeze-dried overnight; the obtained powder was used for analysis. Measurements were performed in the range of 500 to 2500 cm^{-1}, using an excitation wavelength of 633 nm.

The $I_D|I_G$ ratio was determined to discuss the structure disorder related to the presence of defects, where I_D and I_G are the intensity of bands D and G, respectively.

4.3.4. Fourier-transformed infrared spectroscopy

Fourier-transformed infrared spectroscopy (FTIR) was carried out to identify the functional groups in the CQD surface. The vibrational spectra in the infrared region were obtained using the Hyperion 3000 Microscope equipment, coupled to the Vertex 70 V infrared spectrometer. 5 μL of the CQDs suspension was deposited on a gold-coated plate and dried in a vacuum desiccator for 15 min. The spectra were obtained in the range of 500 to 4000 cm^{-1}.

4.3.5. Dynamic light scattering and zeta potential

Dynamic light scattering (DLS) technique was used to determine the hydrodynamic diameter of CQDs. The following parameters were used: material refractive index of 2.42; refractive index of the dispersant (water) of 1.33; and material absorption value of 0.001. This characterization was complementary to the transmission electron microscopy analysis.

Zeta potential was determined to better evaluate the stability of the suspension in terms of repulsive and attractive interactions. Both analyses were carried out on Malvern Zetasizer Nano series equipment.

4.4. Photoelectrochemical characterization of carbon quantum dot suspension

4.4.1. Photoelectrochemical system

To perform all the photoelectrochemical-related studies we developed a photoelectrochemical cell and a modified platform for light irradiation (Figure 8). A 3-D model of the cell was projected in Tinkercad® and the prototype was built at the mechanical workshop (IQSC-USP). The cell has 14 mL of internal volume capacity and the side from which the light is irradiated has a quartz window that prevents the absorption of ultraviolet and visible wavelengths. The two commercial light sources (UV 365±10 nm and blue 405±10 nm) for photoelectrochemical studies had very unstable light power due to the discharge of the batteries during the analysis. This problem motivated us to set up a homemade modified platform for light irradiation using those two commercial light sources. The platform has a power source that converts the 220/110 V to 3.0 V, which supports stable light irradiation, and a regulator of light intensity as well.

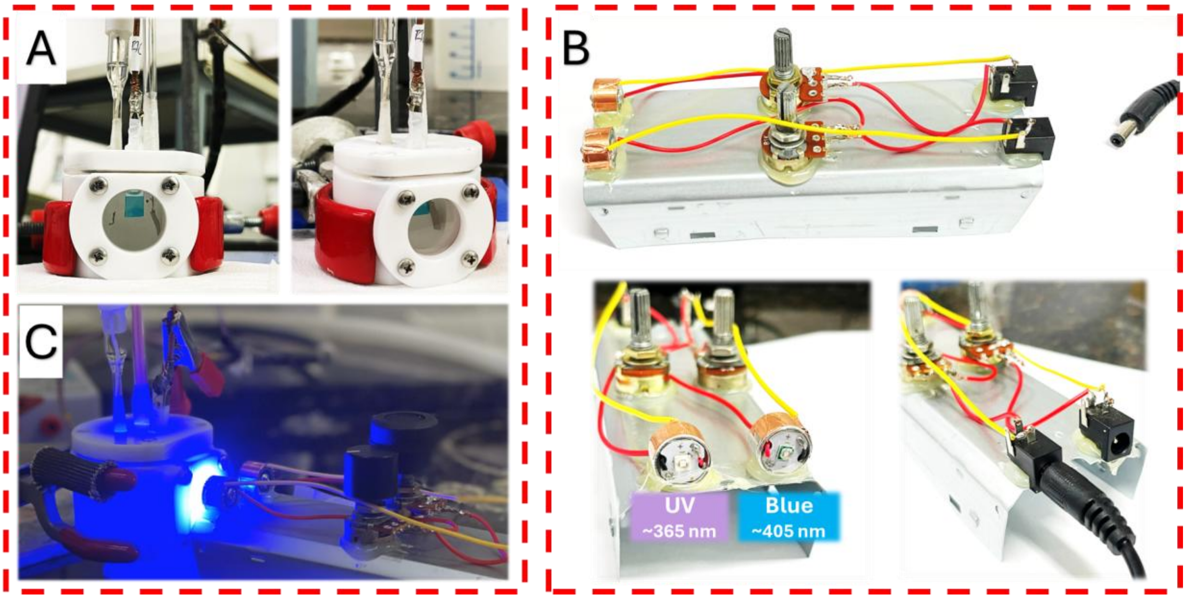

Figure 8. (A) Front view of the photoelectrochemical cell showing the quartz window, (B) homemade platform for light irradiation, and (C) photoelectrochemical system in operation with 405 nm light irradiation.
Source: own author.

4.4.2. Influence of concentration and pH in photoelectrochemical properties

To evaluate the influence of CQD concentration in the electrolyte, different CQD solutions were prepared. A diluting solution of the salts, also used as the electrolyte, was prepared considering the same concentration present in the CQDs suspension. The concentrations analyzed were: 68.1, 186.5, 286.0, 476.7, and 1,430 µg mL^{-1}. This last one was the pure CQD suspension. The pH study was performed varying the pH of the CQDs suspension from 2 to 12 with HCl and NaOH. Cyclic voltammograms (0.0 to 1.0 V, scan rate of 10 mV s^{-1}) were recorded, in dark and 405 nm light irradiation, using ITO as working electrode, Ag/AgCl (3 M KCl) as reference electrode, and platinum (Pt) as counter electrode.

4.5. Photoelectrochemical study

4.5.1. Working electrode fabrication

To investigate the photoelectrochemical performance of CQDs we fabricated two types of working electrodes: one consisting only of CQDs and another consisting of both CQDs and NiTSPc. The coupling of CQDs and NiTSPc was made to investigate if there is a synergistic interaction between them, which could form a strong conjugated system through π-π interaction.

Layer-by-layer (LbL) technique was used to prepare the working electrodes. LbL consists of the deposition of oppositely charged structures in a surface through alternating layers. Before the film formation steps, the ITO slide, from Sigma Aldrich, was cut into 7x25 mm and cleaned by the basic hydrophilization method, as follows: ammonium hydroxide, hydrogen peroxide, and water, in a ratio of 1:1:6, were placed in a petri dish. Then, the slides were immersed in the solution and heated up to 80 °C, for 15 min; afterward, they were rinsed with deionized water and dried at room temperature.

The methodology to prepare the working electrodes is summarized in Figure 9. CQDs films were prepared as follows: ITO slide was rinsed in a solution of poly (allylamine hydrochloride, PAH) (0.5 g L^{-1}) for five minutes, used as a cationic electrolyte, then rinsed in an HCl solution (pH = 2.5) to remove the excess of PAH and dried with nitrogen gas. This process consists of the formation of one layer. After that, the ITO was rinsed in the CQDs suspension for five minutes, then rinsed in the HCl solution to remove the excess of CQDs and dried with nitrogen again; this resulted in the formation of another layer. These two processes combined form one bilayer; 15 and 30 bilayers were produced, resulting in two working electrodes ITO/CQD_{15} and ITO/CQD_{30}, respectively (Schema I, Figure 9). For the electrodes with NiTSPc, the methodology was similar: 15 bilayers of CQDs were formed, then more 15 bilayers of NiTSPc were formed on top, resulting in the $ITO/CQD_{15}/NiTSPc_{15}$ working electrode (Schema II, Figure 9). Finally, in another ITO slide, 15 bilayers of NiTSPc were formed in ITO, then more 15 bilayers of CQDs were formed on top, resulting in the $ITO/NiTSPc_{15}/CQD_{15}$ working electrode (Schema III, Figure 9). In brief, four working electrodes were produced: ITO/CQD_{15}, ITO/CQD_{30}, $ITO/NiTSPc_{15}/CQD_{15}$, and $ITO/CQD_{15}/NiTSPc_{15}$.

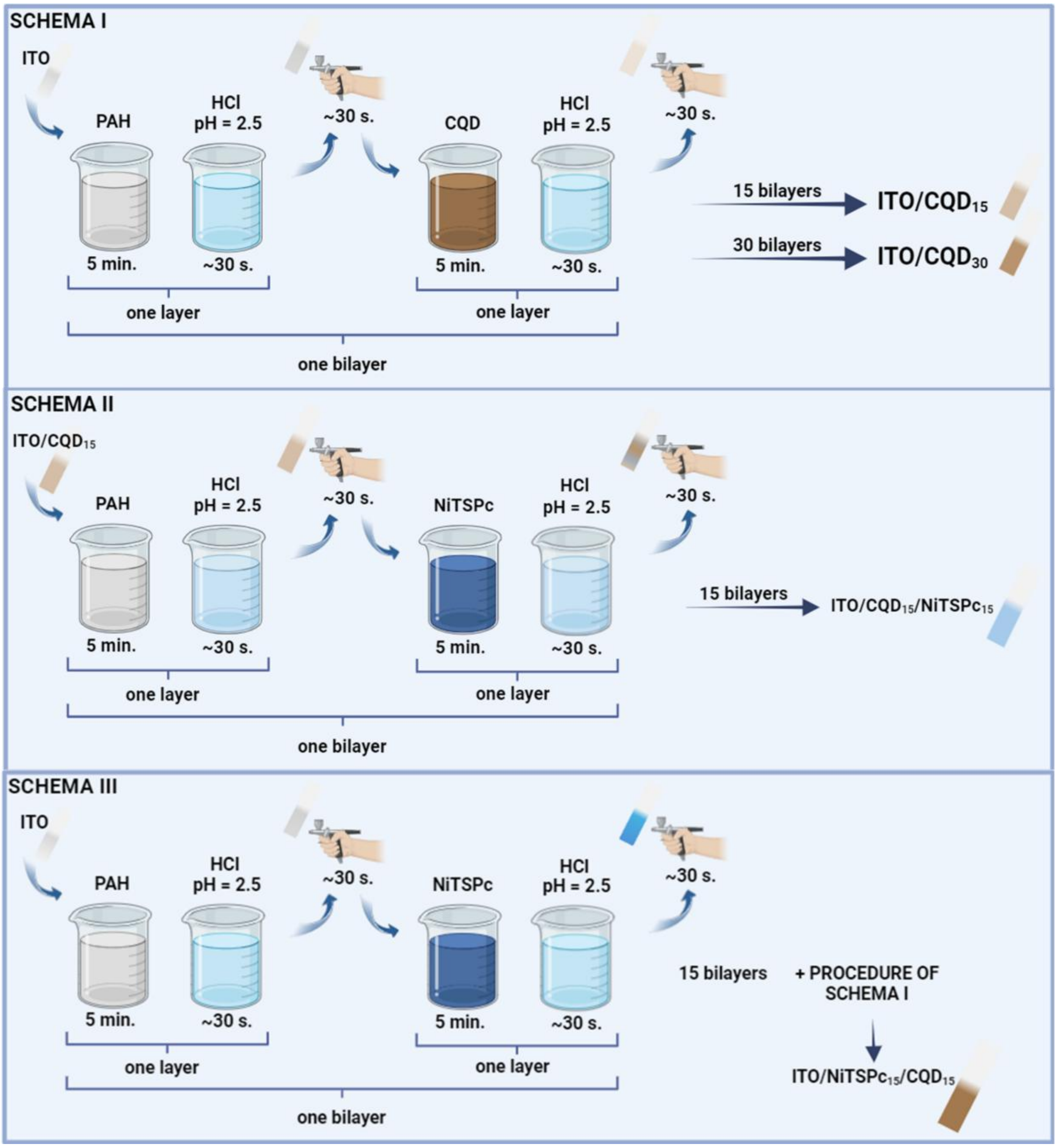

Figure 9. Schematic representation of routes to produce working electrodes. Schema I show the procedure to produce electrodes containing only CQDs. Schemas II and III show the procedure to obtain the electrodes with CQDs and NiTSPc conjugates.

Source: own author.

4.5.2. Measurements and instrumentation

Photoelectrochemical measurements were performed using an electrochemical workstation (Autolab potentiostat) driven by Nova 2.1 software. A three-electrode configuration was used with Ag/AgCl (3 M KCl) as the reference electrode and Pt as the counter electrode. All the experiments were performed using the home-built photoelectrochemical system (Figure 8C). Electrolytes were prepared using deionized water supplied by a Milli-Q purification system (Millipore). Cyclic voltammetry (CV) tests were conducted under two pHs: HCl (pH 1.0) and carbonate/bicarbonate buffer (pH 9.6). The CV curves were recorded at the scan rate of 10 mV s^{-1} in the scan range of 0.2 to 1.2 V. Photocurrent was obtained from chronoamperometry with an externally applied bias of 1.0 V (vs Ag/AgCl) for 220 seconds, under the pH mentioned.

5. RESULTS AND DISCUSSION

5.1. Structural and optical features of carbon quantum dots

5.1.1. Raman spectroscopy

Raman spectra were acquired for pyrolyzed material and CQDs. Figure 10A shows the spectra for the pyrolyzed material, presenting two bands at 1320 and 1590 cm^{-1}. Bands shifted to these wavenumbers are common for carbon allotropes, due to chemical composition and structural organization, which confer similar vibrational modes.

The G band, at 1590 cm^{-1}, is associated with the in-plane stretching of the carbon rings (C-C), typical of sp^2 graphitic structures. The aforementioned stretching occurs within the Brillouin zone by phonons that are activated with resonant electron-phonon scattering (Jorio & Souza Filho, 2016). The D band, at 1320 cm^{-1}, is associated with the breathing modes from carbon rings. This mode becomes active in Raman due to the presence of defects in the sp^2 carbon structure of the nanomaterial; besides, the intensity of the D band is proportional to the density of defects (Szybowicz et al., 2018).

To evaluate the disorder related to defects in the material structure the ratio $I_D|I_G$ is used. The value found of 1.00, for pyrolyzed material, reveals that there is a high defect density, which was formed in the pyrolysis stage. Nevertheless, after the acid treatment (Figure 10B), for the obtention of CQDs, the $I_D|I_G$ ratio increased to 1.97, evidencing the increase in surface defects and the formation of oxygen-containing functional groups, carbonyl, carboxyl, and hydroxyl groups into the basal and edge planes, as evidenced by the appearance of D1, D2, D3 and G’ bands (Peng et al., 2012), (Claramunt et al., 2015), (Rajender & Giri, 2016); this is also denoted by the FTIR result, presenting bands related to these groups.

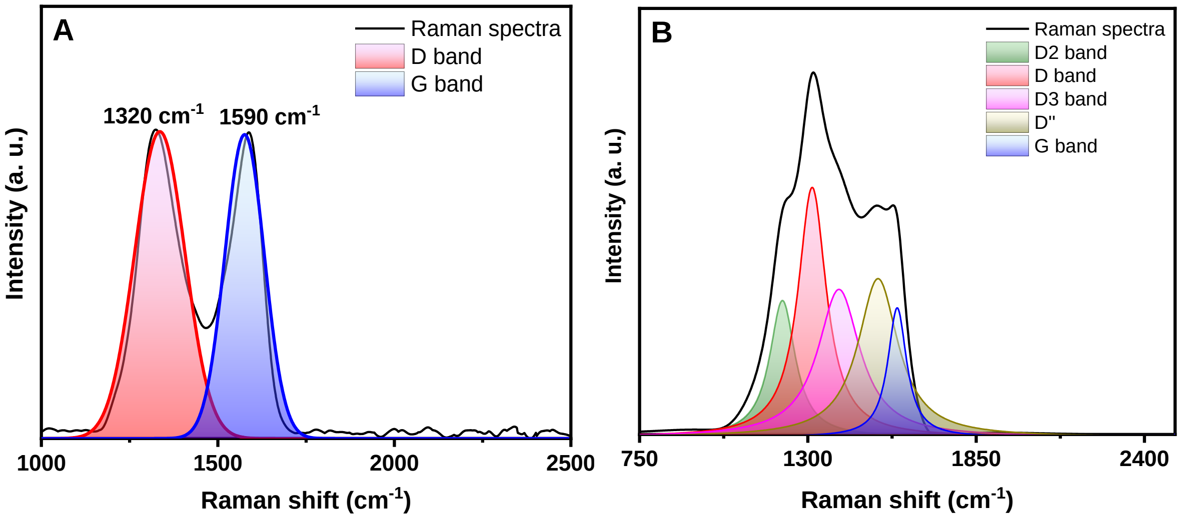

Figure 10. (A) Raman spectra of pyrolyzed material presenting D and G bands. (B) Raman spectra of CQDs. In this one, bands (green, magenta, and brown) other than D and G appear due to the increase in surface defects.

Source: own author.

In addition to acid treatment, other processes for synthesizing CQDs from biomass can generate products with a high density of defects, such as in a heated alumina bath (γ-Al_2O_3) (Brachi, 2020). In this synthesis, the author obtained a $I_D|I_G$ ratio of 1.79; this suggests defects not only on the surface but also in the internal structure of the nanomaterial, in addition to the presence of sp^2 sites and combined sp^2-sp^3 bonds. The X-ray photoelectron spectroscopy (XPS) characterization carried out in the work also showed the composition of 31.1 % oxygen in the nanomaterial, attributed to the presence of C-O, O-H, and C=O groups (Brachi, 2020).

5.1.2. Fourier-transformed infrared spectroscopy

FTIR spectra, shown in Figure 11 and Table 3, highlight the vibrational modes identified for CQDs. The majority are associated with oxygen-containing functional groups.

The broad band around 3470 cm^{-1} is assigned to the O-H stretching mode from water molecules. Stretching modes for oxygen bonds are observed in the regions of 1077 cm^{-1} (υ_{C-O}), 1365 cm^{-1} (υ_{C-O-C}), 1392 cm^{-1} (υ_{COO-}), 1586, and 1715 cm^{-1} ($\upsilon_{C=O}$), revealing the presence of oxygen groups in several types of functional groups, such as carbonyl, ether, and carboxylate in the CQD surface (Xue et al., 2016), (Jing et al., 2019), (X. Feng & Zhang, 2019). Furthermore, the presence of C-H out-of-plane bending between 750 and 875 cm^{-1}, and C=C stretching around 1655 cm^{-1} reveals the existence of aromatic rings in the structure of CQDs (Jing et al., 2019).

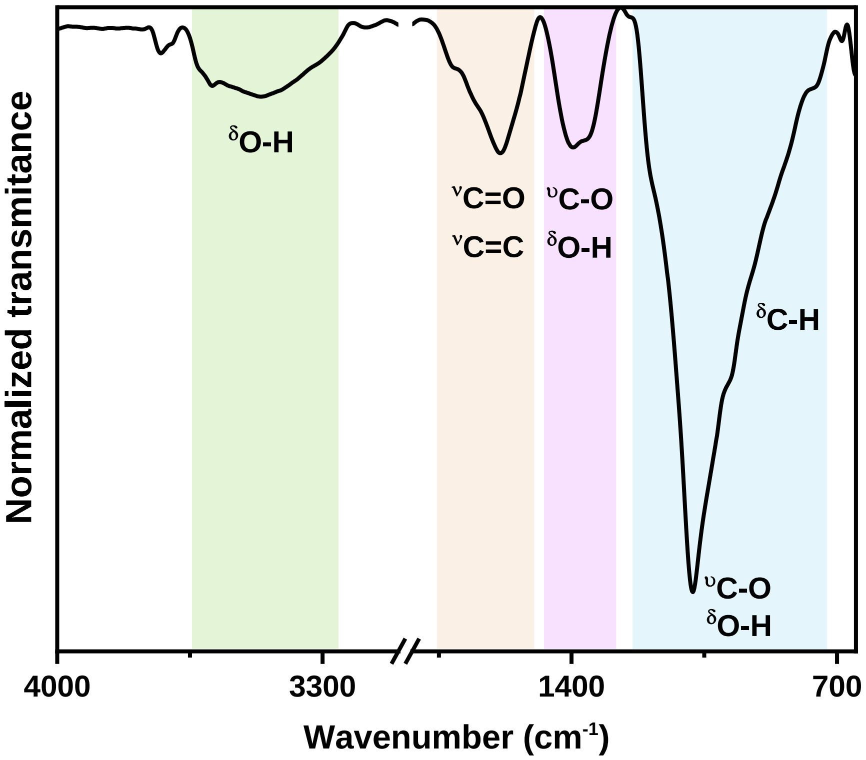

Figure 11. FTIR spectra of CQDs. The assignments reveal the constitution of oxygen-containing functional groups.

Source: own author.

Table 3. Vibrational modes identified in the FTIR spectra of CQD from lignocellulosic biomass.

Wavenumber (cm^{-1})	Assignment	Reference
750 - 875	Bending C-H out-of-plane	(Jing et al., 2019)
1077	Stretching C-O; O-H	(Xue et al., 2016); (Jing et al., 2019)
1365	Stretching C-O-C; O-H	(Y. Liu, Xiao, et al., 2014)
1392	Stretching COO-; O-H	(Xue et al., 2016); (Jing et al., 2019)
1586	Stretching C=O	(Pandiyan et al., 2020)
1655	Stretching C=C	(Xue et al., 2016)
1715	Stretching C=O	(F. Wu et al., 2016)
3470	Stretching O-H	(Xue et al., 2016)

Source: own author.

Functional groups in basal and edge planes increase the solubility of CQDs in water, consequently influencing the suspension stability. Furthermore, the interaction between the carbon core and the surface functional groups plays an important role in electron transfer, including in reactions photocatalyzed by CQDs (R. Wang et al., 2017). The surface functional groups can be protonated or deprotonated in a reaction medium depending on the pH, thus increasing the electron dissipation effect. In this way, the functional groups can act like traps, prolonging electron-hole separation and increasing photocatalytic activity for oxygen reduction (Z. Chen et al., 2022), for degradation of organic dyes (Han et al., 2020), (Nizam et al., 2023), and hydrogen evolution reaction (S. Xu et al., 2024). The presence of these groups will play an important role in further discussions about fluorescence properties.

5.1.3. Size distribution and surface charge

DLS and zeta potential analyses were performed to determine the hydrodynamic radius and the degree of electrostatic repulsion of the CQDs suspension, respectively. The size distribution of CQDs (Figure 12) shows that the nanoparticles had sizes of approximately 1.06 nm. This result is evidence that the synthesis route used leads to the obtention of CQDs with sizes at the nanoscale. The polydispersity index (PDI) value of 0.458 is similar to that found in the literature (Yuan et al., 2015).

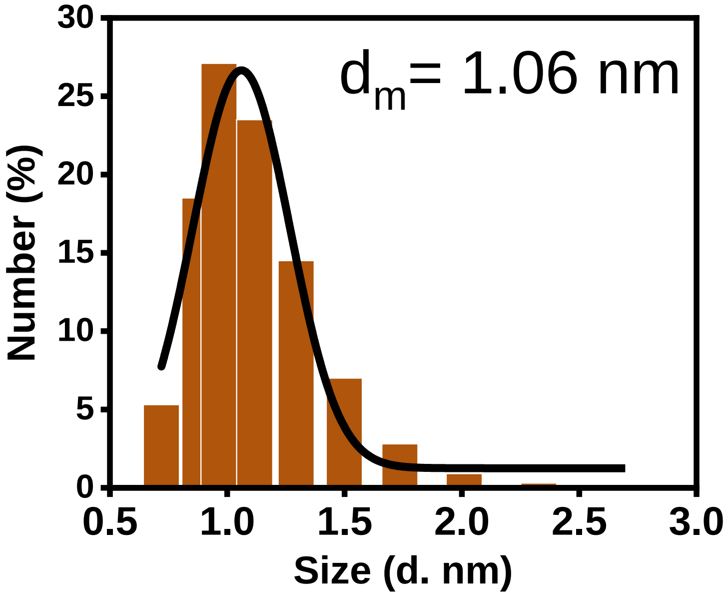

Figure 12. Hydrodynamic diameter distribution histogram of CQDs suspension obtained by DLS revealing the nanoscale size of the particles.

Source: own author.

The found value of zeta potential was -22.6 mV. The obtained CQDs are stable due to the negative electrostatic repulsion and negatively charged oxygen-containing functional groups are decorated onto the CQD surface. The value obtained here is more negative compared to that found in the literature (-4.27 mV (Huang et al., 2017); -17.5 mV (Setianto et al., 2024)) what can be related to the acid treatment used in this work that increases the surface oxidation (increasing oxygen-rich functional groups, as shown by FTIR, Figure 11), and defects in the structure (as shown by Raman spectroscopy, Figure 10B). Moreover, this value implies the negatively charged CQDs are repelling each other, maintaining the suspension stability.

5.1.4. Ultraviolet-Visible spectroscopy

UV-Vis spectra show two absorption bands at 265 and 360 nm (Figure 13). Absorption bands between 280 and 400 nm are often observed for carbon nanomaterials (Dong et al., 2014), (Huang et al., 2017), (Kasinathan et al., 2022). In the highest energy region, around 265 nm, electron transitions occur from the π molecular orbitals of the HOMO to the π* molecular orbitals of the LUMO, which are transitions characteristic of sp^2 carbon from aromatic structures (C=C). Furthermore, at the lowest energy region, with intense absorption near 360 nm, electronic transitions arise from non-bonding orbitals to antibonding π orbitals (n-π*). Those transitions are common for the C=O bonds, allowing us to infer the presence of oxygen heteroatoms in the CQD structure. The CQDs dispersion was light brown under visible light yet emitted light yellow greenish under UV irradiation (365 nm) (inset of Figure 13).

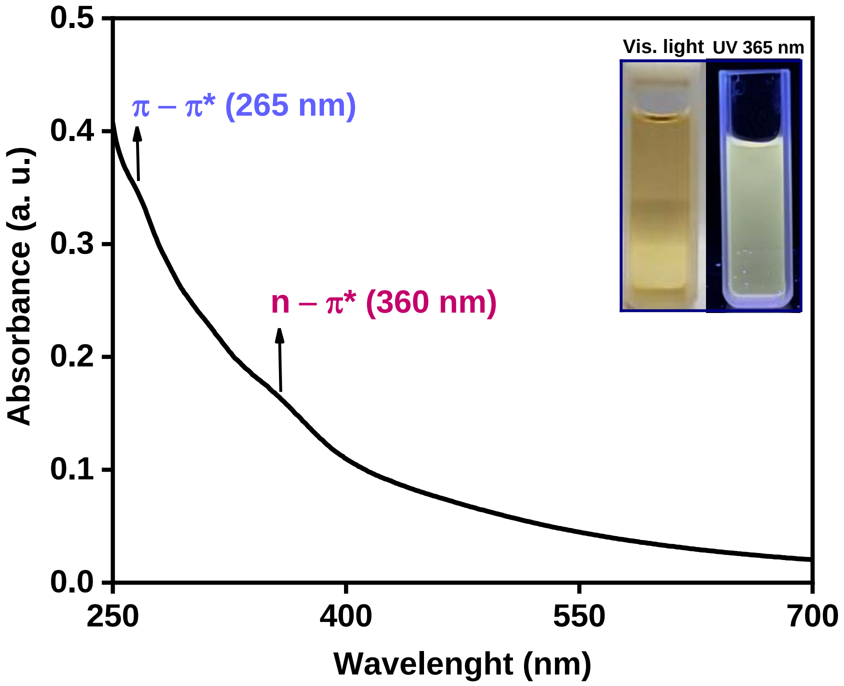

Figure 13. UV-Vis absorption spectra of the carbon quantum dot suspension in water. Inset: photographs of the CQDs suspension under visible light and 365 nm UV light. The π- π* absorption band arises from band-to-band transitions of the sp^2 carbon. The n-π* band is associated with the sub-band states originating from COOH and C=O edge groups.

Source: own author.

5.1.4.1. Tauc plot and Urbach tail

An important feature of semiconductors is the energetic difference between the valence band and conduction band, the bandgap. The bandgap value, expressed in electron volt (eV), is the amount of energy required to excite electrons from the ground state to the excited state; thereby, the bandgap value can directly affect the optical and electronic properties of the material.

Using the UV-Vis data, we can apply the Tauc method to obtain the bandgap value. The method was developed to investigate non-direct interband transitions of metallic amorphous semiconductors (Tauc, 1974). Since then, the Tauc plot has been used to obtain the bandgap value of different types of semiconductors. (Sharma et al., 2017), (Schneider, 2020); including carbon nanomaterials (H. Li et al., 2012), (Zhong et al., 2020), (Migliorini et al., 2022).

Figure 14 shows different regions of the Tauc plot. The first region, with photon energy between 1.5 and 3.5 eV, corresponding to the range 700 – 350 nm, is denominated as the weak absorption tail (WAT) region. In the WAT region, transitions occur from the tail states located above the valence band to tail states that are below the conduction band (Sharma et al., 2017). Weak absorptions in regions between 350 and 500 nm are often observed for carbon nanomaterials (Strauss et al., 2015), (L. Gao et al., 2021), (Q. Zhang et al., 2022), which can be associated with n-π^* transitions from heteroatoms in the structure (F. Wu et al., 2018).

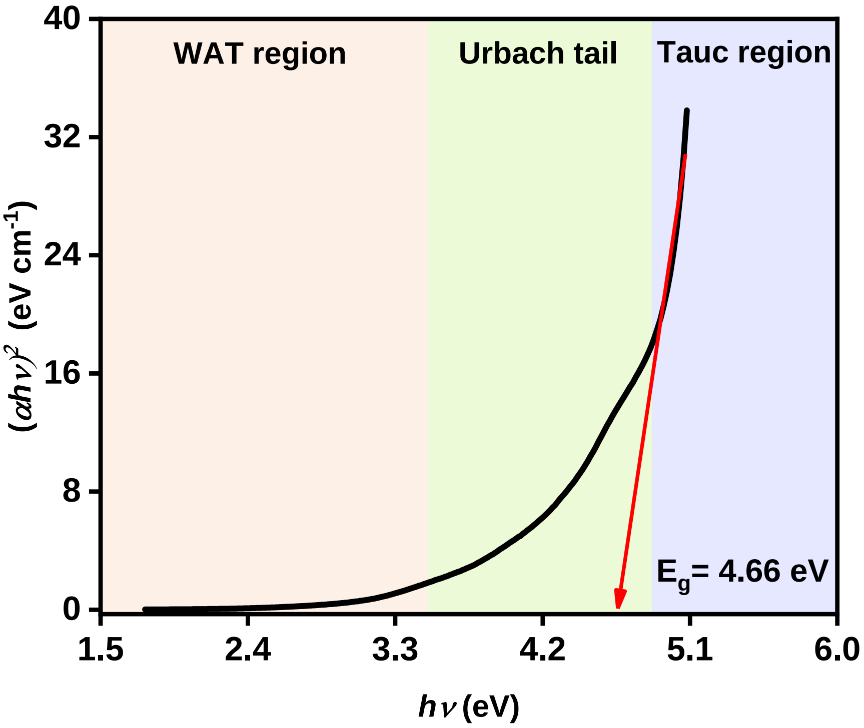

Figure 14. Tauc plot obtained from UV-Vis data showing the dependence of $(\alpha h\nu)^2$ on the $(h\nu)$, by which we can determine the bandgap value (E_g).
Source: own author.

In the second region, we observe the Urbach tail, covering the energy range between 3.5 and 4.8 eV (350 – 260 nm). The Urbach tail follows the relation of Equation 4:

$$\alpha(E) \propto \exp\left(\frac{E-E_g}{E_U}\right) \qquad \text{Equation 4}$$

Where E_U is the Urbach parameter, related to the width of the absorption edge (Klein et al., 2023). The origin of the Urbach tail is still a matter of debate, found in almost all semiconductors. Some of the possible factors for its existence are associated with phonons, impurities, or excitons (Urbach, 1953), (Klein et al., 2023). To metallic semiconductors, Zanatta (2019) attributes the onset of absorption to defective states that can cause such band tails. The defects have either been inserted, in the case of doped semiconductors or maybe a property of the material (Zanatta, 2019), (Klein et al., 2023). For nanomaterials synthesized from lignocellulosic residue, the tail in the band can be associated both with surface defects, introduced in the CQDs synthesis steps, and with heteroatoms present in the structure, which produces “false doping.”

The third region, the Tauc region, begins at 4.8 eV where the maximum point of $(\alpha h\nu)^2$ occurs at a photon energy of 5.1 eV. From this region, the bandgap of the CQD was estimated to be 4.66 eV (266 nm), which correlates to the absorption band from UV-Vis measurement of CQDs dispersed in water with maximum wavelength (λ_{max} = 265 nm). This bandgap value is like the ones found in the literature (Table 4).

Table 4. Comparison of bandgap value of carbon nanomaterials from lignocellulosic biomass. All bandgaps were obtained by the Tauc plot method.

Carbon nanomaterials	**Bandgap (eV)**	**Size (nm)**	**Reference**
Graphene quantum dots from spent tea	5.12	17.6	(Abbas et al., 2020)
Carbon dots from date seeds	5.58	5.08	(Aldakhil, 2024)
Carbon dots from bagasse	2.66	-	(Q. Chen et al., 2020)
Carbon dots from poplar wood chips	5.58	3.8	(Q. Gao et al., 2023)
Carbon dots from *Citrus medica* fruit extract	3.50	6.5	(Ninan et al., 2024)
Graphene quantum dots from spent tea leaves	5.45	2.3	(Abbas et al., 2023)
Carbon dots from banana peels	3.53	8.3	(Patel et al., 2024)
Carbon quantum dots from sugarcane biomass	4.66	-	This work

Source: own author.

5.1.5. Fluorescence properties

Concerning fluorescent carbon nanomaterials, fluorescence emission commonly depends on the excitation wavelength (WL_{EX}). Figure 15A shows this feature. Varying the WL_{EX} from 410 to 510, the emission intensity increases up to maximum emission ($E_{max.}$) at 526 nm with a WL_{EX} of 470 nm. Considering the results obtained from FTIR, that the surface of the CQDs is decorated with various functional groups, which favors the origination of different surface defects, the result also shown by Raman spectroscopy, these are likely the source of multiple light emission centers within the structure of CQDs (Zhu et al., 2020).

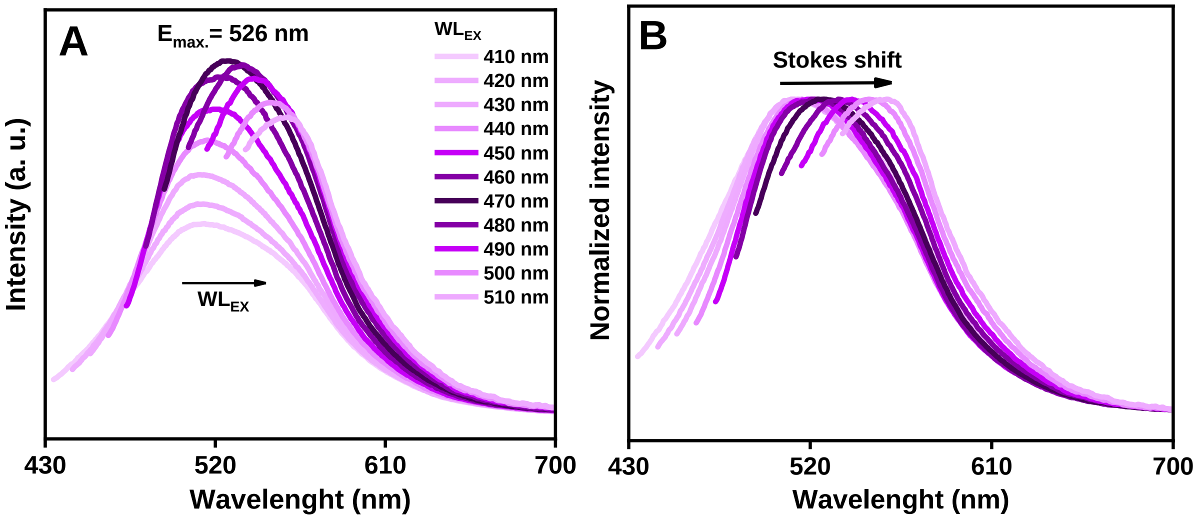

Figure 15. (A) The emission spectrum shows the dependence on the excitation wavelength. Excitation wavelength varied from 410 to 510 nm, and the maximum emission intensity was observed at 526 nm upon excitation at 470 nm. The arrow indicates the increase in excitation wavelength. In (B) is shown the normalized emission intensity; Stokes shift highlights the redshift i. e. longer wavelengths and lower energy emissions.

Source: own author.

While the intensity of emissions has varied, we can also see a shift to the red region (bathochromic shift) (Stokes shift, Figure 15B) i.e., emissions at longer wavelengths and lower energies. The red shift phenomenon can be assigned to the high polydispersity property of the suspended CQDs solution, as identified by the high polydispersity index (0.458); such characteristics offer diverse optical properties on the nanoscale (Fang et al., 2024). Moreover, the recombination of electron-hole pairs in the localized π and π* electronic levels of the sp^2 sites can also explain the fluorescence; in such a manner, sp^2 sites remain within the σ and σ* states of the sp^3 structure, thus, resulting in weak absorption around UV-Vis region but high emissions in the visible region (Ding et al., 2020). Huang et al. (2017) linked the mechanism for excitation-dependent fluorescence emission to the size distribution and emissive traps onto the surface of carbon dots obtained from sugarcane molasses. A similar result was found by

Xue et al. (2016), whose carbon dots from peanut shells presented green fluorescence and emissions shifted to a red region upon the increase of excitation wavelength.

In an alternative way, we can visualize the fluorescence emission using a laser pointer of different excitation wavelengths (Figure 16). By irradiating the suspension with a blue laser, we can observe the redshift, emitting around the green region. Furthermore, when irradiated with a green laser, the suspension emits light around the yellow/orange region. However, when irradiated with red light, the suspension only scatters it, revealing that does not absorb light with longer wavelengths.

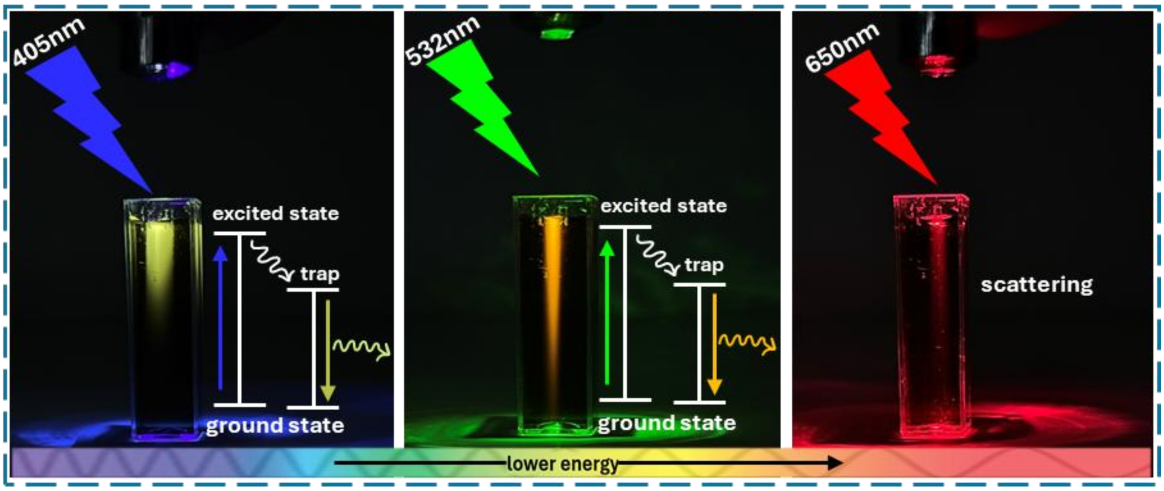

Figure 16. Mechanism for fluorescence emission induced by laser pointer. Excitation in certain wavelengths leads to emission at longer wavelengths, that is, the redshift. This mechanism attributes the phenomenon to the presence of traps in the CQDs structure due to surface defects and functional groups.
Source: own author.

As observed by fluorescence spectroscopy and laser pointer-induced fluorescence, a red shift phenomenon is occurring in emissions. This feature is a matter of debate in the scientific community. Reports attributed the redshift to quantum size effects (Bao et al., 2015), (Jiang et al., 2015), to a high degree of graphitization structure and a large amount of surface functional groups (Wei et al., 2020), and to surface states (carboxyl contents, oxidation degree) (Ding et al., 2020). Functional groups and surface defects can introduce trap states in the band gap, in which case the photoexcited exciton can be trapped and the recombination of the electron-hole pair leads to the emission of photons with lower energy (longer wavelengths) (Tang et al., 2012), (Cayuela et al., 2016).

Herewith, we do not attribute the red shift of fluorescence to one feature, such as conjugated π-domains, surface defects, or size effects. But, considering the FTIR results, showing several oxygen-containing functional groups, which are created by surface oxidation, a conclusion also sustained through Raman results, we conclude that a mechanism for this phenomenon should be associated mainly with surface-state-related fluorescence.

5.2. Photoelectrochemical properties of carbon quantum dots suspension

Although our study aimed to evaluate the use of CQDs immobilized onto ITO electrodes to further photoelectrocatalytic applications, we also investigated the effect of pH and concentration of CQDs suspension as electrolytes. Besides, altering the suspension pH can provide insights concerning the CQD surface charge. As shown in Figure 17A, the concentration varied from 68.1 µg mL^{-1} to 1,430 µg mL^{-1} (pure CQDs suspension). The more concentrated CQDs in the electrolyte, the more current from CQD oxidation is observed; photocurrent is also enhanced due to the photoelectrochemical process.

The influence of CQDs suspension pH in the photocurrent response, presented in Figure 17B, reveals the lowering of oxidation charge transfer at acidic and basic pHs. The lowest photocurrent seemed for pH 2, followed by an increase for pH 4, further increasing for pH 7 and 10, which do not change significantly, and finally, a decrease for pH 12.

Although we do not know the exact mechanism behind this lower photocurrent for acidic and basic pHs, some explanations have been described based on changes in energy level, protonation and deprotonation of functional groups, and nanoparticle agglomeration (Ehtesabi et al., 2020). In particular, the protonation and deprotonation of carboxylic and phenolic groups on the surface of CQDs can affect the HOMO and/or LUMO positions (Song et al., 2014); therefore, a shifting of the Fermi level, which may be affecting the type of electronic transitions within the CQDs (Dutta Choudhury et al., 2017). Furthermost, low pH, with the carboxylic and phenolic groups protonated, could be causing an effect of positive gate, that depletes hole carriers, thereby decreasing the conductance (Jia et al., 2012).

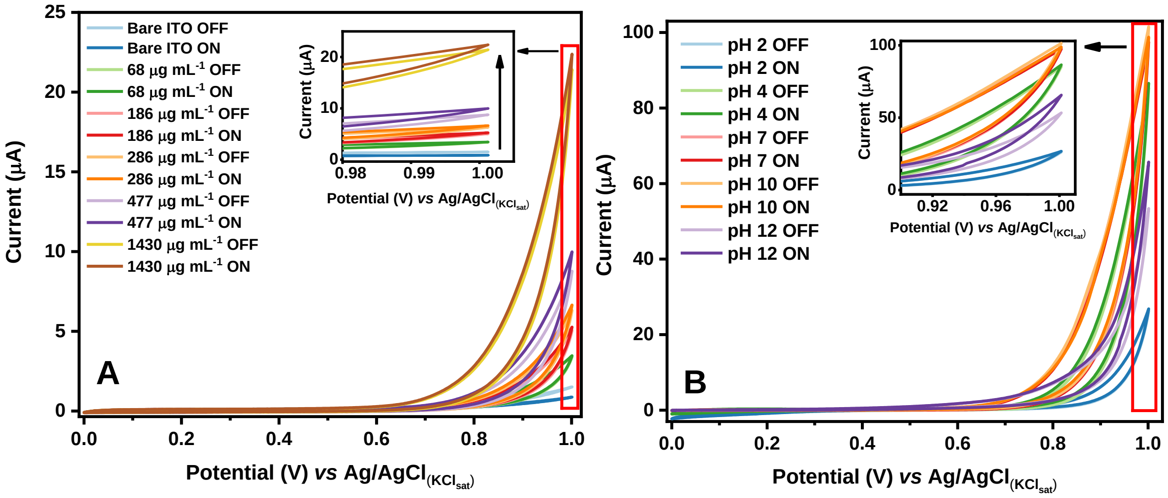

Figure 17. Cyclic voltammograms (0.0 to 1.0 V, scan rate: 10 mV s^{-1}) showing the concentration effect of CQDs in the electrolyte (H_2SO_4, HNO_3, KOH, pH = 7.0) (A) and the influence of CQDs electrolyte pH (B). OFF: analysis in dark. ON: analysis under blue light irradiation (405 nm). ITO was used as the working electrode, Ag/AgCl (3 M KCl) as the reference electrode, and Pt as the counter electrode.

Source: own author.

5.3. Carbon quantum dots-decorated electrodes

5.3.1. Surface characterization of working electrodes

LbL assembly is a versatile technique for nanoscale film preparation. Diverse materials can be assembled onto various surfaces through sequential adsorption of opposite charge molecules. LbL technique was used to immobilize CQDs onto the ITO electrode. Further, we assembled NiTSPc under and on top of the CQDs film to investigate the mechanism of electron transfer and argue if the assembly could result in a more efficient transfer of photoinduced excitons. The films were investigated through Raman spectroscopy and SEM techniques. Figure 18 shows digital images of the working electrodes produced by LbL deposition. For CQD electrodes the color increased accordingly with the number of bilayers, indicating the mounting augment in visible light absorption.

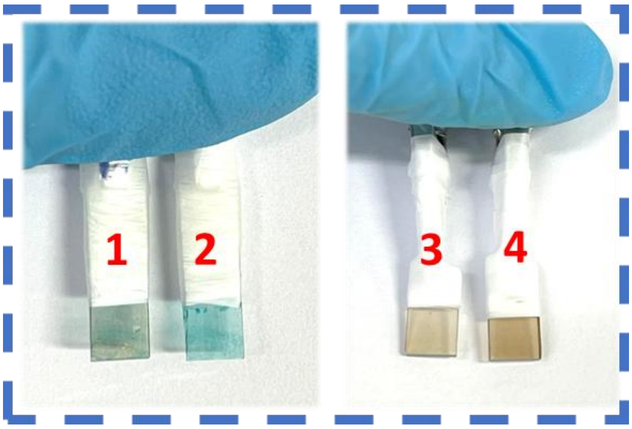

Figure 18. Digital images of working electrodes. 1: ITO/NiTSPc$_{15}$/CQD$_{15}$, 2: ITO/CQD$_{15}$/NiTSPc$_{15}$, 3: ITO/CQD$_{15}$, and 4: ITO/CQD$_{30}$.

Source: own author.

The interaction between NiTSPc and PAH layer occurs *via* NH_3^+—SO_3^- salt-bridges (Alencar et al., 2007), (Alencar et al., 2009), (Furini et al., 2020), and for other metal-ligand phthalocyanines, like iron(III) phthalocyanine tetrasulfonic acid (Fe-TSPc) (Koo et al., 2012) and cobalt(II) tetrasulfonated phthalocyanine (CoTSPc) (De Sousa Luz et al., 2011). Figure 19 shows the schematic representation of this type of interaction.

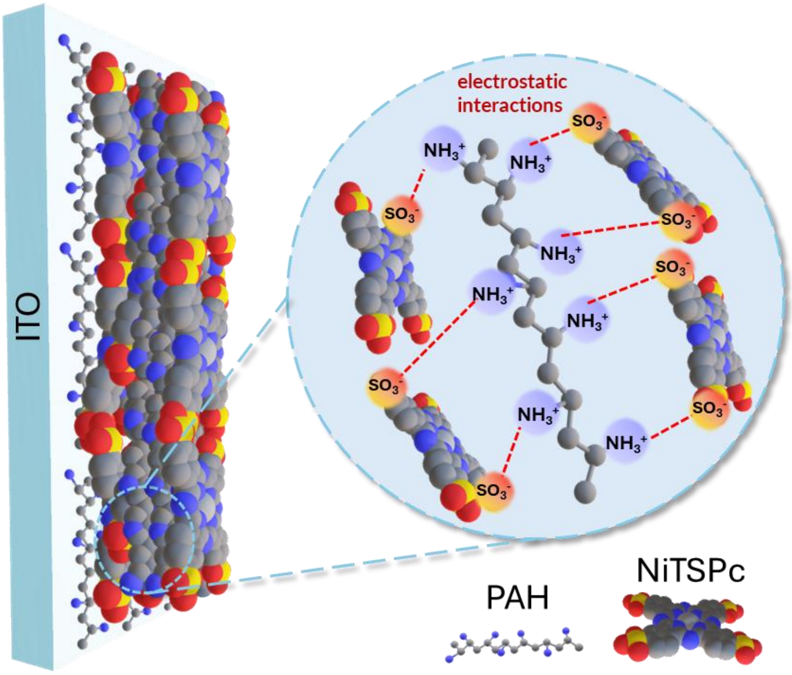

Figure 19. Schematic representation of electrostatic interactions between PAH and NiTSPc in the formation of bilayers onto ITO substrate.

Source: own author.

Furthermore, the interactions between CQDs and PAH could be governed by those electrostatic interactions. Let us recall that the zeta potential of neutral CQDs suspension is -22.6 mV and PAH zeta potential at pH 3.5 is up to +40.0 mV (Paltrinieri et al., 2017), so the assumption of electrostatic interaction is consistent regarding these aspects. Figure 20 shows the schematic representation of the interactions between surface negative functional groups of CQDs and protonated amino groups of PAH molecule. LbL assembly of carbon nanostructures onto electrodes is demonstrating several promising results for the application of photoelectrocatalysis. Zeng et al. (2016) performed the assembly of GQDs onto positively charged zinc oxide nanowires (ZnO NW), which were previously deposited onto FTO glass. They used the electrode as a photoanode for photoelectrochemical hydrogen generation; this report was the first published demonstrating this reaction. Other studies have shown the assembly of crystalline silicon solar cells with nitrogen-doped CQDs owning highly electronegative functional groups (Ali et al., 2020). In this regard, the LbL technique is a promising way to perform the immobilization of CQDs onto ITO for photoelectrochemical purposes.

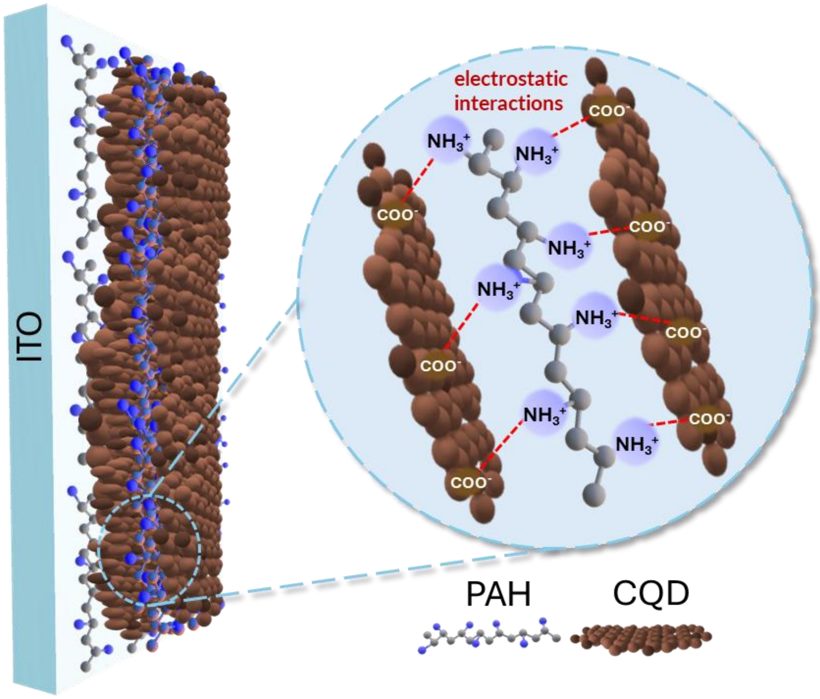

Figure 20. Schematic representation of electrostatic interactions between PAH and CDQs in the formation of bilayers onto ITO substrate. The oxygen-containing functional groups are represented by the carboxyl group.
Source: own author.

Figure 21 displays the Raman spectra of the working electrodes and NiTSPc structure for comparison. Two known bands are observed in the spectrum (a) and (b), which are ITO/CQD$_{15}$ and ITO/CQD$_{30}$ electrodes, respectively; the D band around 1320 cm^{-1} associated with sp^3 carbons from defects, and the G band around 1590 cm^{-1} related to sp^2 carbon atoms. Furthermore, the D band is overlapped by the pyrrole stretching band from the phthalocyanine around 1332 cm^{-1}. Moreover, D and G bands increase from spectra (a) to (b), clearly related to the amount of CQDs onto the electrode, considering they have 15 and 30 bilayers of CQDs, respectively. For the electrode with 15 CQDs above 15 bilayers of NiTSPc (Figure 21c), we may note few bands of NiTSPc structure appear because covered phthalocyanine hinders the light scattering, decreasing the signal response.

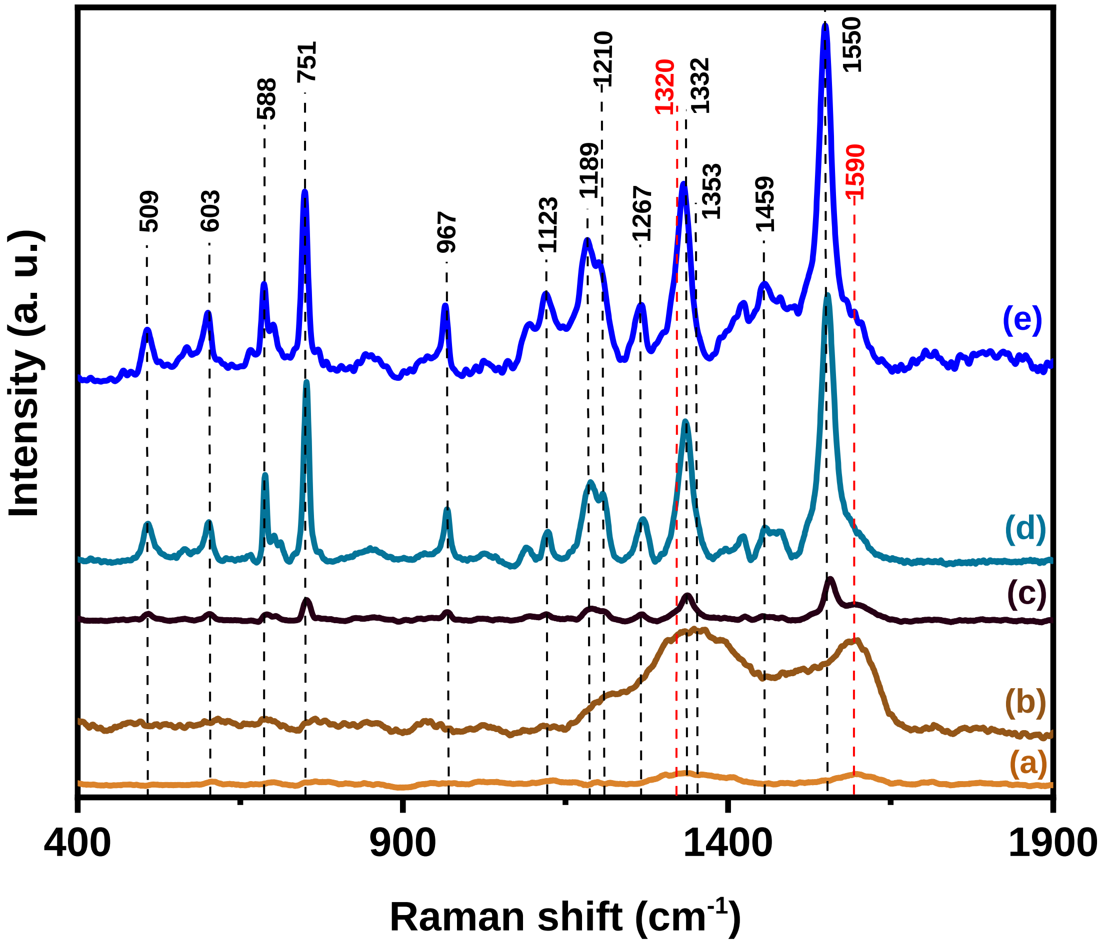

Figure 21. Raman spectra for (a) ITO/CQD$_{15}$, (b) ITO/CQD$_{30}$, (c) ITO/NiTSPc$_{15}$/CQD$_{15}$, (d) ITO/CQD$_{15}$/NiTSPc$_{15}$, and (e) ITO/NiTSPc. Wavenumbers in red are from CQDs.

Source: own author.

For (d), the electrode with 15 bilayers of NiTSPc above 15 bilayers of CQDs, we can observe the major band intensity is related to the phthalocyanine structure, which was already expected since the above layers are responsible for the light scattering. These results demonstrate the successful immobilization of CQDs and NiTSPc onto ITO glass. Table 5 summarizes the assignments of the Raman bands.

Table 5. Summarization of Raman shifts and respective assignments.

Raman shift (cm^{-1})	Assignments[‡]
509	Isoindole deformation
603	Macrocycle vibration
688	Macrocycle vibration
751	Macrocycle vibration out-of-plane bending
967	Benzene breathing
1123	C-H bending
1189	SO_3 stretching
1210	SO_3—NH_3 stretching
1267	C-H bending
1320	D band of CQDs
1332	Pyrrole stretching overlapping with CQDs D band.
1353	PAH C-H deformation
1459	Isoindole stretching
1550	C=C, C=N pyrrole stretching
1590	G band of CQDs

[‡] From references (Zucolotto et al., 2003), (Furini et al., 2020), (Martin et al., 2023).

SEM images, Figure 22, show the surface morphology of ITO and working electrodes. The bare ITO presents a homogeneous phase and seems to have high roughness, which is, in fact, due to the indium tin oxide deposited onto glass (Figure 22a and b) (Hemasiri et al., 2017). One can observe from Figure 22c that the NiTSPc films onto CQDs have reduced porosity and sites compared to the ones where CQD films were deposited above the phthalocyanine (Figures 22e and f). Indeed, in the latter, we can observe the larger sites and conglomerate of CQD particles. Despite that, CQDs with 15 bilayers onto ITO (Figure 22g and h) presented minor sites and lower evidence of conglomerates.

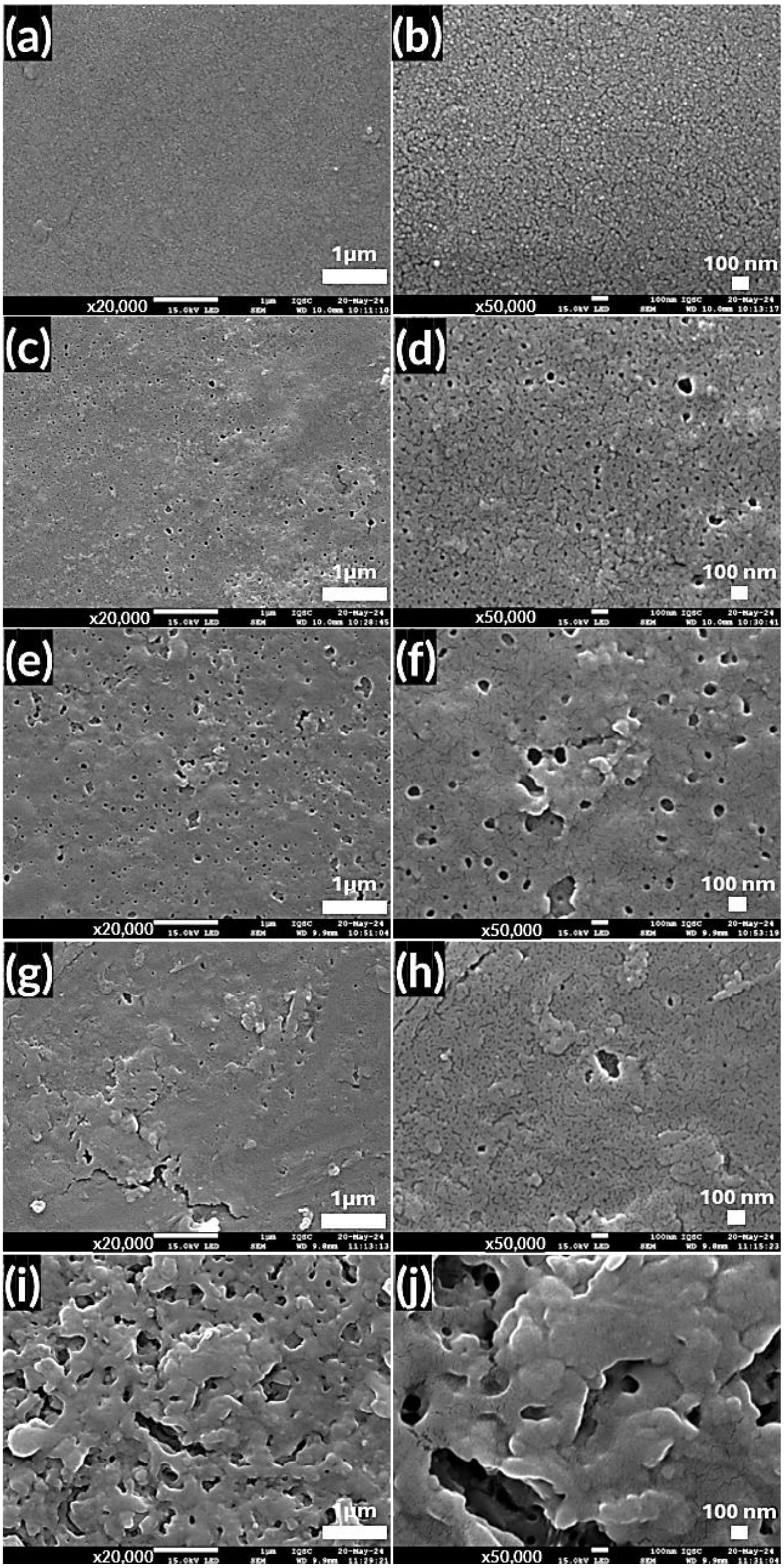

Figure 22. SEM images of (a) and (b) ITO, (c) and (d) ITO/CQD$_{15}$/NiTSPc$_{15}$, (e) and (f) ITO/NiTSPc$_{15}$/CQD$_{15}$, (g) and (h) ITO/CQD$_{15}$, (i) and (j) ITO/CQD30. Left and right have 20,000 and 50,000 magnifications, respectively.

Source: own author.

Furthermore, Figures 22i and 22j are the electrode surfaces with 30 bilayers of CQDs; the formation of conglomerates of particles is observed. We can speculate that the film does not form homogeneously, but after the first layer above the PAH, it starts to grow randomly. This behavior could occur due to the adherence of particles governed by weak forces, such as van der Waals forces. This network is indicative of CQDs with high surface energies, leading to conglomerates mutually linked through dispersive forces (Oza et al., 2016). Similar images are obtained by those particles agglomeration, such as for black carbon (Patey et al., 2009). Sohn et al. (2016) also presented a similar one with silicon (Si) nanoparticles covered with carbon. Furthermore, the nanoparticles were coated onto copper foil to use as an anode material for lithium-ion batteries; the porous carbon matrix is responsible for excellent electronic transport in their system.

5.3.2. Photoelectrochemical performance of carbon quantum dots electrodes

The photoelectric response of CQDs and CQDs/NiTSPc electrodes was investigated by CV from 0.2 to 1.2 V with a 10 mV s^{-1} scan rate and chronoamperometry with an externally applied bias of 1.0 V for 220 s. All experiments were carried out in the homemade photoelectrochemical system using HCl pH = 1.0 and carbonate/bicarbonate buffer pH = 9.6. Ag/AgCl (3M KCl) was used as the reference electrode and Pt as the counter electrode. Moreover, the analyses were performed in dark and under UV (365 nm) and blue (405 nm) light irradiation.

For the sake of clarity, from now on the electrode $ITO/CQD_{15}/NiTSPc_{15}$ will be denoted as CQD/NiTSPc; electrode $ITO/NiTSPc_{15}/CQD_{15}$ will be denoted as NiTSPc/CQD; and electrodes ITO/CQD_{15} and ITO/CQD_{30} will be denoted as CQD15 and CQD30, respectively.

NiTSPc/CQD surfaces showed evident photocurrent at anodic potentials when performed in HCl compared to the background current density in the dark (Figure 23A). The film showed one electrochemical process assigned to Ni^{2+}/Ni^{3+} pair through the process: $[NiTSPc(II)]^{4-} \rightleftharpoons [NiTSPc(III)]^{3-} + e^{-}$ (Alencar et al., 2009). Half wave potentials ($E_{1/2}$) were 0.84, 0.86, and 0.88 V under dark, blue, and UV light, respectively. One can observe that the increase in anodic photocurrent density followed by a shift of $E_{1/2}$ is correlated with short wavelength incidence, that is, higher energetic photons. One can also see that more energetic photons lead to higher photocurrent; this result could be a consequence of more electron-hole pairs being generated by UV than by blue light. The photogenerated electrons are transferred to NiTSPc as required by increasing the oxidation potential.

When we have a CQD/NiTSPc surface, the phthalocyanine is no longer in direct contact with ITO, this hinders the metal center process from occurring. A reasonable explanation for that can be derived considering the absorption spectra of NiTSPc which shows poorly absorption in the violet and blue region (~400 nm) (Kolay et al., 2020); by that, the excitation of electrons is hindered when the molecule is excited in this wavelength region. Consequently, electron transfer from NiTSPc to CQDs and the oxidation of some species in electrolytes to the reduction of NiTSPc are impaired under blue light irradiation.

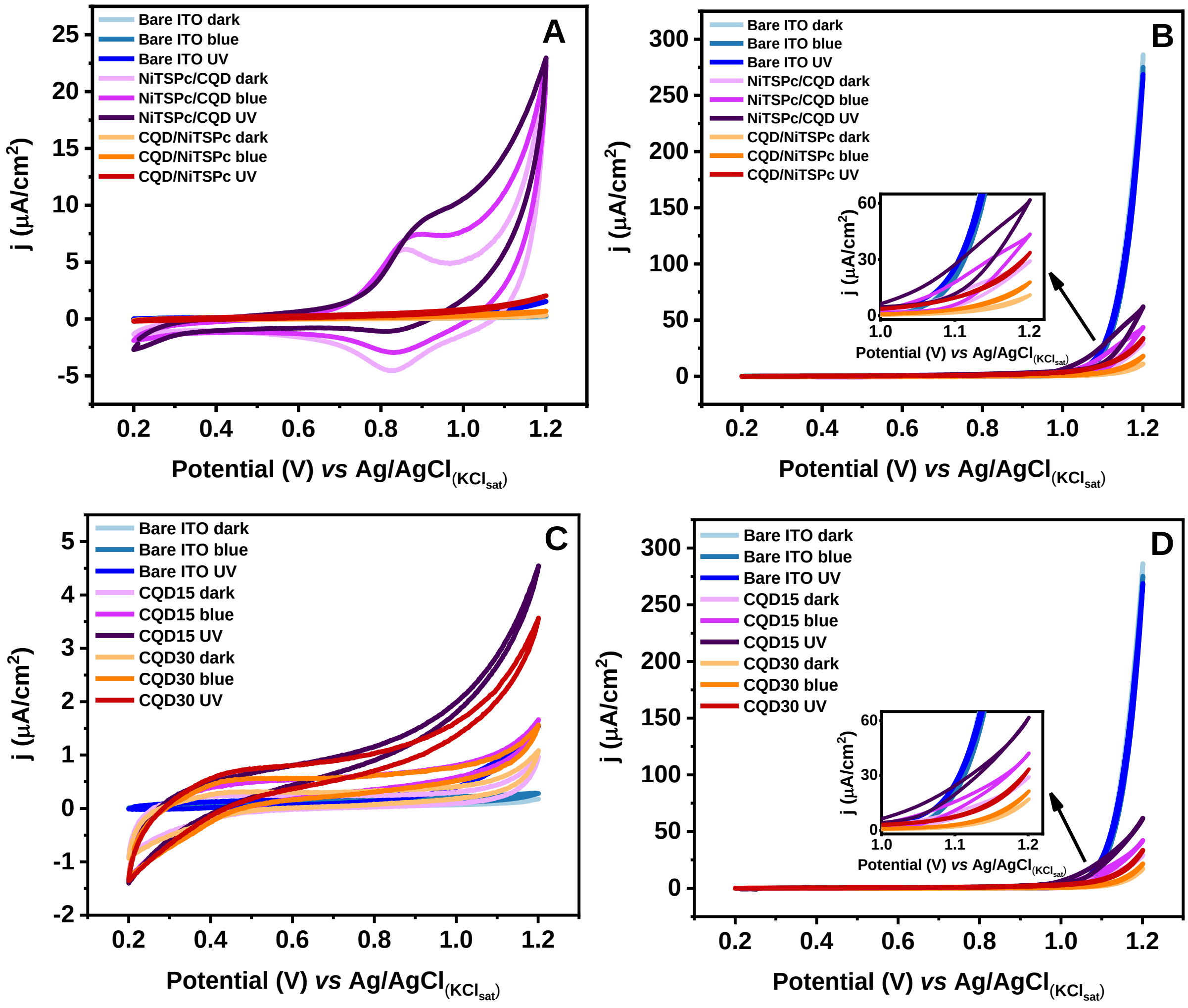

Figure 23. CVs of LbL assembled electrodes with NiTSPc and/or CQDs. (A) Analysis in HCl pH = 1.0. (B) analysis in carbonate/bicarbonate buffer pH = 9.6. (C) analysis under HCl pH = 1.0. (D) analysis in carbonate/bicarbonate buffer pH = 9.6. Note: A and B are CVs with electrodes with CQDs and NiTSPc; C and D are electrodes only with CQDs, differing in the number of bilayers.

Source: own author.

One can surmise that, for the NiTSPc/CQD surface, at anodic potentials the Fermi level is diminished, which causes the oxidation of NiTSPc molecules and, consequently, CQD is oxidized for the reduction of NiTSPc and closes the circuit for electron transfer to occur. Likewise, under blue and UV light these process presents more current flowing through the circuit, indicating that the incident photons excite the electrons from the valence band to the conduction band enhancing electron-hole separation on CQD, then providing photoexcited electrons to the NiTSPc reduction. One should notice when the electron is transferred from CQDs to NiTSPc the holes in CQDs will be consumed by the oxidation of one species A in the electrolyte [$A + h^+ \rightarrow A^+$]. The formation of A^+ from A using CQD as photocatalysts under blue and UV light generates the photocurrent. Therefore, for promising photoelectrocatalytic applications the NiTSPc/CQD assembly should be considered. A similar result was found by Messina et al. (2021), where they performed a combination of CQDs and GQDs with TiO_2 nanoparticles and evaluated the photocurrent response under UV (365 nm) and visible light (455 nm). The photocurrent density has doubled under UV light, whereas under visible light showed a slight increase. These results can be clearly correlated with the ones obtained here. In Figure 24 is summarized the current density at 1 V vs Ag/AgCl in pH = 1.

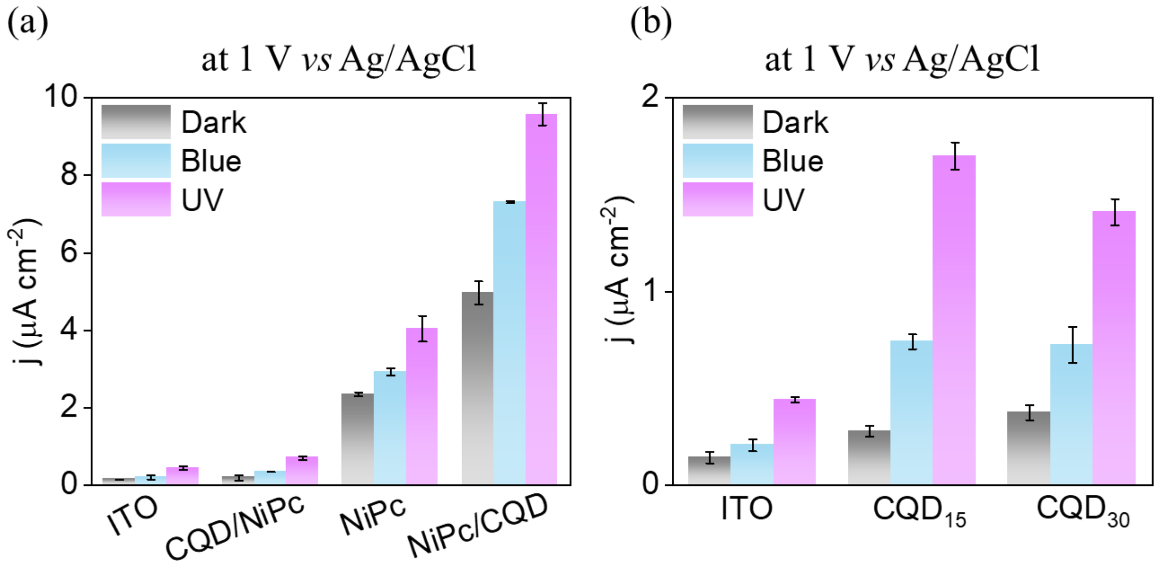

Figure 24. The maximum current density at 1 V vs Ag/AgCl for (a) electrodes with NiTSPc and (b) electrodes with CQDs.

By using pH 9.6, NiTSPc/CQD did not show any redox process related to the phthalocyanine (Figure 23B). Although the reason for this is not understood yet, one should note, disregarding bare ITO, the anodic photocurrent density under UV reached up to 60 µA

cm^2 at 1.2 V, in contrast to 23 µA cm^2 obtained for the same surface at pH = 1.0, also under UV. The reason of the significant increase in photocurrent density in basic medium is not clear yet; could be due to acidic environments containing high concentrations of H^+ leading to the solution protonation hence influencing the efficiency of the electron donor (S. Xu et al., 2024), also due to the difference in ionic strength of the electrolyte, or influenced by some other cofactor, which is also a matter of concern for other authors (H. Y. Wang et al., 2021). A similar result was observed for CQD_{15} and CQD_{30} surfaces in pH 1.0 and 9.6 (Figure 23C and D). However, two main aspects can be considered. First, in HCl the current of CQD_{15} and CQD_{30} at dark was higher compared to the bare ITO, suggesting that the CQDs enhanced the surface conductivity; moreover, photocurrents also increased compared to bare ITO implying the photoelectrocatalytic property of CQDs.

In basic conditions, bare ITO showed a pronounced effect at 1.2 V over the CQDs electrodes, even when these have been irradiated. Yet, the same observation can be made here. As in pH 1.0, analyses under pH 9.6 and irradiation showed higher photocurrent than those performed in the dark. Nevertheless, at a lower applied bias of 1.0 V using chronoamperometry, all surfaces showed significant photoelectrocatalytic activity toward acidic and basic conditions (Figure 25). Tan's group reported an alike result to GQDs. Under visible light irradiation, both GQDs and ZnO NW were photoexcited generating excitons. The holes in the valance band of ZnO are transferred to the HOMO orbital of GQDs and therefore oxidize water to oxygen. At the same time, the electrons from LUMO of GQDs are transferred to the VB of ZnO and then to the external circuit for the reduction of water to hydrogen on the counter electrode (Zeng et al., 2016).

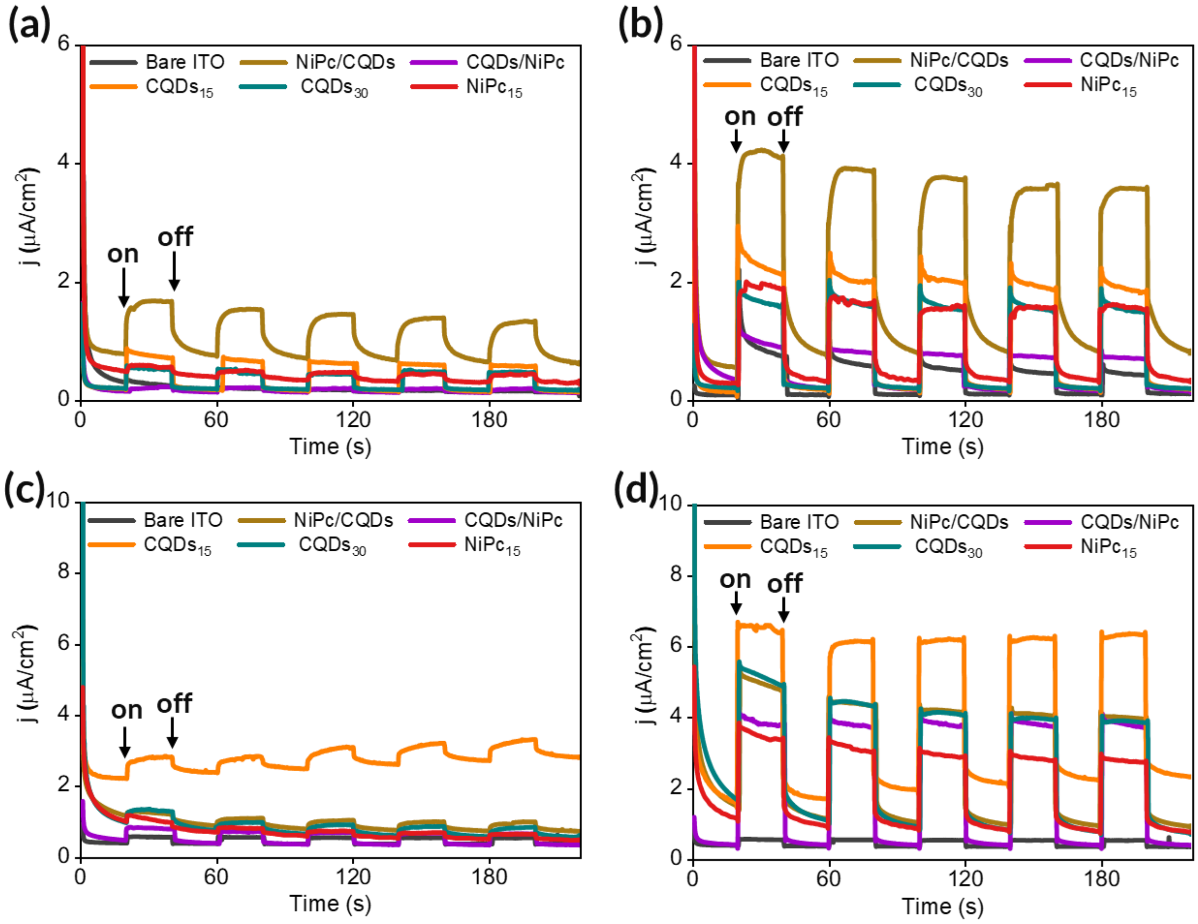

Figure 25. Chronoamperometry profiles of LbL assembled electrodes with NiTSPc and/or CQDs with the applied bias of 1.0 V. A: Analysis in HCl pH = 1.0 and blue light. B: Analysis in HCl pH = 1.0 and UV light. C: analysis in carbonate/bicarbonate buffer pH = 9.6 and blue light. D: analysis in carbonate/bicarbonate buffer pH = 9.6 and UV light. Note: The legend concerns all experimental data. “ON” and “OFF” means turning ON and turning OFF the light source. The net increase in current density for all experiments is compared to the photocurrent of the bare ITO.

Source: own author.

The photocurrent of the CQD_{15} surface, in acid and basic conditions, showed to be greater than the CQD_{30} surface at an applied bias of 1.0 V (Figure 25C and D). This result overturned the hypothesis that more CQDs on the surface would improve the photocurrent due to more photoelectron generation. However, by doubling the number of bilayers of CQDs the photocurrent is diminished. A first thought relies on the generation of photoelectrons:

considering that more CQDs could generate more photoexcited electrons, these can be a hindrance to the flow of electrons. Another, and more presumed one, consists of the CQDs aggregation onto the surface. As evidenced by SEM analysis, the surface of CQD_{30} shows large, aggregated particles, revealing the unorganized CQD deposition. Therefore, the photoexcited electron-hole pairs could be recombining at the boundary of CQDs before reaching the ITO substrate, of course, leading to a decrease in photocurrent density (Shalom et al., 2012), (Bian et al., 2014). These results confirmed that CQDs from lignocellulosic biomass have direct photoelectrochemical response under UV and blue light irradiation. Thereupon, lignocellulosic residues, such as sugarcane biomass, are an excellent carbon source for facile synthesis of CQDs offering a destination for this residue and presenting an environment-friendly nanomaterial for photoelectrocatalytic applications.

Electrochemical impedance spectroscopy was carried out in HCl pH 1.0 at dark and under blue and UV irradiation with an applied bias of 0 V vs OCP. Figure 26 presents the Nyquist plots and equivalent circuits, and Table 6 presents the parameters from the fitting of the EIS spectra for working electrodes with CQDs. In the equivalent circuit (RS{Q1[R1(R2C2)]}), R, C, and Q are resistance, capacitance, and constant phase element (CPE), respectively. CPE is characteristic of porous or rough materials, used to represent a frequency-dependent capacitance (Ranganathan et al., 2016). The assembly of CQDs and NiPc onto the ITO results in a heterogeneous surface with non-uniform current distribution, by that, the capacitance of porous materials is represented by a CPE, dependent of Y_02 and n ($0 \leq n \leq 1$); for ideal capacitors $n = 1$. The capacitance values for Q1 and C2 increased for measurements under irradiation as seen in Table 6, which was expected since, at open circuit conditions, a charge accumulation arises at the electrode/electrolyte interface.

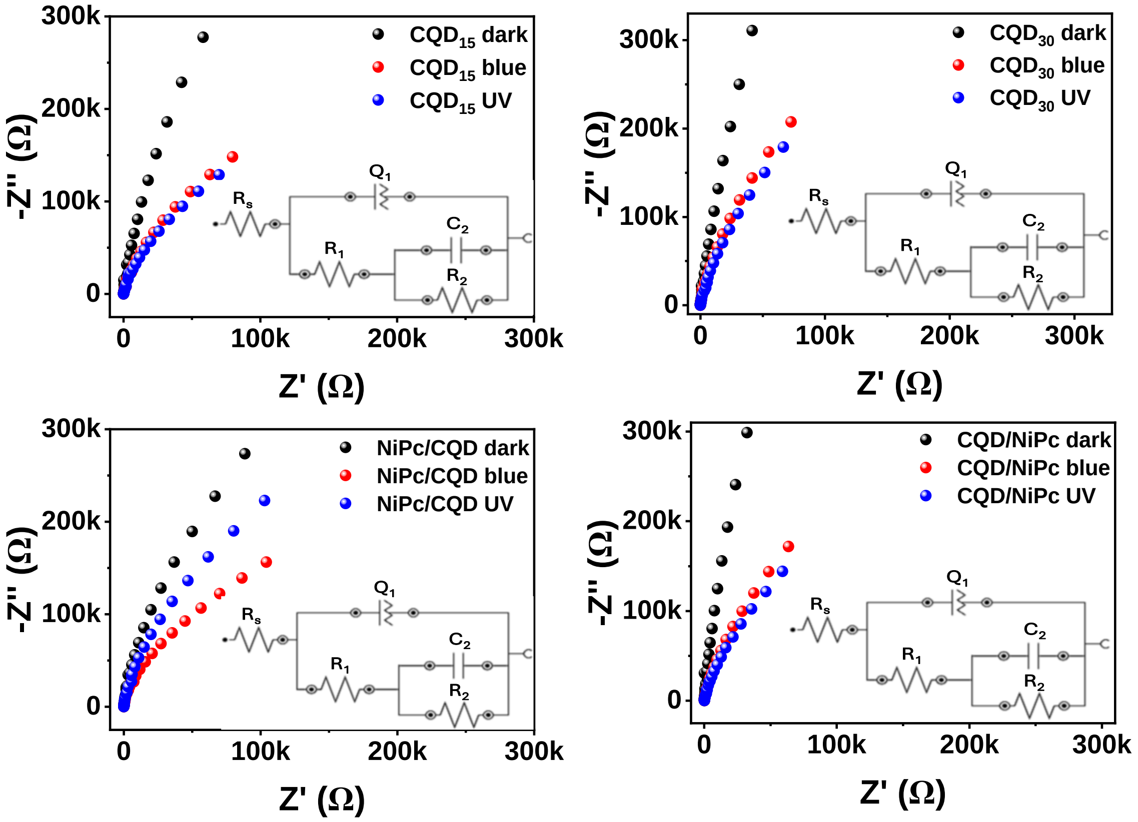

Figure 26. Nyquist plots for electrodes with CQDs at dark and under blue and UV irradiation. The EIS was performed in HCl pH = 1.0 (100 kHz to 0.1 Hz, 0 V vs OCP).

Source: own author.

Table 6. Fitting parameters were obtained from the Nyquist plots.

		Q$_1$				
Electrode	R$_s$ (Ω)	Y$_0$ (μF s^{n-1})	n	R$_1$ (kΩ)	R$_2$ (kΩ)	C$_2$ (μF)
CQD$_{15}$ dark	58.88	4.74	0.93	0.45	2860.00	0.42
CQD$_{15}$ blue	59.21	6.45	0.92	237.00	342.00	5.03
CQD$_{15}$ UV	58.72	7.56	0.92	204.00	275.00	5.78
CQD$_{30}$ dark	78.75	4.36	0.97	549.00	6560.00	0.65
CQD$_{30}$ blue	77.84	5.60	0.95	331.00	751.00	2.20
CQD$_{30}$ UV	77.52	6.16	0.94	228.00	612.00	2.58
NiTSPc/CQD dark	80.41	4.40	0.97	494.00	916.00	1.86
NiTSPc/CQD blue	79.91	4.30	0.97	150.00	308.00	5.42
NiTSPc/CQD UV	79.61	4.29	0.97	232.00	543.00	2.77
CQD/NiTSPc dark	75.94	3.86	0.95	0.04	7110.00	1.25
CQD/NiTSPc blue	72.73	4.57	0.83	0.01	882.00	3.07
CQD/NiTSPc UV	70.61	5.06	0.77	0.01	804.00	3.81

From the EIS performed in the dark, intrinsic electronic properties of the electrodes were investigated through the Mott−Schottky (M−S) plots (1 kHz). Figure 27 shows the M-S plots and Table 7 shows the flat band potentials (VFB) obtained from the extrapolation to the x-intercept.

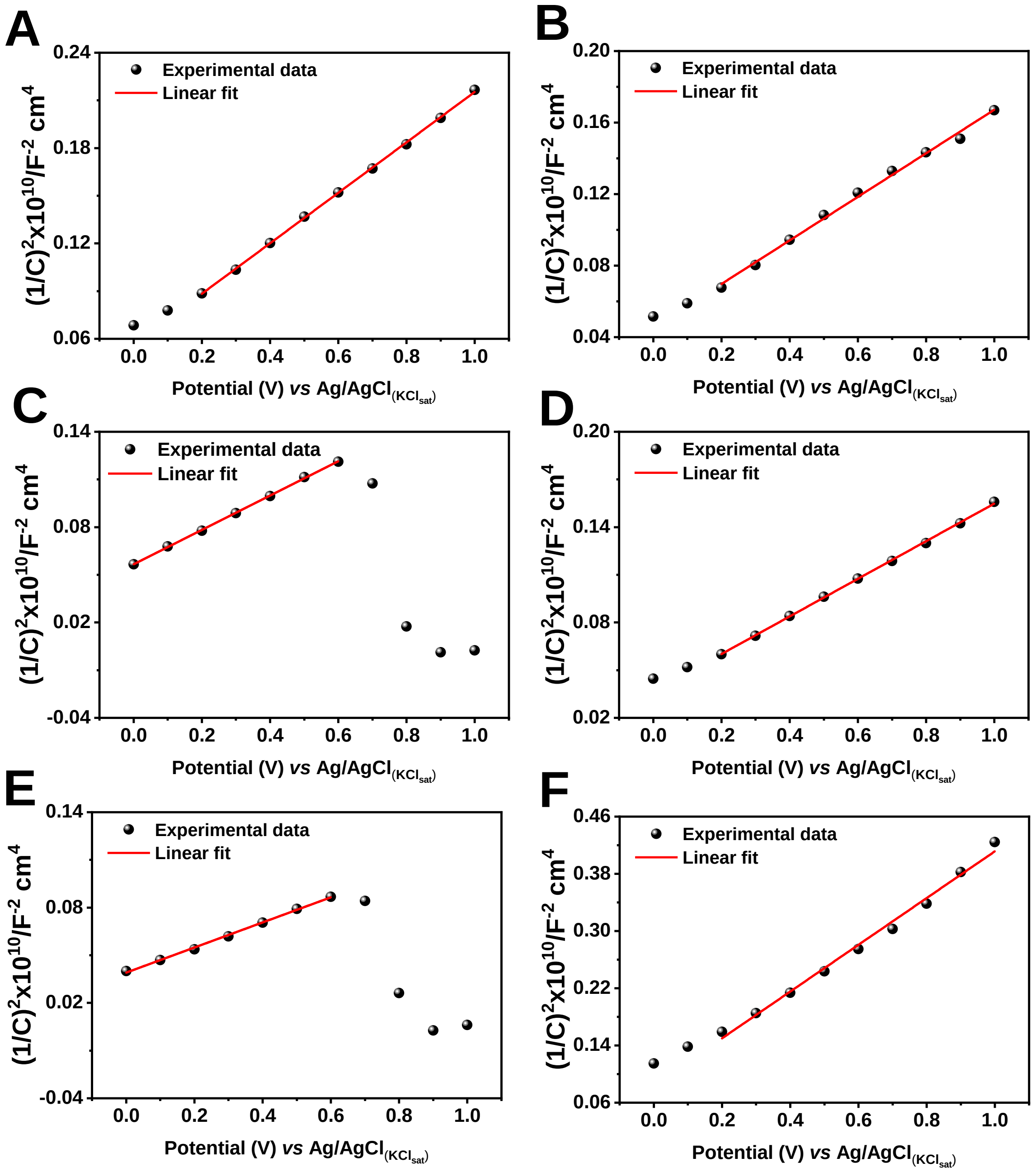

Figure 27. Mott-Schottky plots for each electrode. A: CQD_{15}. B: CQD_{30}. C: NiTSPc/CQD. D: CQD/NiTSPc. E: $NiTSPc_{15}$. F: Bare ITO.

Source: own author.

Also, the number of donors (ND) was calculated from Equation 5. All M-S plots present positive slopes, indicating that they are n-type semiconductors, with electrons as the majority carriers. Interestingly, electrodes NiTSPc/CQDs and NiTSPc_{15} show positive slopes at lower potentials (< 0.6 V) but negative ones at higher potentials; this behavior is a suggestion that a p-n interface was formed (H. Lim et al., 2017), (Malara et al., 2015).

$$slope = \frac{2}{\varepsilon\varepsilon_0 A^2 e N_D} \qquad \text{Equation 5}$$

where the slope is from the Mott-Schottky plot (Figure 26), ε is the dielectric constant of ITO (3.2), ε_0 is the permittivity of free space, A is electrode area, e is the electronic charge, and N_D is the number of donors (Gelderman et al., 2007).

Table 7.Flat band potential of the working electrodes.

Electrode	Flat band potential (V)	N_D
Bare ITO	-0.257	2.16E+31
CQD15	-0.356	4.11E+31
CQD30	-0.308	6.46E+31
NiPc/CQD	-0.493	8.26E+31
CQD/NiPc	-0.372	5.79E+31
NiPc15	-0.523	6.03E+31

The formation of a p-n interface induces an electric field within the space charge region leading to a higher hole accumulation at the electrode surface. This improvement in charge carrier collection could lead to improved photoelectrochemical water oxidation due to the higher number of holes available on the electrode surface (H. Lim et al., 2017). The FBP values of all electrodes were lower than the bare ITO, this negative shift strengthens the band bending at the electrode/electrolyte interface, and can also indicate a decrease in charge recombination and reduction of the overpotential for water oxidation (Kong et al., 2019). The open circuit potential (OCP) measured before EIS analysis under dark and light irradiation were combined in Figure 27. First, we should note that electrodes with CQDs in direct contact with ITO have similar OCP values, which shift to negative potentials under blue and UV light. While for NiTSPc/CQDs electrodes the potential shifts to more positive ones under UV and blue irradiation, the NiPc electrode shifts to more negative potential under UV light. One can note that electrodes with CQDs have larger ΔOCP, showing higher photovoltages. This indicates an increased band bending at the CQD/electrolyte interface (Chong et al., 2021).

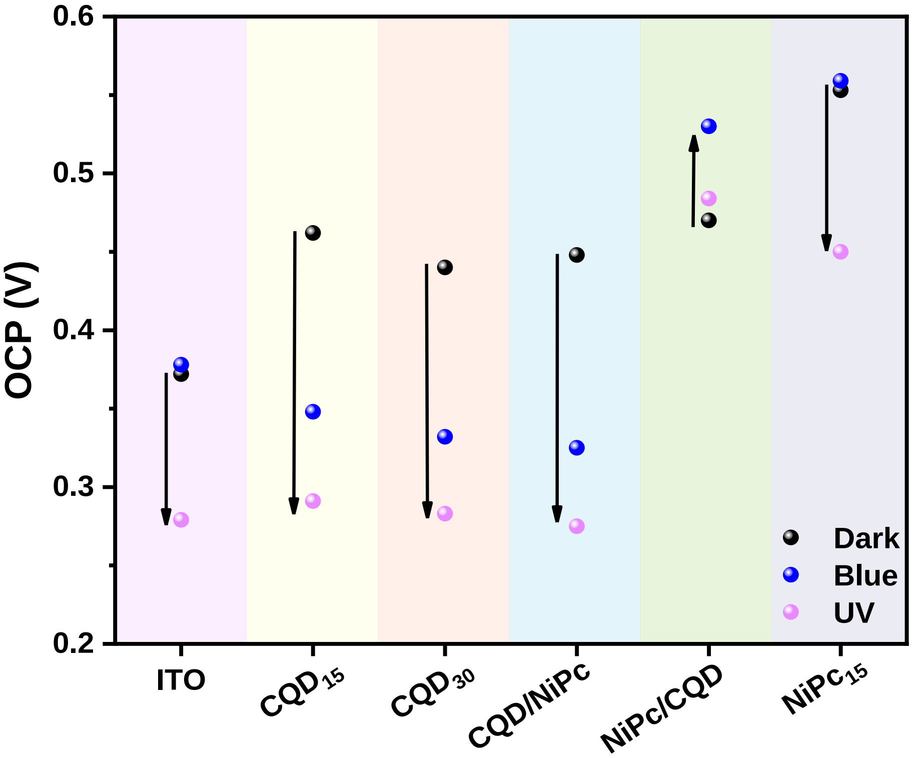

Figure 28. OCP values for electrodes were measured at dark and under blue and UV irradiation. Source: own author.

5.3.2.1. Proposed mechanisms for the photoelectrocatalytic reactions

The results previously presented show the photoelectrochemical performance of four working electrodes assembled with NiTSPc and/or CQDs. The increase in photocurrent density using CQD electrodes makes them potential sources for electron transfer intermediation for both electron-hole formation and suppression of charge recombination. Therefore, herein we presented the possible mechanisms for the photoelectrocatalytic reactions of those working electrodes with better performance, that is, NiTSPc/CQD and CQD_{15}.

For the mechanism of NiTSPc/CQD, we considered that photogenerated electrons were transferred to NiTSPc when that was oxidized by anodic potentials, and the respective holes were responsible for the oxidation of some species A in the electrolyte (Figure 25A).

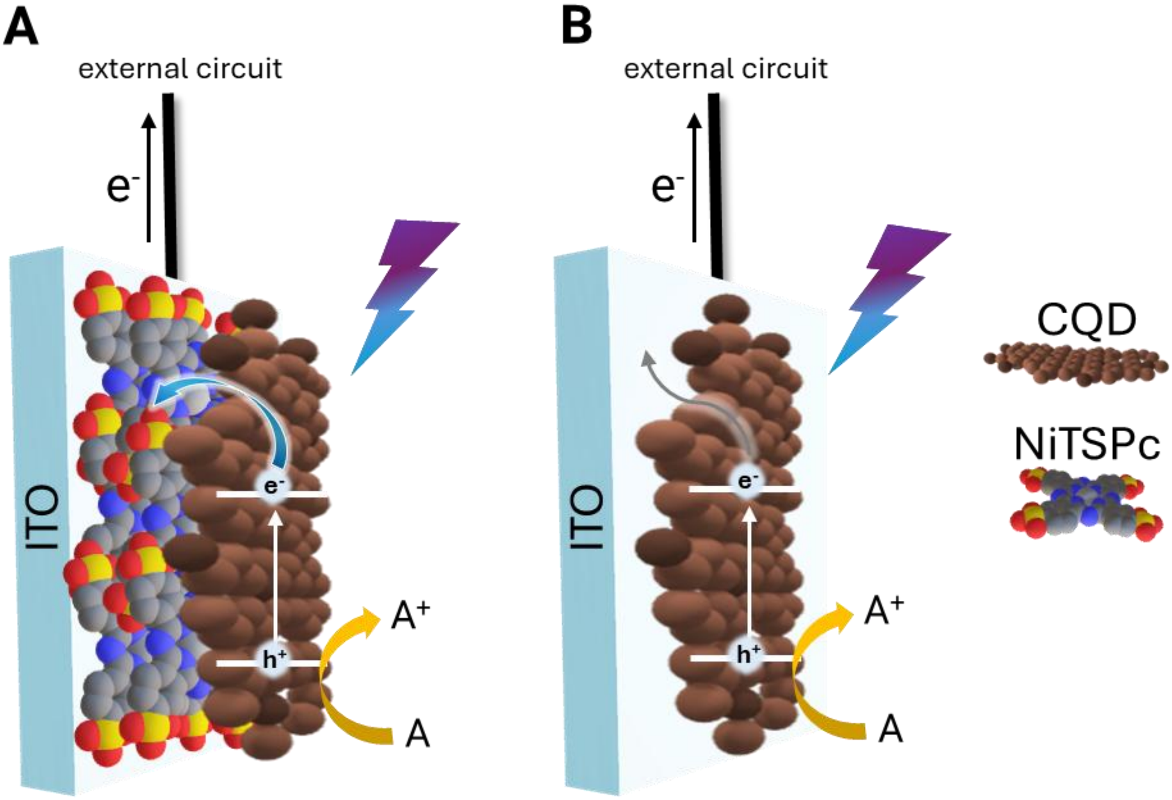

Figure 29. Schematic representation of NiTSPc/CQD (A) and CQD15 (B) under irradiation. The incident light generates electron-hole pairs which can oxidate some species A in the electrolyte through a photoelectrocatalytic reaction.
Source: own author.

Furthermore, the mechanism of CQD_{15} (Figure 25B) shows that the assembly of CQDs onto the ITO substrate increases the surface conductivity. Moreover, under UV and blue irradiation the photocurrent density was increased indicating the generation of photoexcited electrons. These electrons flow through the system revealing the suppression of charge recombination and enabling the efficient interfacial electron transfer process which is required for photoelectrocatalytic activity.

Briefly, this thesis presents that the conjugation of CQDs onto NiPc significantly boosts the photoelectrochemical water oxidation performance. Moreover, the results show that CQDs from lignocellulosic biomass have a direct photoelectrochemical response under UV and blue light irradiation; hence, sugarcane biomass, specifically, is an excellent carbon source for facile synthesis of CQDs being an environment-friendly nanomaterial for photoelectrocatalytic applications.

6. CONCLUSIONS AND PERSPECTIVES

In this dissertation, we aimed to synthesize CQDs from lignocellulosic biomass for application in photoelectrocatalysis. The methodology of pyrolysis followed by acid treatment was effective for this purpose. The hydrodynamic diameter measured by the DLS technique was 1.06 nm, and the zeta potential = -22.6 mV which provides the suspension stability. Through FTIR and Raman spectroscopy, we observed the presence of oxygen-containing functional groups which was a basis to explain the fluorescence properties of the nanomaterial together with UV-Vis and fluorescence spectroscopy results. The bandgap value of 4.66 eV derived from UV-Vis spectra confirms the semiconductor character of the CDQ.

To investigate the photoelectrocatalytic performance, the CQDs were assembled onto an ITO substrate with PAH as a positive polyelectrolyte. The conjugation of a phthalocyanine, NiTSPc, was also implemented to verify the effect on photocurrent, hence in the photoelectrocatalytic process. All electrodes showed higher photocurrent in comparison to the bare ITO, but NiTSPc/CQD and CQD_{15} electrodes demonstrated better performance under the conditions tested. Furthermore, we proposed a mechanism for the photoelectrocatalytic behavior and to explain the role of light irradiation in the process.

The results confirmed the direct photoelectrocatalytic response of CQDs derived from lignocellulosic biomass under UV (365 nm) and blue light (405 nm) irradiation. Thus, this approach represents a low-cost production of CQDs for applications in photoelectrocatalysis.

Concerning the route of synthesis, one should investigate the possibility of reducing the presence of ions to obtain a CQD suspension with lower ionic strength. Although the dialysis method can be used one should remember the problems concerning agglomeration. Techniques, such as AFM or SEM, should be performed to verify the film thickness. Finally, the agglomerated particulates of CQDs onto the ITO electrode present high porosity and sites that can be hostage for binding of other molecules for photoelectrocatalysis. An example is the application for biophotoelectrocatalysis, where we could immobilize ADH onto a CQD electrode and investigate the possible photocatalytic oxidation of ethanol to acetaldehyde.

REFERENCES

Abbas, A., Rubab, S., Rehman, A., Irfan, S., Sharif, H. M. A., Liang, Q., & Tabish, T. A. (2023). One-step green synthesis of biomass-derived graphene quantum dots as a highly selective optical sensing probe. *Materials Today Chemistry*, *30*, 101555. https://doi.org/10.1016/j.mtchem.2023.101555

Abbas, A., Tabish, T. A., Bull, S. J., Lim, T. M., & Phan, A. N. (2020). High yield synthesis of graphene quantum dots from biomass waste as a highly selective probe for Fe3+ sensing. *Scientific Reports*, *10*(1), 1–16. https://doi.org/10.1038/s41598-020-78070-2

Ahlawat, A., Dhiman, T. K., Solanki, P. R., & Rana, P. S. (2023). Facile synthesis of carbon dots via pyrolysis and their application in photocatalytic degradation of rhodamine B (RhB). *Environmental Science and Pollution Research*, *0123456789*. https://doi.org/10.1007/s11356-023-25604-6

Ahmed, S. F., Kumar, P. S., Ahmed, B., Mehnaz, T., Shafiullah, G. M., Nguyen, V. N., Duong, X. Q., Mofijur, M., Badruddin, I. A., & Kamangar, S. (2024). Carbon-based nanomaterials: Characteristics, dimensions, advances and challenges in enhancing photocatalytic hydrogen production. *International Journal of Hydrogen Energy*, *52*, 424–442. https://doi.org/10.1016/j.ijhydene.2023.03.185

Alafeef, M., Srivastava, I., Aditya, T., & Pan, D. (2024). Carbon Dots: From Synthesis to Unraveling the Fluorescence Mechanism. *Small*, *20*(4), 1–13. https://doi.org/10.1002/smll.202303937

Aldakhil, F. (2024). *carbon dots derived from biomass waste for fl uorescence determination of valsartan*. 19969–19982. https://doi.org/10.1039/d4ra02398f

Alenad, A. M., Taha, T. A., Zayed, M., Gamal, A., Shaaban, M., Ahmed, A. M., & Mohamed, F. (2023). Impact of carbon nanotubes concentrations on the performance of carbon nanotubes/zinc oxide nanocomposite for photoelectrochemical water splitting. *Journal of Electroanalytical Chemistry*, *943*(May), 117579. https://doi.org/10.1016/j.jelechem.2023.117579

Alencar, W. S., Crespilho, F. N., Martins, M. V. A., Zucolotto, V., Oliveira, O. N., & Silva, W. C. (2009). Synergistic interaction between gold nanoparticles and nickel phthalocyanine in layer-by-layer (LbL) films: Evidence of constitutional dynamic chemistry (CDC). *Physical Chemistry Chemical Physics*, *11*(25), 5086–5091. https://doi.org/10.1039/b821915j

Alencar, W. S., Crespilho, F. N., Santos, M. R. M. C., Zucolotto, V., Oliveira, O. N., & Silva, W. C. (2007). Influence of film architecture on the charge-transfer reactions of metallophthalocyanine layer-by-layer films. *Journal of Physical Chemistry C, 111*(34), 12817–12821. https://doi.org/10.1021/jp070695r

Ali, M., Anjum, A. S., Bibi, A., Wageh, S., Sun, K. C., & Jeong, S. H. (2022). Gradient heating-induced bi-phase synthesis of carbon quantum dots (CQDs) on graphene-coated carbon cloth for efficient photoelectrocatalysis. *Carbon*, *196*(February), 649–662. https://doi.org/10.1016/j.carbon.2022.05.040

Ali, M., Riaz, R., Bae, S., Lee, H. S., Jeong, S. H., & Ko, M. J. (2020). Layer-by-Layer Self-Assembly of Hollow Nitrogen-Doped Carbon Quantum Dots on Cationized Textured Crystalline Silicon Solar Cells for an Efficient Energy Down-Shift. *ACS Applied Materials and Interfaces*, *12*(9), 10369–10381. https://doi.org/10.1021/acsami.9b21087

Aragaw, B. A. (2020). Reduced graphene oxide-intercalated graphene oxide nano-hybrid for enhanced photoelectrochemical water reduction. *Journal of Nanostructure in Chemistry*, *10*(1), 9–18. https://doi.org/10.1007/s40097-019-00324-x

Bao, L., Liu, C., Zhang, Z. L., & Pang, D. W. (2015). Photoluminescence-tunable carbon nanodots: Surface-state energy-gap tuning. *Advanced Materials*, *27*(10), 1663–1667. https://doi.org/10.1002/adma.201405070

Bian, J., Feng, J., Zhang, Z., Sun, J., Chu, M., Sun, L., Li, X., Tang, D., & Jing, L. (2020). Graphene-modulated assembly of zinc phthalocyanine on BiVO4nanosheets for efficient visible-light catalytic conversion of CO2. *Chemical Communications*, *56*(36), 4926–4929. https://doi.org/10.1039/d0cc01518k

Bian, J., Huang, C., Wang, L., Hung, T., Daoud, W. A., & Zhang, R. (2014). Carbon dot loading and TiO2 nanorod length dependence of photoelectrochemical properties in carbon dot/TiO2 nanorod array nanocomposites. *ACS Applied Materials and Interfaces*, *6*(7), 4883–4890. https://doi.org/10.1021/am4059183

Bienkowski, K., Solarska, R., Trinh, L., Widera-Kalinowska, J., Al-Anesi, B., Liu, M., Grandhi, G. K., Vivo, P., Oral, B., Yılmaz, B., & Yıldırım, R. (2024). Halide Perovskites for Photoelectrochemical Water Splitting and CO2 Reduction: Challenges and Opportunities. *ACS Catalysis* , *14*(9), 6603–6622. https://doi.org/10.1021/acscatal.3c06040

Blaskievicz, S. F., Francisco, J. L., Marken, F., & Mascaro, L. H. (2024). Carbon Nitrides in Photoelectrochemistry: State of the Art and Perspectives Beyond Water Splitting. *ACS Applied*

Energy Materials, *7*(8), 3021–3038. https://doi.org/10.1021/acsaem.3c02623

Bockris, J. O., & Reddy, A. K. N. (2004). *Modern Electrochemistry 2B*. Kluwer Academic.

Brachi, P. (2020). Synthesis of fluorescent carbon quantum dots (CQDs) through the mild thermal treatment of agro-industrial residues assisted by γ-alumina. *Biomass Conversion and Biorefinery*, *10*(4), 1301–1312. https://doi.org/10.1007/s13399-019-00503-4

Cayuela, A., Soriano, M. L., Carrillo-Carrión, C., & Valcárcel, M. (2016). Semiconductor and carbon-based fluorescent nanodots: The need for consistency. *Chemical Communications*, *52*(7), 1311–1326. https://doi.org/10.1039/c5cc07754k

Chai, X., He, H., Fan, H., Kang, X., & Song, X. (2019). A hydrothermal-carbonization process for simultaneously production of sugars, graphene quantum dots, and porous carbon from sugarcane bagasse. *Bioresource Technology*, *282*(January), 142–147. https://doi.org/10.1016/j.biortech.2019.02.126

Chaudhary, S., Kumar, S., Kaur, B., & Mehta, S. K. (2016). Potential prospects for carbon dots as a fluorescence sensing probe for metal ions. *RSC Advances*, *6*(93), 90526–90536. https://doi.org/10.1039/c6ra15691f

Chen, Q., Lin, G., Meng, L., Zhou, L., Hu, L., Nong, J., Li, Y., Wang, J., Hu, K., & Yu, Q. (2020). Enhanced photoelectric performance of TiO2 nanotubes sensitized with carbon dots derived from bagasse. *Chemical Physics Letters*, *749*(March), 137428. https://doi.org/10.1016/j.cplett.2020.137428

Chen, T. W., Ramachandran, R., Chen, S. M., Anushya, G., Al-Sehemi, A. G., Mariyappan, V., Alargarsamy, S., Alam, M. M., Mahesh, T. C., Kalimuthu, P., & Kannan, R. (2024). An overview of semiconductor electrode materials for photoelectrochemical water splitting and CO2 conversion. *International Journal of Electrochemical Science*, *19*(5), 100542. https://doi.org/10.1016/j.ijoes.2024.100542

Chen, X., Zhang, X., Wang, H., Guo, H., & Cui, W. (2024). Boron functionalized carbon-based metal-free catalyst for efficient photoelectrocatalytic degradation of pollutants. *Journal of Materials Science*, *0123456789*. https://doi.org/10.1007/s10853-024-09497-5

Chen, Z., Liu, Y., & Kang, Z. (2022). Diversity and Tailorability of Photoelectrochemical Properties of Carbon Dots. *Accounts of Chemical Research*, *55*(21), 3110–3124. https://doi.org/10.1021/acs.accounts.2c00570

Chong, R., Wang, Z., Lv, J., Rong, J., Zhang, L., Jia, Y., Wang, L., Chang, Z., & Wang, X.

(2021). A hybrid CoOOH-rGO/Fe2O3 photoanode with spatial charge separation and charge transfer for efficient photoelectrochemical water oxidation. *Journal of Catalysis*, *399*, 170–181. https://doi.org/10.1016/j.jcat.2021.05.006

Claramunt, S., Varea, A., López-Díaz, D., Velázquez, M. M., Cornet, A., & Cirera, A. (2015). The importance of interbands on the interpretation of the raman spectrum of graphene oxide. *Journal of Physical Chemistry C*, *119*(18), 10123–10129. https://doi.org/10.1021/acs.jpcc.5b01590

De Sousa Luz, R. A., Martins, M. V. A., Magalhães, J. L., Siqueira, J. R., Zucolotto, V., Oliveira, O. N., Crespilho, F. N., & Da Silva, W. C. (2011). Supramolecular architectures in layer-by-layer films of single-walled carbon nanotubes, chitosan and cobalt (II) phthalocyanine. *Materials Chemistry and Physics*, *130*(3), 1072–1077. https://doi.org/10.1016/j.matchemphys.2011.08.038

Deepanraj, S. R. N. S. B. (2024). *Development and characterization of polymeric thermal interface material using aluminized glass fiber , bamboo fiber , and sugarcane bagasse carbon quantum dots*. *0123456789*. https://doi.org/10.1007/s13399-024-05595-1

Ding, H., Li, X. H., Chen, X. B., Wei, J. S., Li, X. B., & Xiong, H. M. (2020). Surface states of carbon dots and their influences on luminescence. *Journal of Applied Physics*, *127*(23). https://doi.org/10.1063/1.5143819

Ding, H., Yu, S. B., Wei, J. S., & Xiong, H. M. (2016). Full-color light-emitting carbon dots with a surface-state-controlled luminescence mechanism. *ACS Nano*, *10*(1), 484–491. https://doi.org/10.1021/acsnano.5b05406

Dong, Y., Lin, J., Chen, Y., Fu, F., Chi, Y., & Chen, G. (2014). Graphene quantum dots, graphene oxide, carbon quantum dots and graphite nanocrystals in coals. *Nanoscale*, *6*(13), 7410–7415. https://doi.org/10.1039/c4nr01482k

Dutta Choudhury, S., Chethodil, J. M., Gharat, P. M., Praseetha, P. K., & Pal, H. (2017). PH-Elicited Luminescence Functionalities of Carbon Dots: Mechanistic Insights. *Journal of Physical Chemistry Letters*, *8*(7), 1389–1395. https://doi.org/10.1021/acs.jpclett.7b00153

Ehtesabi, H., Hallaji, Z., Najafi Nobar, S., & Bagheri, Z. (2020). Carbon dots with pH-responsive fluorescence: a review on synthesis and cell biological applications. *Microchimica Acta*, *187*(2). https://doi.org/10.1007/s00604-019-4091-4

Fang, X. W., Chang, H., Wu, T., Yeh, C. H., Hsiao, F. L., Ko, T. S., Hsieh, C. L., Wu, M. Y.,

& Lin, Y. W. (2024). Green Synthesis of Carbon Quantum Dots and Carbon Quantum Dot-Gold Nanoparticles for Applications in Bacterial Imaging and Catalytic Reduction of Aromatic Nitro Compounds. *ACS Omega*. https://doi.org/10.1021/acsomega.4c00833

Farooq, A., Karimov, K. S., Ahmed, N., Ali, T., Khalid Alamgir, M., & Usman, M. (2015). Copper phthalocyanine and metal free phthalocyanine bulk heterojunction photodetector. *Physica B: Condensed Matter*, *457*, 17–21. https://doi.org/10.1016/j.physb.2014.09.032

Feng, J., Ran, X., Wang, Y., Zhan, S., Wang, L., Xiao, B., Zhong, Y., Xu, D., Feng, G., & Dai, Z. (2024). Modulation of surface oxygen vacancies on bismuth-rich Bi5O7I nanoparticles for efficiently boosting photocatalytic overall water splitting. *Applied Surface Science*, *655*(February), 159517. https://doi.org/10.1016/j.apsusc.2024.159517

Feng, X., & Zhang, Y. (2019). A simple and green synthesis of carbon quantum dots from coke for white light-emitting devices. *RSC Advances*, *9*(58), 33789–33793. https://doi.org/10.1039/c9ra06946a

Fox, M. (2010). *Optical properties of solids* (2nd ed.). Oxford University Press.

Furini, L. N., Martin, C. S., Camacho, S. A., Rubira, R. J. G., Fernandes, J. D., Silva, E. A., Gomes, T. C., Stunges, G. M., Constantino, C. J. L., & Alessio, P. (2020). Electrochemical properties of nickel phthalocyanine: The effect of thin film morphology tuned by deposition techniques. *Thin Solid Films*, *699*(May 2019), 137897. https://doi.org/10.1016/j.tsf.2020.137897

Gao, L., Wang, L., Kuklin, A. V., Gao, J., Yin, S., Ågren, H., & Zhang, H. (2021). A Facile Approach for Elemental-Doped Carbon Quantum Dots and Their Application for Efficient Photodetectors. *Small*, *17*(52), 1–9. https://doi.org/10.1002/smll.202105683

Gao, Q., Guo, X., Meng, L., Liu, M., Chen, L., Li, H., & Hu, J. (2023). N, S/P co-doped hemicellulose-based carbon dots with tunable fluorescence for anti-counterfeiting. *International Journal of Biological Macromolecules*, *253*(P6), 126332. https://doi.org/10.1016/j.ijbiomac.2023.126332

García de Arquer, F. P., Talapin, D. V., Klimov, V. I., Arakawa, Y., Bayer, M., & Sargent, E. H. (2021). Semiconductor quantum dots: Technological progress and future challenges. *Science (New York, N.Y.)*, *373*(6555). https://doi.org/10.1126/science.aaz8541

Gazzetto, M., Sciortino, A., Nazari, M., Rohwer, E., Giammona, G., Mauro, N., Feurer, T., Messina, F., & Cannizzo, A. (2020). Photocycle of Excitons in Nitrogen-Rich Carbon

Nanodots: Implications for Photocatalysis and Photovoltaics. *ACS Applied Nano Materials*, *3*(7), 6925–6934. https://doi.org/10.1021/acsanm.0c01259

Gelderman, K., Lee, L., & Donne, S. W. (2007). Flat-band potential of a semiconductor: Using the Mott-Schottky equation. *Journal of Chemical Education*, *84*(4), 685–688. https://doi.org/10.1021/ed084p685

Gholipour, A., Jahanshahi, M., & Emadi, H. (2024). Synthesis of Carbon Quantum Dots and Fe-Doped Carbon Quantum Dots as Fluorescent Probes via One-Step Microwave Process for Rapid and Accurate Detection of Diclofenac Sodium. *Journal of Cluster Science*, *35*(1), 237–251. https://doi.org/10.1007/s10876-023-02480-1

Han, W., Li, D., Zhang, M., Ximin, H., Duan, X., Liu, S., & Wang, S. (2020). Photocatalytic activation of peroxymonosulfate by surface-tailored carbon quantum dots. *Journal of Hazardous Materials*, *395*(April). https://doi.org/10.1016/j.jhazmat.2020.122695

Hemasiri, B. W. N. H., Kim, J. K., & Lee, J. M. (2017). Fabrication of highly conductive graphene/ITO transparent bi-film through CVD and organic additives-free sol-gel techniques. *Scientific Reports*, *7*(1), 1–12. https://doi.org/10.1038/s41598-017-18063-w

Huang, G., Chen, X., Wang, C., Zheng, H., Huang, Z., Chen, D., & Xie, H. (2017). Photoluminescent carbon dots derived from sugarcane molasses: Synthesis, properties, and applications. *RSC Advances*, *7*(75), 47840–47847. https://doi.org/10.1039/c7ra09002a

Jia, X., Li, J., & Wang, E. (2012). One-pot green synthesis of optically pH-sensitive carbon dots with upconversion luminescence. *Nanoscale*, *4*(18), 5572–5575. https://doi.org/10.1039/c2nr31319g

Jiang, K., Sun, S., Zhang, L., Lu, Y., Wu, A., Cai, C., & Lin, H. (2015). Red, Green, and Blue Luminescence by Carbon Dots: Full-Color Emission Tuning and Multicolor Cellular Imaging. *Angewandte Chemie*, *127*(18), 5450–5453. https://doi.org/10.1002/ange.201501193

Jing, S., Zhao, Y., Sun, R. C., Zhong, L., & Peng, X. (2019). Facile and High-Yield Synthesis of Carbon Quantum Dots from Biomass-Derived Carbons at Mild Condition. *ACS Sustainable Chemistry and Engineering*, *7*(8), 7833–7843. https://doi.org/10.1021/acssuschemeng.9b00027

John, V. L., Nair, Y., & Vinod, T. P. (2021). Doping and Surface Modification of Carbon Quantum Dots for Enhanced Functionalities and Related Applications. *Particle and Particle Systems Characterization*, *38*(11), 1–28. https://doi.org/10.1002/ppsc.202100170

Jorio, A., & Souza Filho, A. G. (2016). Raman Studies of Carbon Nanostructures. *Annual Review of Materials Research*, *46*, 357–382. https://doi.org/10.1146/annurev-matsci-070115-032140

Kasinathan, K., Samayanan, S., Marimuthu, K., & Yim, J. H. (2022). Green synthesis of multicolour fluorescence carbon quantum dots from sugarcane waste: Investigation of mercury (II) ion sensing, and bio-imaging applications. *Applied Surface Science*, *601*(March), 154266. https://doi.org/10.1016/j.apsusc.2022.154266

Klein, J., Kampermann, L., Mockenhaupt, B., Behrens, M., Strunk, J., & Bacher, G. (2023). Limitations of the Tauc Plot Method. *Advanced Functional Materials*, *33*(47), 1–19. https://doi.org/10.1002/adfm.202304523

Kolay, A., Ghosal, P., & Deepa, M. (2020). Novel Integration of Nickel Phthalocyanine/Nickel Oxide-Based Photocathodes and Copper-Encapsulated Carbon-Dot-Cosensitized Photoanodes in Tandem for a Highly Efficient Solar Cell. *ACS Sustainable Chemistry and Engineering*, *8*(23), 8593–8603. https://doi.org/10.1021/acssuschemeng.0c01107

Kong, W., Zhang, X., Liu, S., Zhou, Y., Chang, B., Zhang, S., Fan, H., & Yang, B. (2019). N Doped Carbon Dot Modified WO3 Nanoflakes for Efficient Photoelectrochemical Water Oxidation. *Advanced Materials Interfaces*, *6*(1), 1–8. https://doi.org/10.1002/admi.201801653

Koo, B., Baek, H., & Cho, J. (2012). Control over memory performance of layer-by-layer assembled metal phthalocyanine multilayers via molecular-level manipulation. *Chemistry of Materials*, *24*(6), 1091–1099. https://doi.org/10.1021/cm2033959

Kumari, M., Chaudhary, G. R., Chaudhary, S., Huang, M., & Guo, Z. (2024). Transformation of waste rice straw to carbon quantum dots and their potential chemical sensing application: green and sustainable approach to overcome stubble burning issues. *Biomass Conversion and Biorefinery*, *14*(6), 7507–7518. https://doi.org/10.1007/s13399-022-02761-1

Lakowicz, J. R. (2006). Principles of Fluorescence Spectroscopy. In *Geofisica pura e applicata* (Vol. 33, Issue 1). Springer Science.

Li, C., He, J., Xiao, Y., Li, Y., & Delaunay, J. J. (2020). Earth-abundant Cu-based metal oxide photocathodes for photoelectrochemical water splitting. *Energy and Environmental Science*, *13*(10), 3269–3306. https://doi.org/10.1039/d0ee02397c

Li, H., Kang, Z., Liu, Y., & Lee, S. T. (2012). Carbon nanodots: Synthesis, properties and applications. *Journal of Materials Chemistry*, *22*(46), 24230–24253.

https://doi.org/10.1039/c2jm34690g

Li, W., Wang, X., Lin, J., Meng, X., Wang, L., Wang, M., Jing, Q., Song, Y., Vomiero, A., & Zhao, H. (2024). Controllable and large-scale synthesis of carbon quantum dots for efficient solid-state optical devices. *Nano Energy*, *122*(December 2023), 109289. https://doi.org/10.1016/j.nanoen.2024.109289

Lim, H., Kim, J. Y., Evans, E. J., Rai, A., Kim, J. H., Wygant, B. R., & Mullins, C. B. (2017). Activation of a Nickel-Based Oxygen Evolution Reaction Catalyst on a Hematite Photoanode via Incorporation of Cerium for Photoelectrochemical Water Oxidation. *ACS Applied Materials and Interfaces*, *9*(36), 30654–30661. https://doi.org/10.1021/acsami.7b08239

Lim, S. Y., Shen, W., & Gao, Z. (2015). Carbon quantum dots and their applications. *Chemical Society Reviews*, *44*(1), 362–381. https://doi.org/10.1039/c4cs00269e

Liu, H., Ye, T., & Mao, C. (2007). Fluorescent Carbon Nanoparticles Derived from Candle Soot. *Angewandte Chemie*, *119*(34), 6593–6595. https://doi.org/10.1002/ange.200701271

Liu, Y., Xiao, N., Gong, N., Wang, H., Shi, X., Gu, W., & Ye, L. (2014). One-step microwave-assisted polyol synthesis of green luminescent carbon dots as optical nanoprobes. *Carbon*, *68*, 258–264. https://doi.org/10.1016/j.carbon.2013.10.086

Liu, Y., Zhao, Y., & Zhang, Y. (2014). One-step green synthesized fluorescent carbon nanodots from bamboo leaves for copper(II) ion detection. *Sensors and Actuators, B: Chemical*, *196*, 647–652. https://doi.org/10.1016/j.snb.2014.02.053

Liu, Y., Zhu, C., Gao, Y., Yang, L., Xu, J., Zhang, X., Lu, C., Wang, Y., & Zhu, Y. (2020). Biomass-derived nitrogen self-doped carbon dots via a simple one-pot method: Physicochemical, structural, and luminescence properties. *Applied Surface Science*, *510*(January), 145437. https://doi.org/10.1016/j.apsusc.2020.145437

Luo, Z., Wu, C., Yan, M., Yu, X., Yu, X., & Qian, Q. (2024). Enhancing detectivity of organic photodetectors through the biomass carbon quantum dots from sugarcane bagasse. *Materials Chemistry and Physics*, *316*(January), 129056. https://doi.org/10.1016/j.matchemphys.2024.129056

Malara, F., Minguzzi, A., Marelli, M., Morandi, S., Psaro, R., Dal Santo, V., & Naldoni, A. (2015). α-Fe2O3/NiOOH: An Effective Heterostructure for Photoelectrochemical Water Oxidation. *ACS Catalysis*, *5*(9), 5292–5300. https://doi.org/10.1021/acscatal.5b01045

Mandal, B., Sarkar, S., & Sarkar, P. (2012). Exploring the electronic structure of graphene quantum dots. *Journal of Nanoparticle Research*, *14*(12). https://doi.org/10.1007/s11051-012-1317-3

Martin, C. S., Kavazoi, H. S., Miyazaki, C. M., Alessio, P., & Constantino, C. J. L. (2023). Nickel Tetrasulfonated Phthalocyanine Decorated with AuNP as a Double Sensorial Platform: SERS and Electrochemical. *Chemosensors*, *11*(7). https://doi.org/10.3390/chemosensors11070372

Messina, M. M., Barrionuevo, S. D., Coustet, M. E., Kreuzer, M. P., Saccone, F. D., dos Santos Claro, P. C., & Ibañez, F. J. (2021). Graphene and Carbon Dots for Photoanodes with Enhanced Performance. *ACS Applied Nano Materials*, *4*(7), 7309–7318. https://doi.org/10.1021/acsanm.1c01295

Migliorini, F., Belmuso, S., Dondè, R., De Iuliis, S., & Altman, I. (2022). To optical properties of carbon nanoparticles: A need in comprehending Urbach energy. *Carbon Trends*, *8*, 100184. https://doi.org/10.1016/j.cartre.2022.100184

Molaei, M. J. (2020a). Principles, mechanisms, and application of carbon quantum dots in sensors: A review. *Analytical Methods*, *12*(10), 1266–1287. https://doi.org/10.1039/c9ay02696g

Molaei, M. J. (2020b). The optical properties and solar energy conversion applications of carbon quantum dots: A review. *Solar Energy*, *196*(November 2019), 549–566. https://doi.org/10.1016/j.solener.2019.12.036

Ninan, G. G., Varghese, M., & Balachandran, M. (2024). Enhancing the stability of DSSC by Co-activation of microwave synthesized TiO2 with biomass derived carbon dots. *Optical Materials*, *154*(April), 115730. https://doi.org/10.1016/j.optmat.2024.115730

Nizam, N. U. M., Hanafiah, M. M., Mahmoudi, E., & Mohammad, A. W. (2023). Synthesis of highly fluorescent carbon quantum dots from rubber seed shells for the adsorption and photocatalytic degradation of dyes. *Scientific Reports*, *13*(1), 1–17. https://doi.org/10.1038/s41598-023-40069-w

Oza, G., Ravichandran, M., Merupo, V. I., Shinde, S., Mewada, A., Ramirez, J. T., Velumani, S., Sharon, M., & Sharon, M. (2016). Camphor-mediated synthesis of carbon nanoparticles, graphitic shell encapsulated carbon nanocubes and carbon dots for bioimaging. *Scientific Reports*, *6*(July 2015), 1–9. https://doi.org/10.1038/srep21286

Paltrinieri, L., Wang, M., Sachdeva, S., Besseling, N. A. M., Sudhölter, E. J. R., & De Smet,

L. C. P. M. (2017). Fe3O4 nanoparticles coated with a guanidinium-functionalized polyelectrolyte extend the pH range for phosphate binding. *Journal of Materials Chemistry A*, *5*(35), 18476–18485. https://doi.org/10.1039/c7ta04054g

Pandey, F. P., Rastogi, A., & Singh, S. (2020). Optical properties and zeta potential of carbon quantum dots (CQDs) dispersed nematic liquid crystal 4′- heptyl-4-biphenylcarbonitrile (7CB). *Optical Materials*, *105*(April), 109849. https://doi.org/10.1016/j.optmat.2020.109849

Pandiyan, S., Arumugam, L., Srirengan, S. P., Pitchan, R., Sevugan, P., Kannan, K., Pitchan, G., Hegde, T. A., & Gandhirajan, V. (2020). Biocompatible Carbon Quantum Dots Derived from Sugarcane Industrial Wastes for Effective Nonlinear Optical Behavior and Antimicrobial Activity Applications. *ACS Omega*, *5*(47), 30363–30372. https://doi.org/10.1021/acsomega.0c03290

Patel, D. K., Won, S. Y., Jung, E., Deb Dutta, S., Patil, T. V., Lim, K. T., & Soo Han, S. (2024). Assessment of the biocompatibility and bioimaging potential of fluorescent carbon dots derived from waste biomass. *Materials Letters*, *361*(December 2023), 136152. https://doi.org/10.1016/j.matlet.2024.136152

Patey, T. J., Hintennach, A., La Mantia, F., & Novák, P. (2009). Electrode engineering of nanoparticles for lithium-ion batteries-Role of dispersion technique. *Journal of Power Sources*, *189*(1), 590–593. https://doi.org/10.1016/j.jpowsour.2008.09.091

Peng, J., Gao, W., Gupta, B. K., Liu, Z., Romero-Aburto, R., Ge, L., Song, L., Alemany, L. B., Zhan, X., Gao, G., Vithayathil, S. A., Kaipparettu, B. A., Marti, A. A., Hayashi, T., Zhu, J. J., & Ajayan, P. M. (2012). Graphene quantum dots derived from carbon fibers. *Nano Letters*, *12*(2), 844–849. https://doi.org/10.1021/nl2038979

Pourmadadi, M., Rahmani, E., Rajabzadeh-Khosroshahi, M., Samadi, A., Behzadmehr, R., Rahdar, A., & Ferreira, L. F. R. (2023). Properties and application of carbon quantum dots (CQDs) in biosensors for disease detection: A comprehensive review. *Journal of Drug Delivery Science and Technology*, *80*(August 2022), 104156. https://doi.org/10.1016/j.jddst.2023.104156

Prakash, J., Prasad, U., Alexander, R., Bahadur, J., Dasgupta, K., & Kannan, A. N. M. (2019). Photoelectrochemical Solar Water Splitting: The Role of the Carbon Nanomaterials in Bismuth Vanadate Composite Photoanodes toward Efficient Charge Separation and Transport. *Langmuir*, *35*(45), 14492–14504. https://doi.org/10.1021/acs.langmuir.9b02782

Qiu, Y., Li, D., Li, Y., Ma, X., & Li, J. (2022). Green carbon quantum dots from sustainable lignocellulosic biomass and its application in the detection of Fe3+. *Cellulose*, *29*(1), 367–378. https://doi.org/10.1007/s10570-021-04314-7

Rajender, G., & Giri, P. K. (2016). Formation mechanism of graphene quantum dots and their edge state conversion probed by photoluminescence and Raman spectroscopy. *Journal of Materials Chemistry C*, *4*(46), 10852–10865. https://doi.org/10.1039/c6tc03469a

Raju, K. S., Das, G. S., & Tripathi, K. M. (2023). Nitrogen-doped carbon quantum dots from biomass as a FRET-based sensing platform for the selective detection of H2O2 and aspartic acid. *RSC Sustainability*, *2*(1), 223–232. https://doi.org/10.1039/d3su00343d

Ranganathan, K., Morais, A., Nongwe, I., Longo, C., Nogueira, A. F., & Coville, N. J. (2016). Study of photoelectrochemical water splitting using composite films based on TiO2 nanoparticles and nitrogen or boron doped hollow carbon spheres as photoanodes. *Journal of Molecular Catalysis A: Chemical*, *422*, 165–174. https://doi.org/10.1016/j.molcata.2015.10.024

Rasal, A. S., Yadav, S., Yadav, A., Kashale, A. A., Manjunatha, S. T., Altaee, A., & Chang, J. Y. (2021). Carbon Quantum Dots for Energy Applications: A Review. *ACS Applied Nano Materials*, *4*(7), 6515–6541. https://doi.org/10.1021/acsanm.1c01372

Rogers, B., Pennathur, S., & Adams, J. (2012). Nanotechnology: Understanding Small Systems, Second Edition. In *Nanotechnology: Understanding Small Systems, Second Edition*. https://doi.org/10.1201/b12783

Roy, A. K., Ghann, W., Rabi, S., Barua, J., Majumder, S., Amin, R., Ziaul Hyder, M. K. M., & Uddin, J. (2024). Hydrogen peroxide assisted synthesis of fluorescent carbon nanoparticles from teak leaves for dye-sensitized solar cells. *RSC Sustainability*, *2*(4), 1003–1013. https://doi.org/10.1039/d3su00452j

Roy, K., Ghosh, D., Sarkar, K., Devi, P., & Kumar, P. (2020). Chlorophyll(a)/Carbon Quantum Dot Bio-Nanocomposite Activated Nano-Structured Silicon as an Efficient Photocathode for Photoelectrochemical Water Splitting. *ACS Applied Materials and Interfaces*, *12*(33), 37218–37226. https://doi.org/10.1021/acsami.0c10279

Sahai, S., Jangra, A., Thomas, L. M., & Satsangi, V. R. (2023). Quantum Dots as Efficient Solar Energy Absorber: Review on Photovoltaics and Photoelectrochemical Systems. *Journal of The Institution of Engineers (India): Series D*. https://doi.org/10.1007/s40033-023-00490-x

Sayama, K. (2018). Production of high-value-added chemicals on oxide semiconductor photoanodes under visible light for solar chemical-conversion processes. *ACS Energy Letters*, *3*(5), 1093–1101. https://doi.org/10.1021/acsenergylett.8b00318

Schneider, K. (2020). Optical properties and electronic structure of V2O5, V2O3 and VO2. *Journal of Materials Science: Materials in Electronics*, *31*(13), 10478–10488. https://doi.org/10.1007/s10854-020-03596-0

Sendeku, M. G., Shifa, T. A., Dajan, F. T., Ibrahim, K. B., Wu, B., Yang, Y., Moretti, E., Vomiero, A., & Wang, F. (2024). Frontiers in Photoelectrochemical Catalysis: A Focus on Valuable Product Synthesis. *Advanced Materials*, *2308101*. https://doi.org/10.1002/adma.202308101

Setianto, S., Men, L. K., Bahtiar, A., Panatarani, C., & Joni, I. M. (2024). Carbon quantum dots with honeycomb structure: a novel synthesis approach utilizing cigarette smoke precursors. *Scientific Reports*, *14*(1), 1–8. https://doi.org/10.1038/s41598-024-52106-3

Shalom, M., Buhbut, S., Tirosh, S., & Zaban, A. (2012). Design rules for high-efficiency quantum-dot-sensitized solar cells: A multilayer approach. *Journal of Physical Chemistry Letters*, *3*(17), 2436–2441. https://doi.org/10.1021/jz3010078

Sharma, N., Prabakar, K., Ilango, S., Dash, S., & Tyagi, A. K. (2017). Optical band-gap and associated Urbach energy tails in defected AlN thin films grown by ion beam sputter deposition: Effect of assisted ion energy. *Advanced Materials Proceedings*, *2*(5), 342–346. https://doi.org/10.5185/amp.2017/511

Shen, D., Zhu, L., Wu, C., & Gu, S. (2020). State-of-the-art on the preparation, modification, and application of biomass-derived carbon quantum dots. *Industrial and Engineering Chemistry Research*, *59*(51), 22017–22039. https://doi.org/10.1021/acs.iecr.0c04760

Singleton, J. (2001). Band Theory and Electronic Properties of Solids. In *Band Theory and Electronic Properties of Solids*. https://doi.org/10.1093/oso/9780198506454.001.0001

Sohn, H., Kim, D. H., Yi, R., Tang, D., Lee, S. E., Jung, Y. S., & Wang, D. (2016). Semimicro-size agglomerate structured silicon-carbon composite as an anode material for high performance lithium-ion batteries. *Journal of Power Sources*, *334*, 128–136. https://doi.org/10.1016/j.jpowsour.2016.09.096

Song, Y., Zhu, S., Xiang, S., Zhao, X., Zhang, J., Zhang, H., Fu, Y., & Yang, B. (2014). Investigation into the fluorescence quenching behaviors and applications of carbon dots. *Nanoscale*, *6*(9), 4676–4682. https://doi.org/10.1039/c4nr00029c

Strauss, V., Margraf, J. T., Dirian, K., Syrgiannis, Z., Prato, M., Wessendorf, C., Hirsch, A., Clark, T., & Guldi, D. M. (2015). Carbon Nanodots: Supramolecular Electron Donor-Acceptor Hybrids Featuring Perylenediimides. *Angewandte Chemie - International Edition*, *54*(28), 8292–8297. https://doi.org/10.1002/anie.201502482

Sun, J., Bian, J., Li, J., Zhang, Z., Li, Z., Qu, Y., Bai, L., Yang, Z. Di, & Jing, L. (2020). Efficiently photocatalytic conversion of CO2 on ultrathin metal phthalocyanine/g-C3N4 heterojunctions by promoting charge transfer and CO2 activation. *Applied Catalysis B: Environmental*, *277*(April), 119199. https://doi.org/10.1016/j.apcatb.2020.119199

Sun, Y. P., Zhou, B., Lin, Y., Wang, W., Fernando, K. A. S., Pathak, P., Meziani, M. J., Harruff, B. A., Wang, X., Wang, H., Luo, P. G., Yang, H., Kose, M. E., Chen, B., Veca, L. M., & Xie, S. Y. (2006). Quantum-sized carbon dots for bright and colorful photoluminescence. *Journal of the American Chemical Society*, *128*(24), 7756–7757. https://doi.org/10.1021/ja062677d

Szybowicz, M., Nowicka, A. B., & Dychalska, A. (2018). Characterization of carbon nanomaterials by raman spectroscopy. In *Characterization of Nanomaterials: Advances and Key Technologies*. Elsevier Ltd. https://doi.org/10.1016/B978-0-08-101973-3.00001-8

Tang, L., Ji, R., Cao, X., Lin, J., Jiang, H., Li, X., Teng, K. S., Luk, C. M., Zeng, S., Hao, J., & Lau, S. P. (2012). Deep ultraviolet photoluminescence of water-soluble self-passivated graphene quantum dots. *ACS Nano*, *6*(6), 5102–5110. https://doi.org/10.1021/nn300760g

Tauc, J. (1974). *Amorphous and liquid semiconductors*.

Thambiraja, S., & Shankaran, D. R. (2016). Green synthesis of highly fluorescent carbon quantum dots from sugarcane bagasse pulp. *Applied Surface Science, 390,* 435–443. https://doi.org/10.1016/j.apsusc.2016.08.106

Tong, T., Zhang, M., Chen, W., Huo, X., Xu, F., Yan, H., Lai, C., Wang, W., Hu, S., Qin, L., & Huang, D. (2024). Recent advances in carbon-based material/semiconductor composite photoelectrocatalysts: Synthesis, improvement strategy, and organic pollutant removal. *Coordination Chemistry Reviews, 500*(May 2023), 215498. https://doi.org/10.1016/j.ccr.2023.215498

Urbach, F. (1953). The long-wavelength edge of photographic sensitivity and of the electronic Absorption of Solids. *Physical Review*, *92*(5), 1324. https://doi.org/10.1103/PhysRev.92.1324

Wang, H. Y., Hu, R., Wang, N., Hu, G. L., Wang, K., Xie, W. H., & Cao, R. (2021). Boosting photoanodic activity for water splitting in carbon dots aqueous solution without any traditional supporting electrolyte. *Applied Catalysis B: Environmental*, *296*(February), 120378. https://doi.org/10.1016/j.apcatb.2021.120378

Wang, L., Weng, S., Su, S., & Wang, W. (2023). Progress on the luminescence mechanism and application of carbon quantum dots based on biomass synthesis. *RSC Advances*, *13*(28), 19173–19194. https://doi.org/10.1039/d3ra02519e

Wang, N., Zhang, Y. S., Wei, D. D., Duan, H. M., Mo, L. M., & Wang, H. Y. (2023). Carbon quantum dots aqueous solution as electrolyte for H2O2 production based on photoelectrochemical water splitting. *Journal of Materials Chemistry A*, *11*(8), 4162–4169. https://doi.org/10.1039/d2ta09453c

Wang, R., Lu, K. Q., Tang, Z. R., & Xu, Y. J. (2017). Recent progress in carbon quantum dots: synthesis, properties and applications in photocatalysis. *Journal of Materials Chemistry A*, *5*(8), 3717–3734. https://doi.org/10.1039/c6ta08660h

Wang, T., Peng, L., Wu, D., Chen, B., & Jia, B. (2023). Crude fiber and protein rich cottonseed meal derived carbon quantum dots composite porous carbon for supercapacitor. *Journal of Alloys and Compounds*, *947*, 169499. https://doi.org/10.1016/j.jallcom.2023.169499

Wang, Y., Liu, X., Han, X., Godin, R., Chen, J., Zhou, W., Jiang, C., Thompson, J. F., Mustafa, K. B., Shevlin, S. A., Durrant, J. R., Guo, Z., & Tang, J. (2020). Unique hole-accepting carbon-dots promoting selective carbon dioxide reduction nearly 100% to methanol by pure water. *Nature Communications*, *11*(1), 1–9. https://doi.org/10.1038/s41467-020-16227-3

Wang, Z., Huang, H., Li, G., Yan, X., Yu, Z., Wang, K., & Wu, Y. (2021). Advances in engineering perovskite oxides for photochemical and photoelectrochemical water splitting. *Applied Physics Reviews*, *8*(2). https://doi.org/10.1063/5.0039197

Wang, Z., Liu, J., Wang, W., Wei, Z., Wang, F., Gong, P., Wang, J., Li, N., Liu, B., Zhang, Z., Wang, W., & Sun, L. (2017). Photoluminescent carbon quantum dot grafted silica nanoparticles directly synthesized from rice husk biomass. *Journal of Materials Chemistry B*, *5*(24), 4679–4689. https://doi.org/10.1039/c7tb00811b

Wareing, T. C., Gentile, P., & Phan, A. N. (2021). Biomass-Based Carbon Dots: Current Development and Future Perspectives. *ACS Nano*, *15*(10), 15471–15501. https://doi.org/10.1021/acsnano.1c03886

Wei, S., Yin, X., Li, H., Du, X., Zhang, L., Yang, Q., & Yang, R. (2020). Multi-Color Fluorescent Carbon Dots: Graphitized sp2 Conjugated Domains and Surface State Energy

Level Co-Modulate Band Gap Rather Than Size Effects. *Chemistry - A European Journal*, *26*(36), 8129–8136. https://doi.org/10.1002/chem.202000763

Wu, F., Su, H., Zhu, X., Wang, K., Zhang, Z., & Wong, W. K. (2016). Near-infrared emissive lanthanide hybridized carbon quantum dots for bioimaging applications. *Journal of Materials Chemistry B*, *4*(38), 6366–6372. https://doi.org/10.1039/c6tb01646d

Wu, F., Yang, M., Zhang, H., Zhu, S., Zhu, X., & Wang, K. (2018). Facile synthesis of sulfur-doped carbon quantum dots from vitamin B1 for highly selective detection of Fe3+ ion. *Optical Materials*, *77*, 258–263. https://doi.org/10.1016/j.optmat.2018.01.048

Wu, H., Tan, H. L., Toe, C. Y., Scott, J., Wang, L., Amal, R., & Ng, Y. H. (2020). Photocatalytic and Photoelectrochemical Systems: Similarities and Differences. *Advanced Materials*, *32*(18), 1–21. https://doi.org/10.1002/adma.201904717

Xia, C., Wang, H., Kim, J. K., & Wang, J. (2021). Rational Design of Metal Oxide-Based Heterostructure for Efficient Photocatalytic and Photoelectrochemical Systems. *Advanced Functional Materials*, *31*(12), 1–31. https://doi.org/10.1002/adfm.202008247

Xu, J., Olvera-Vargas, H., Ou, G. H. X., Randriamahazaka, H., & Lefebvre, O. (2023). Hybrid TiO2/Carbon quantum dots heterojunction photoanodes for solar photoelectrocatalytic wastewater treatment. *Chemosphere*, *341*(August), 140077. https://doi.org/10.1016/j.chemosphere.2023.140077

Xu, S., Li, M., Wang, Y., & Jin, Z. (2024). Enhanced photocatalytic hydrogen evolution over coal-based carbon quantum dots modified CoMoO4/g-C3N4. *International Journal of Hydrogen Energy*, *51*, 16–30. https://doi.org/10.1016/j.ijhydene.2023.09.260

Xu, S., Sun, W., Meng, X., Dong, Y., & Ding, Y. (2021). Carbon Quantum Dot Conjugated Copper(II) Phthalocyanine Integrating BiVO4Semiconductor for Photocatalytic Water Oxidation. *Journal of Physical Chemistry C*, *125*(44), 24413–24421. https://doi.org/10.1021/acs.jpcc.1c07491

Xu, X., Ray, R., Gu, Y., Ploehn, H. J., Gearheart, L., Raker, K., & Scrivens, W. A. (2004). Electrophoretic analysis and purification of fluorescent single-walled carbon nanotube fragments. *Journal of the American Chemical Society*, *126*(40), 12736–12737. https://doi.org/10.1021/ja040082h

Xue, M., Zhan, Z., Zou, M., Zhang, L., & Zhao, S. (2016). Green synthesis of stable and biocompatible fluorescent carbon dots from peanut shells for multicolor living cell imaging.

New Journal of Chemistry, *40*(2), 1698–1703. https://doi.org/10.1039/c5nj02181b

Yan, Y., Zhai, D., Liu, Y., Gong, J., Chen, J., Zan, P., Zeng, Z., Li, S., Huang, W., & Chen, P. (2020). van der Waals Heterojunction between a Bottom-Up Grown Doped Graphene Quantum Dot and Graphene for Photoelectrochemical Water Splitting. *ACS Nano*, *14*(1), 1185–1195. https://doi.org/10.1021/acsnano.9b09554

Yoshino, S., Takayama, T., Yamaguchi, Y., Iwase, A., & Kudo, A. (2022). CO2Reduction Using Water as an Electron Donor over Heterogeneous Photocatalysts Aiming at Artificial Photosynthesis. *Accounts of Chemical Research*, *55*(7), 966–977. https://doi.org/10.1021/acs.accounts.1c00676

Yu, T., Wang, D., Liu, M., Lei, W., Shafie, S., Mohtar, M. N., Jindapetch, N., Dommelen, P. van, & Zhao, Z. (2024). Exploiting Carbon Quantum Dots Synthesized by Electrochemical Exfoliation for Flexible Resistance Switching. *ACS Materials Letters*, *6*(3), 793–800. https://doi.org/10.1021/acsmaterialslett.3c01258

Yuan, M., Zhong, R., Gao, H., Li, W., Yun, X., Liu, J., Zhao, X., Zhao, G., & Zhang, F. (2015). One-step, green, and economic synthesis of water-soluble photoluminescent carbon dots by hydrothermal treatment of wheat straw, and their bio-applications in labeling, imaging, and sensing. *Applied Surface Science*, *355*, 1136–1144. https://doi.org/10.1016/j.apsusc.2015.07.095

Zanatta, A. R. (2019). Revisiting the optical bandgap of semiconductors and the proposal of a unified methodology to its determination. *Scientific Reports*, *9*(1), 11225. https://doi.org/10.1038/s41598-019-47670-y

Zeng, Z., Xiao, F. X., Gui, X., Wang, R., Liu, B., & Yang Tan, T. T. (2016). Layer-by-layer assembly of nitrogen-doped graphene quantum dots monolayer decorated one-dimensional semiconductor nanoarchitectures for solar-driven water splitting. *Journal of Materials Chemistry A*, *4*(42), 16383–16393. https://doi.org/10.1039/c6ta05469b

Zhang, J., Xu, J., & Tao, F. (2021). Interface Modification of TiO2Nanotubes by Biomass-Derived Carbon Quantum Dots for Enhanced Photocatalytic Reduction of CO2. *ACS Applied Energy Materials*, *4*(11), 13120–13131. https://doi.org/10.1021/acsaem.1c02760

Zhang, Q., Tian, F., Zhou, Q., Zhang, C., Tang, S., Jiang, L., & Du, S. (2022). Targeted ginkgo kernel biomass precursor using eco-friendly synthesis of efficient carbon quantum dots for detection of trace nitrite ions and cell imaging. *Inorganic Chemistry Communications*, *140*(April), 109442. https://doi.org/10.1016/j.inoche.2022.109442

Zhang, Y., Fan, X., Sun, X., Yang, X., Li, Z., Yang, Z., & Dong, C. (2024). Synthesis of oil-soluble carbon dots via pyrolysis and their diverse applications in doxycycline detection, fluorescent ink and film. *Spectrochimica Acta - Part A: Molecular and Biomolecular Spectroscopy, 304*(September 2023), 123406. https://doi.org/10.1016/j.saa.2023.123406

Zhang, Y. S., Duan, H. M., Wang, N., Wei, D. D., Mo, L. M., Wang, N., Wang, X. P., Lei, S. L., Zhang, Y., & Wang, H. Y. (2023). Developing positively surface-charged carbon dots as "semiconductor electrolyte" for photo-electrochemical H2O2 production based on oxygen reduction. *Chemical Engineering Journal*, *477*(September), 146903. https://doi.org/10.1016/j.cej.2023.146903

Zhang, Z., Wei, L., Qin, X., & Li, Y. (2015). Carbon nanomaterials for photovoltaic process. *Nano Energy*, *15*, 490–522. https://doi.org/10.1016/j.nanoen.2015.04.003

Zhao, F., Li, X., Zuo, M., Liang, Y., Qin, P., Wang, H., Wu, Z., Luo, L., Liu, C., & Leng, L. (2023). Preparation of photocatalysts decorated by carbon quantum dots (CQDs) and their applications: A review. *Journal of Environmental Chemical Engineering*, *11*(2), 109487. https://doi.org/10.1016/j.jece.2023.109487

Zhong, H., Sa, R., Lv, H., Yang, S., Yuan, D., Wang, X., & Wang, R. (2020). Covalent Organic Framework Hosting Metalloporphyrin-Based Carbon Dots for Visible-Light-Driven Selective CO2 Reduction. *Advanced Functional Materials*, *30*(35), 1–8. https://doi.org/10.1002/adfm.202002654

Zhu, Z., Yang, P., Li, X., Luo, M., Zhang, W., Chen, M., & Zhou, X. (2020). Green preparation of palm powder-derived carbon dots co-doped with sulfur/chlorine and their application in visible-light photocatalysis. *Spectrochimica Acta - Part A: Molecular and Biomolecular Spectroscopy*, *227*, 117659. https://doi.org/10.1016/j.saa.2019.117659

Zucolotto, V., Ferreira, M., Cordeiro, M. R., Constantino, C. J. L., Balogh, D. T., Zanatta, A. R., Moreira, W. C., & Jr., O. N. O. (2003). *Layer-by-layer and Langmuir-Blodgett films from nanoparticles and complexes Unusual Interactions Binding Iron Tetrasulfonated Phthalocyanine and Poly (allylamine hydrochloride) in Layer-by-Layer Films*. *May 2020*.

Zuo, P., Lu, X., Sun, Z., Guo, Y., & He, H. (2016). A review on syntheses, properties, characterization and bioanalytical applications of fluorescent carbon dots. *Microchimica Acta*, *183*(2), 519–542. https://doi.org/10.1007/s00604-015-1705-3